EFFECTS OF LARGE DAMAGE ON RESIDUAL STRENGTH OF CARBON FIBER REINFORCED COMPOSITE LAMINATES

A Thesis by

Muhammad Munir Zanial

Bachelor of Science, Rensselaer Polytechnic Institute, 2005

Submitted to the Department of Aerospace Engineering
and the faculty of the Graduate School of
Wichita State University
in partial fulfillment of
the requirements for the degree of
Master of Science

May 2014

EFFECTS OF LARGE DAMAGE ON RESIDUAL STRENGTH OF CARBON FIBER REINFORCED COMPOSITE LAMINATES

The following faculty members have examined the final copy of this thesis for form and content, and recommend that it be accepted in partial fulfillment of the requirement for the degree of Master of Science, with a major in Aerospace Engineering.

_____

John S. Tomblin, Committee Chair

_____

Waruna Seneviratne, Committee Member

_____

Alexander Bukhgeym, Committee Member

DEDICATION

To my caring parents, my loving wife, my beautiful children, supportive colleagues, family members, and friends

ACKNOWLEDGEMENTS

In the name of God, the Compassionate and the Merciful. Praise be to God for his mercy that allows the completion of this work.

I would like to express my gratitude to my advisors and committee members, Dr. John Tomblin, Dr. Waruna Seneviratne and Dr. Alexander Bukhgeym for the opportunity to work together on this topic and for their continuous support and guidance. Immense thanks are also due to Dr. YK Hwang, Richard Hostert and Ric Abbott for being there every step of the way from the conception of the problem statement to the conclusion of this study. No amount of paid lunches or meals would equate to the value of their kind assistance.

At the professional level, I would like to thank Bombardier Learjet, my director Pierre Harter, my manager Greg Davied and my long-time friend Anand Kathula for allowing me to use this topic as the focus of my thesis and for supporting me throughout my years of graduate studies. Special thanks to Upul Palliyaguru and the rest of the crew for supporting this project. All of them have been very flexible and supportive in seeing me succeed in this interesting endeavor.

At the personal level, countless gratitude goes to my parents, Danial Sulaiman and Maimunah Ismail, for the prayers and sacrifice they have made in all these years of my life and to my loving wife, Najmiah Mukhtar and beautiful children, Muhriz and Mueez, for putting me before themselves in every situation. Sleepless nights and missing-in-action time are now finally over. ‘Abi’ finally did it.

Finally, great thanks to every single one of you that has helped me directly or indirectly in getting this work completed. Thanks again.

ABSTRACT

Tension or compression fracture behavior studies are normally initiated with open hole tension or compression tests performed at the laminate level. While these test data serve as an excellent starting point in residual strength studies in small notch sizes, the need to evaluate and verify the residual strength for larger structures and at larger notch sizes region is still there.

An experimental study was performed with the focus on large notch sizes of circular hole and narrow slit flaw configurations on laminates fabricated with a carbon/epoxy oven-cure capable prepreg material system. The current part of the study focused on uniaxial tension loading with a constant width and height to flaw dimension ratio. Experimental test data were then combined with lamina and laminate level data for residual strength curves generation and the curves were validated against Whitney-Nuismer and Mar-Lin fracture mechanics models. The effects of flaw sizes and the flaw type towards the residual strength capability of a laminate turn out to be substantial as the notch size gets larger than one inch. Test results showed that a narrow slit or saw cut damage is far more critical than a circular hole cut-out. The notch sensitivity order of a saw cut flaw is also roughly three times more than that of a circular hole.

Analytical studies were also performed to evaluate several finite element method variable effects on residual strength prediction and to discover the best practice in stress analyses of notched composite laminates. Point Stress failure criterion was used in the analyses and predicted failure loads were compared to the experimental data. Good agreements and correlations were found between the analytical predictions and the experimental data. It can be concluded that the residual strength of a notched laminated composite can be reasonably predicted from finite element analyses.

TABLE OF CONTENTS

TABLE OF CONTENTS (continued)

TABLE OF CONTENTS (continued)

LIST OF TABLES

LIST OF TABLES (continued)

LIST OF FIGURES

LIST OF FIGURES (continued)

LIST OF FIGURES (continued)

LIST OF ABBREVIATIONS / NOMENCLATURE

AML	Angled Minus Longitudinal
ASCD	Autodesk Composite Simulation Design
ASTEC	Aircraft Structural Test and Evaluation Center
ASTM	American Society for Testing And Materials
CNC	Computer Numerical Control
CTD	Cold Temperature Dry
CPT	Cured Ply Thickness
ETW	Elevated Temperature Wet
FEA	Finite Element Analysis
FEM	Finite Element Method
FPF	First Ply Failure
ID	Identification
LEFM	Linear Elastic Fracture Mechanics
ML	Mar-Lin
Mode I	Crack Opening Mode
N/A	Not Applicable
NDI	Non-Destructive Inspection
NIAR	National Institute For Aviation Research
OH	Open Hole
PW	Plain Weave
RTA	Room Temperature Ambient

RVE	Representative Volume Element
SC	Saw Cut
SG	Strain Gage
TTU	Through-Transmission Ultrasonic
UD	Unidirectional
ULF	Ultimate Laminate Failure
WEK	Waddoups, Eisenmann and Kaminski
WN	Whitney-Nuismer
WSU	Wichita State University

LIST OF SYMBOLS

$\bar{E}_{11}$	Effective Longitudinal Elastic Modulus of Laminate
$\bar{E}_{22}$	Effective Transverse Elastic Modulus of Laminate
$\bar{G}_{12}$	Effective Shear Modulus of Laminate
$\bar{\nu}_{12}$	Effective Laminate Poisson's Ratio
a	Characteristic Dimension or Length
a_c	Crack Tip Damage Zone Size
c	Half-Length of a Straight Crack
C_L	Centerline
D	Degree of Damage at Crack Tip
ε_y	Y-Component of Strain
E	Young's Modulus
E_{22_f}	Fiber Transverse Modulus
E_{22_m}	Matrix Transverse Modulus
E_{11}	Lamina Longitudinal Modulus
E_{22}	Lamina Transverse Modulus
E_{33}	Lamina Interlaminar Modulus
f_i	Second-Order Strength Tensor
f_{ij}	Fourth-Order Strength Tensor
G_{12_f}	Fiber In-Plane Shear Modulus
G_{12_m}	Matrix In-Plane Shear Modulus
G_{23_f}	Fiber Transverse Shear Modulus

G_{12}	Lamina In-Plane Shear Modulus
G_{13}	Lamina Transverse Shear Modulus
G_{23}	Lamina Transverse Shear Modulus
G_I	Energy Release Rate
gcc	Gram per Cubic Centimeters
gsm	Gram per Square Meter
H_C	Composite Fracture Toughness
h	Height
inHg	Inch of Mercury
K_I	Stress Intensity Factor
K_t	Stress Concentration Factor
n	Order of Singularity
pcf	Pound per Cubic Foot
R	Circular Hole Radius
t	Thickness
S_{12_m}	Matrix In-Plane Shear Strength
S_{12}	Lamina In-Plane Shear Strength
$\mu\varepsilon$	Microstrain
ν	Poisson's Ratio
ν_{12_f}	Fiber Poisson's Ratio for 1-2 Plane
ν_{23_f}	Fiber Poisson's Ratio for 2-3 Plane

ν_{12}	Lamina Poisson's Ratio for 1-2 Plane
ν_{13}	Lamina Poisson's Ratio for 1-3 Plane
ν_{23}	Lamina Poisson's Ratio for 2-3 Plane
ρ	Lamina Density
σ^{∞}	Far-Field Stress
σ_N^{∞}	Notched Residual Strength
σ_y	Y-Component of Stress
w	Width
$+S_{1_m}$	Matrix Tensile Strength
$+S_1$	Lamina Longitudinal Tensile Strength
$+S_2$	Lamina Transverse Tensile Strength
$-S_{1_f}$	Fiber Longitudinal Compression Strength
$-S_{1_m}$	Matrix Compression Strength
$-S_1$	Lamina Longitudinal Compression Strength
$-S_2$	Lamina Transverse Compression Strength
2c	Full-Length of a Straight Crack

CHAPTER 1

INTRODUCTION

1.1 Background Information

Since the start of commercial use of composite in industrial, consumer goods and transportation applications, the need to further understand advanced composite material behavior has dramatically increased. Along with continuous material characterization efforts in static and fatigue fields, a large focus has also been made in the damage tolerance aspects of composite materials. While the variety of composite material types and selections are huge, the focus of this study is on one specific continuous carbon fiber reinforced and epoxy composite material system typical for uses in the manufacture of composite aerospace primary structural element applications.

The emphasis on the study of the behavior of composite laminates with stress concentrations is needed to address residual strength properties due to necessary section cut-outs such as for aircraft windows or access panels, or due to possible scenarios of aircraft structural damage such as from manufacturing and in-service damage sources. Efforts to explore tension and compression fracture behaviors of laminated composite have been extensive from 1960s to this day.

Tension or compression fracture behavior studies are normally initiated with open hole tension or compression tests performed at laminate level with a nominal 0.25” diameter hole per ASTM D 5766 procedures [1]. While these test data serve as an excellent starting point in residual strength studies in small notch sizes, the need to evaluate and verify the residual strength for larger structures and at larger notch sizes region is still there. In addition, variability of damage threats necessitates the evaluation of other flaw types and characteristics such as through

thickness slits, cracks, or saw cuts (potential damage inflicted from a high energy impact scenario). These three terms are used interchangeably within the context of composite fracture mechanics discussion, even though one may argue that the flaw geometry in between these three types may be different. All these flaws have a generic shape of an ellipsoidal cut-out where the ratio of major axis dimension to the minor axis dimension is large.

The concept of stress concentration factor, K_t to understand stress concentrations and distributions around notches has been very useful for an open hole flaw. However, for an elliptical crack, slit or slender saw cuts, it is no longer a meaningful concept since with near zero tip radius, K_t would become infinitely large. Thus the concept of stress intensity factor, K_I was introduced [2] or generally known as Linear Elastic Fracture Mechanics (LEFM). However, the crack tip behavior in composite materials is more complicated than that in metallic materials. Due to the orthotropic nature of continuous fiber reinforced composite materials, several adaptations of the LEFM model and new failure models have been found more applicable.

These models were reviewed from available literature and then used to validate and verify the experimental study along with the supporting finite element models. Procedures and techniques used in experimental and analytical studies are covered thoroughly so that the document is self-contained and the results can be reconstructed or further validated. There are, however, several details that cannot be published due to the proprietary nature of the data.

1.2 Purpose of Study

The purposes of the thesis are to:

1. Evaluate the residual strengths of the subject composite material system with large damage

2. Provide correlations and comparisons between open hole versus saw cut damage residual strength effects and notch sensitivities
3. Validate and calibrate the experimental data with reference to published literature
4. Develop finite element analysis (FEA) methodologies to be used to predict residual strength

CHAPTER 2

LITERATURE REVIEW

2.1 Overview of Composite Fracture Models

For metallic materials, a flaw grows from the initial flaw size via the self-similar extension of the flaw itself [3]. For composites, however, the flaw geometry generally remains unchanged as the load is increased but the damage zone would significantly increase [3]. The factors that affect the progression and the intensification of the damage zone ahead of the crack tip are not well understood. Micromechanical phenomena such as fiber breakage, interply delamination or interfacial seperation, fiber-matrix debonding, matrix micro-cracking, and macromechanical failure phenomena contribute to the damage zone creation and progression in composites [4]. The understanding of the behavior of the damage zone in notched composite laminates is hoped to be as important as the plastic zone concept in the LEFM for metals [3].

A look at all of the fracture models to date has revealed that none of them have made an attempt to explore the interlaminar interaction between plies in the laminate [3]. While the simplification of treating laminated composite plate as an orthotropic plate is recognized for the ease of fracture model use, it fails to address the micromechanical phenomena and interactions occurring at the crack tip region. Similarly, most fracture models to date assume self-similar crack growth and are mostly based on a semi-empirical approach [3].

Overview and comparisons of most commonly used composite fracture models for predicting notched properties of composite laminates were covered extensively by Awerbuch and Madhukar [5]. Another fracture model that is also worth noting, excluded from Awerbuch et al. [5], is the D-Criterion model [6]. The D-Criterion model proposes the use of a parameter that

would represent the degree of damage at the crack tip, *D*, to replace the conventional notion of stress intensity factor, K_I.

As a reminder, the term 'crack' from the composite material system perspective when discussed with regards to fracture mechanics models would rather suggest an artificially induced narrow slit or notch rather than a typical hairline fracture or crack line in metallic materials. In most cases, the reviewed fracture models within this document are presented along with the notion of characteristic dimension, *a*.

2.1.1 Waddoups-Esseinmann-Kaminski (WEK) Model

Waddoups, Eisenmann, and Kaminski (WEK) fracture model was based on the concepts of LEFM adapted from homogeneous isotropic materials and validated against experimental data [7]. One model was developed for laminates containing circular holes and the other model was for straight cracks.

Circular Holes

Without focusing on the details of the damage zone in terms of actual stress function ahead of the flaw tip region, the WEK model is based on the relationship between the energy release rate, G_I and the stress intensity factor, K_I shown in Equation (1) [7]:

$$G_I = \frac{(1-\nu^2)\pi}{E} K_I^2 \tag{1}$$

where ν is Poisson's ratio and *E* is Young's modulus of the material. From the LEFM, stress intensity factor, K_I can be presented as shown in Equation (2) [8] where there is a geometric correction factor, *f*:

$$K_I = \sigma_N^{\infty}\sqrt{\pi a} f\left(\frac{a}{R}\right) \tag{2}$$

where σ_N^∞ is the notched residual strength, a is the characteristic length and R is the circular hole radius. The relationships from the equations can lead to a normal presentation of residual strength in terms of a ratio of un-notched property and notched property as shown in Equation (3):

$$\frac{\sigma_{UN}}{\sigma_N^\infty} = f(\frac{a}{R}) \tag{3}$$

Straight Cracks

Similarly, for straight cracks of length, *2c,* the LEFM concepts were adapted for the composite material applications. The stress intensity factor for notched laminate with straight cracks, K_{IC} is based on Irwin's plastic zone approximation where half-crack length, c, is preceded with crack tip damage zone size (or referred to as plastic zone correction length for metallic materials) at the crack tip, a_c [9].

$$K_{IC} = \sigma_N^\infty \sqrt{\pi(c + a_c)} \tag{4}$$

For an unnotched case, the stress intensity factor becomes:

$$K_{IC} = \sigma_{UN} \sqrt{\pi a_c} \tag{5}$$

Thus, the ratio of notched strength to unnotched strength can be presented as:

$$\frac{\sigma_N^\infty}{\sigma_{UN}} = \sqrt{\frac{a_c}{c + a_c}} \tag{6}$$

The crack tip damage zone size, a_c can be determined empirically from curve-fitting of the notched properties. After rearrangement of Equation (6), a_c can be represented as the slope of the curve-fit function, as shown in Equation (7) [5]. An example of this curve-fitting is shown in Figure 2-1, extracted from Awerbuch et al. [5]. Depending on the curve-fit results, a single characteristic dimension may be used across a wide range of notch sizes. It was reported that a_c

is independent of original crack length, c and it is part of a material parameter, thus dependent on the laminate configuration and the material system [5].

$$c = a_c \left[\left(\frac{\sigma_{UN}}{\sigma_N^{\infty}} \right)^2 - 1 \right] \tag{7}$$

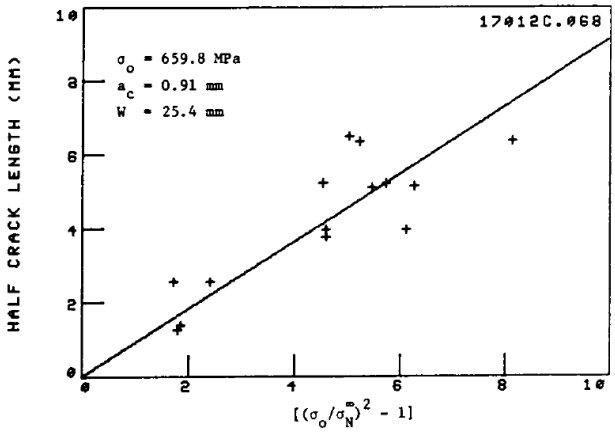

Figure 4. *Best fit for a_c (WEK-fracture model) for graphite/epoxy [0/±45]$_s$ laminate containing a center crack.*

Figure 2-1 Example of characteristic dimension determination via curve-fit of notched property data [5]

In general, it was recognized that via the use of the LEFM methods, acceptable correlations with experimental data were found but it must be cautioned that the applicability of this fracture model was found to be limited. The isotropic fracture mechanics can only be directly applied to anisotropic plates when under these conditions [10]:

1. The flaw orientation with respect to the principal axis of symmetry must be fixed
2. The stress intensity factor for anisotropic case must be consistent with the isotropic case in stress distribution and in crack displacement modes
3. The critical orientation coincides with one of the principal directions of elastic symmetry

2.1.2 Whitney-Nuismer (WN) Model

Whitney-Nuismer (WN) proposed the use of two criteria that assume that fracture occurs when the stress at an arbitrary characteristic dimension reaches the unnotched strength. These two criteria were dubbed as the "point-stress" and "average-stress" criteria. This notion is similar to that of the WEK model except that there is no application of isotropic LEFM. Whitney-Nuismer further made the argument that the application of LEFM for composite materials is rather flawed based on the fact that:

1. The types of single cracks observed in metals do not form in matrix of composite materials under repeated loads
2. For composites, there is a different relationship from that of metals such that with greater tensile strength, the fracture toughness increases.

Point-Stress Criterion

For this failure criterion, failure is assumed to occur when the stress tangential to the flaw edge, σ_y over some characteristic distance, a equals to or exceeds the strength of unnotched laminate [11]. For the case of straight crack flaw, the term R in the equation is replaced with half crack length, c.

$$\sigma_y(x,0)_{|x=R+a} = \sigma_{UN} \tag{8}$$

Average-Stress Criterion

For this failure criterion, failure is assumed to occur when the average stress tangential to the flaw edge, σ_y, over some characteristic distance, a equals to or exceeds the strength of unnotched laminate [11]. Similarly, for the case of straight crack flaw, the term R in the equation is replaced with half crack length, c.

$$\sigma_{UN} = \frac{1}{a}\int_{R}^{R+a} \sigma_y(x,0)\, dx \tag{9}$$

Circular Holes

For an infinite orthotropic plate with a circular hole of radius, R and subjected to uniform stress, σ^{∞} applied along the y-axis, the normal stress, σ_y distribution along the horizontal x-axis can be expressed as [12]:

$$\sigma_y(x,0) = \frac{\sigma^{\infty}}{2}\underbrace{\left\{2 + \left(\frac{R}{x}\right)^2 + 3\left(\frac{R}{x}\right)^4\right.}_{\text{Isotropic contribution}} \underbrace{\left. - (K_t - 3)\left(5\left(\frac{R}{x}\right)^6 - 7\left(\frac{R}{x}\right)^8\right)\right\}}_{\text{Anisotropic contribution}} for\ x > R \tag{10}$$

where K_t is the stress concentration factor. For a sanity check, for an open hole in an isotropic material, the maximum circumferential stress at the hole radius edge, which equals to $3\sigma^{\infty}$, can only be achieved if the isotropic contribution is used while the anisotropic contribution vanishes since K_t equals three. The stress concentration factor for orthotropic composite materials can be expressed as [13]:

$$K_t = 1 + \sqrt{2\left(\sqrt{\frac{\bar{E}_{11}}{\bar{E}_{22}}} - \bar{\nu}_{12}\right) + \frac{\bar{E}_{11}}{\bar{G}_{12}}} \tag{11}$$

where $\bar{E}_{11}$ is the effective longitudinal elastic modulus of the laminate parallel to the loading direction, $\bar{E}_{22}$ is the effective transverse elastic modulus of the laminate perpendicular to the loading direction, $\bar{\nu}_{12}$ is the effective laminate Poisson's ratio, and $\bar{G}_{12}$ is the effective shear modulus of the laminate. It must be noted that for the isotropic and quasi-isotropic materials, K_t equals three.

Thus, for Point Stress Criterion, the ratio of notched strength to unnotched strength can be presented as:

$$\frac{\sigma_N^\infty}{\sigma_{UN}} = \frac{2}{\left\{2 + \left(\frac{R}{R+a}\right)^2 + 3\left(\frac{R}{R+a}\right)^4 - (K_t - 3)\left(5\left(\frac{R}{R+a}\right)^6 - 7\left(\frac{R}{R+a}\right)^8\right)\right\}} \quad (12)$$

where *a* is the characteristic distance or length. Thus, from Equation (12), for a very large open hole, the ratio $\frac{\sigma_N^\infty}{\sigma_{UN}}$ would approach to $\frac{1}{K_t}$. As expected, when the radius of a hole is small, the ratio $\frac{\sigma_N^\infty}{\sigma_{UN}}$ would approach one.

On the other hand, for the Average Stress Criterion, the ratio of notched strength to unnotched strength can be presented as [12]:

$$\frac{\sigma_N^\infty}{\sigma_{UN}} = \frac{2\left(1 - \frac{R}{R+a}\right)}{\left\{2 - \left(\frac{R}{R+a}\right)^2 - \left(\frac{R}{R+a}\right)^4 + (K_t - 3)\left(\left(\frac{R}{R+a}\right)^6 - \left(\frac{R}{R+a}\right)^8\right)\right\}} \quad (13)$$

Straight Cracks

For an elliptical opening in an anisotropic plate, such as straight crack of length, *2c*, the stress distribution function ahead of the crack tip can be reduced to [13]:

$$\sigma_y(x, 0) = \frac{K_I x}{\sqrt{\pi c(x^2 - c^2)}} \; for \; x > c \quad (14)$$

where K_I is the Mode I stress intensity factor, *x* is the horizontal coordinate from the center of the crack and *c* is half of the total crack length. K_I can be calculated from:

$$K_I = \sigma^\infty \sqrt{\pi c} \quad (15)$$

Similar to circular hole flaw, the two proposed failure criteria of Equation (8) and Equation (9) are also used for straight cracks. For Point Stress criterion, the ratio of notched strength to unnotched strength can be presented as [5]:

$$\frac{\sigma_N^{\infty}}{\sigma_{UN}} = \sqrt{1 - \left(\frac{c}{c+a}\right)^2} \tag{16}$$

For Average Stress criterion, the ratio of notched strength to unnotched strength can be presented as [5]:

$$\frac{\sigma_N^{\infty}}{\sigma_{UN}} = \sqrt{\frac{1 - \left(\frac{c}{c+a}\right)}{1 + \left(\frac{c}{c+a}\right)}} \tag{17}$$

It was also reported that the characteristic dimensions for both failure criteria depend on the material system and the laminate configuration [5].

2.1.3 Mar-Lin (ML) Model

The Mar-Lin (ML) fracture model was adapted from the LEFM where for homogeneous isotropic materials, notched strength is represented as:

$$\sigma_N^{\infty} = \frac{K_{IC}}{\sqrt{\pi c}} = K_{IC}(\pi c)^{-0.5} \tag{18}$$

in which the exponent 0.5 is the order of stress singularity at the tip of the crack. While other failure models such as the WN model have incorporated in their models a concept of effective crack length or characteristic dimension, Mar and Lin [14], on the other hand, proposed that in composites the relationship is:

$$\sigma_N^{\infty} = \frac{H_C}{(2c)^n} = H_C(2c)^{-n} \tag{19}$$

where H_C is the composite fracture toughness and n is the order of singularity of a crack in the matrix, with the tip at the fiber/matrix interface. The ML fracture model can be applied to both open hole and straight crack flaws.

It was found that the type of discontinuity or flaw has little effect on the notched strength of the materials such that the same values of H_C and n were used for all cases [15]. It must be

noted, however, that the order of singularity, n, depends on laminate lay-up. In terms of the ratio of notched strength to unnotched strength, the ML model is more conveniently expressed in a logarithmic form:

$$\log\left(\frac{\sigma_N^{\infty}}{\sigma_{UN}}\right) = \log\left(\frac{H_C}{\sigma_{UN}}\right) - n\log(2c) \tag{20}$$

CHAPTER 3

EXPERIMENTAL STUDY

This chapter describes the extent of the experimental study performed to evaluate the effects of large damage on composites. The test specimens were fabricated and extracted at the National Institute for Aviation Research (NIAR) facility in Wichita, Kansas. All mechanical tests associated with the thesis were conducted at the NIAR test labs.

3.1 Test Scope

This experimental study was designed to:

1. Evaluate tension fracture strengths of the subject prepreg material system under Mode I dominant loading condition.
2. Focus on effects on residual strength properties stemming from notch sizes that are larger than one inch long.
3. Assess whether there is any effect on residual strength performance because of varying laminate thicknesses.
4. Quantify the residual strength effects from various test environments and from a unique design feature, co-cured splice.
5. Provide correlations and comparisons between circular hole versus saw cut damage residual strength effects and notch sensitivities.

In general, tests performed within this document are shown in Figure 3-1. Open hole damage served as the control test case while more emphasis was made on the saw cut damage.

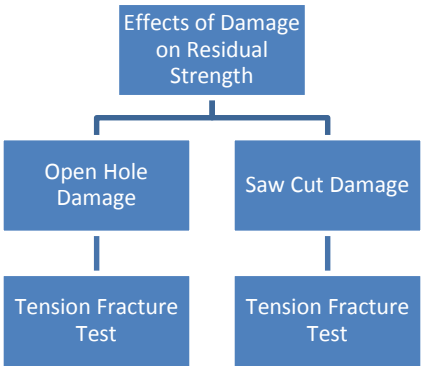

Figure 3-1 Test overview

3.1.1 General Workflow

The general work flow involved within this thesis is shown in Figure 3-2.

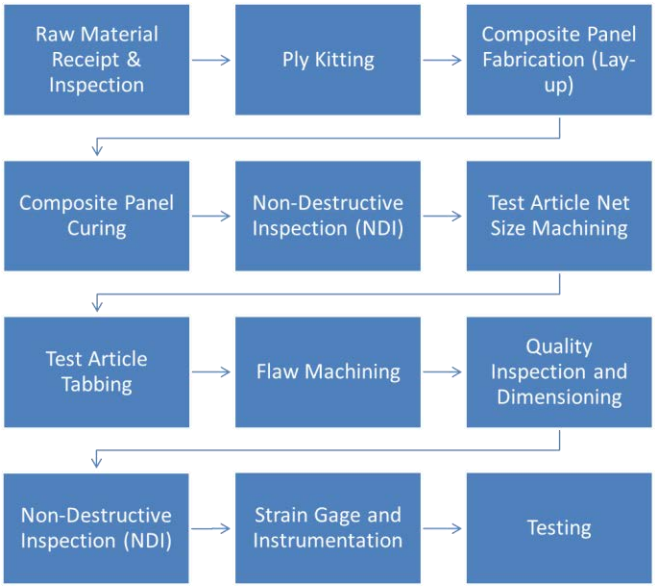

Figure 3-2 General workflow

3.1.2 Test Article Configuration

Test articles were rectangular, flat monolithic plain weave panels designed with various sizes of flaw length, which are designated by '2c' dimensions where 'c' is the half-crack or half-defect dimension. Plain weave prepreg style was selected mainly due to its wide range of usage in primary structural element constructions and the fact that its being the most popular weave style in the industry.

Flaw length dimension was sized to the maximum dimension within the test machines capability available at the NIAR. The largest test frame available was capable of applying 500kip maximum and accommodating 6 feet by 6 feet test space including test fixturing. To be conservative, two feet (one foot at each end) were designated for test fixturing purposes, leaving four feet length as the maximum possible test article height. The ratio selections described in Table 3-1 were based on Walker et al.'s evaluation with the rationale that they were critical to avoid the effects of finite width and finite height on the evaluated residual strengths [16].

TABLE 3-1

TEST ARTICLE CONFIGURATION

Panel Configuration	Laminate Configuration[(1)]	Flaw Length, 2c (in)	Flaw Type	Gage Section Width per Flaw Length Ratio, w/2c	Gage Section Height per Flaw Length Ratio, h/2c	Average Measured Article Thickness, t
Monolithic (PW)	SL-12	2	Circular Hole	4	10	12 plies (0.094")
	SL-12	2 and 5	Saw Cut			
	SL-24	2 and 5	Saw Cut			24 plies (0.186")
	SL-24 with co-cured splice					

Notes: (1) The term 'SL' is a laminate identifier.

3.2 Materials

3.2.1 Carbon Fiber Prepreg

Table 3-2 describes in general the carbon/epoxy prepreg system used for the test article fabrication. The specific material system product used and its properties are proprietary and cannot be published in this thesis.

TABLE 3-2

CARBON FIBER/EPOXY PREPREG

General Material Type	Fiber Classification	Fabric	Yarn Filament Count	Resin Type	Fabric Areal Weight
Oven Cure Capable Carbon-Epoxy Prepreg System	Standard Modulus	Plain Weave	3000 (warp) 3000 (fill)	Epoxy	5.78±0.24$\frac{oz}{yd^2}$ (196±8gsm)

3.2.2 Carbon Fiber Reinforcement

Table 3-3 describes published properties of the continuous carbon fiber reinforcement that makes up the prepreg system in Table 3-2 from the material supplier.

TABLE 3-3

CARBON FIBER PROPERTIES

Fiber Type	Tow Ultimate Tensile Strength	Tow Tensile Modulus	Density
Standard Modulus Carbon Fiber	530ksi (minimum)	33Msi minimum average 37Msi maximum average	106.13pcf (1.7gcc)

3.2.3 Resin

The published properties of epoxy resin used in the make-up of the prepreg system are shown in Table 3-4.

TABLE 3-4

RESIN PROPERTIES

Resin Type	Tensile Modulus	Poisson's Ratio	Density
Toughened Epoxy	604ksi	0.4076	81.78pcf (1.31gcc)

3.3 Composite Manufacturing

3.3.1 Material Procurement

Prepreg materials used for test article fabrication were supplied by Cytec Engineered Materials Incorporated. All plain weave prepreg materials were evaluated via acceptance testing and receiving inspection testing to verify the materials quality and their acceptance to appropriate material specifications.

3.3.2 Ply Kitting

Ply kitting operations were performed on Gerber Technology® [17] ply cutter machines. Due to the size of the article, there were cases that ply overlaps were inevitable. This held true in the case of 65 inches high by 20 inches wide panels due to the prepreg width limitation of 42 inches wide. As a result, 0°/90° and 45°/-45° plies had to be spliced during the large test article fabrication.

A side tab was machined to be part of every machined ply kit. For ply count and stacking sequence verification, these tabs on the plies were visually inspected along with the use of other conventional verification methods, such as backing film and release paper count checks.

3.3.3 Laminate Lay-up

Using the pre-cut ply kits, each ply was laid up according to the laminate stacking sequence (or also known as ply table) as shown in Table 3-5. Instead of traditional laminate classifications of ‘soft’, quasi-isotropic or ‘hard’ laminates, the concept of Angled Minus Longitudinal (AML) was used. The AML concept is used to quantify the number of angled (±45°) plies in comparison to the longitudinal (0°) plies, with weighting functions based on cured ply thicknesses (CPT) and modulus values when laminates are made of various prepreg forms.

For the purpose of this study, since only one fabric form was used, a PW prepreg ply laid up in 0° direction would essentially only have half the amount of fibers in the 0° direction, while the other half of fibers would be in the 90° direction. Thus, the AML calculation can be further simplified as shown in Equation (21) for both types of laminates, SL-12 and SL-24.

TABLE 3-5

LAMINATE STACKING SEQUENCE

Laminate Type	AML	Stacking Sequence	No. of Plies	Average Measured Thickness (in)
SL-12	25	$[45/0_2/45/0/45]_s$	12	0.094
SL-24	25	$[45/0_2/45_2/0_2/45_2/0_2/45]_s$	24	0.186

$$AML = \%\ of\ \pm 45°\ Fibers - \%\ of\ 0°\ Fibers = 50\% - \frac{50\%}{2} = 25\% \tag{21}$$

Lay-up rosette directions (or known as lay-up reference directions) were marked on the aluminum lay-up table in the test article height direction as shown in Figure 3-3. The directions also serve as the material reference direction in finite element analyses.

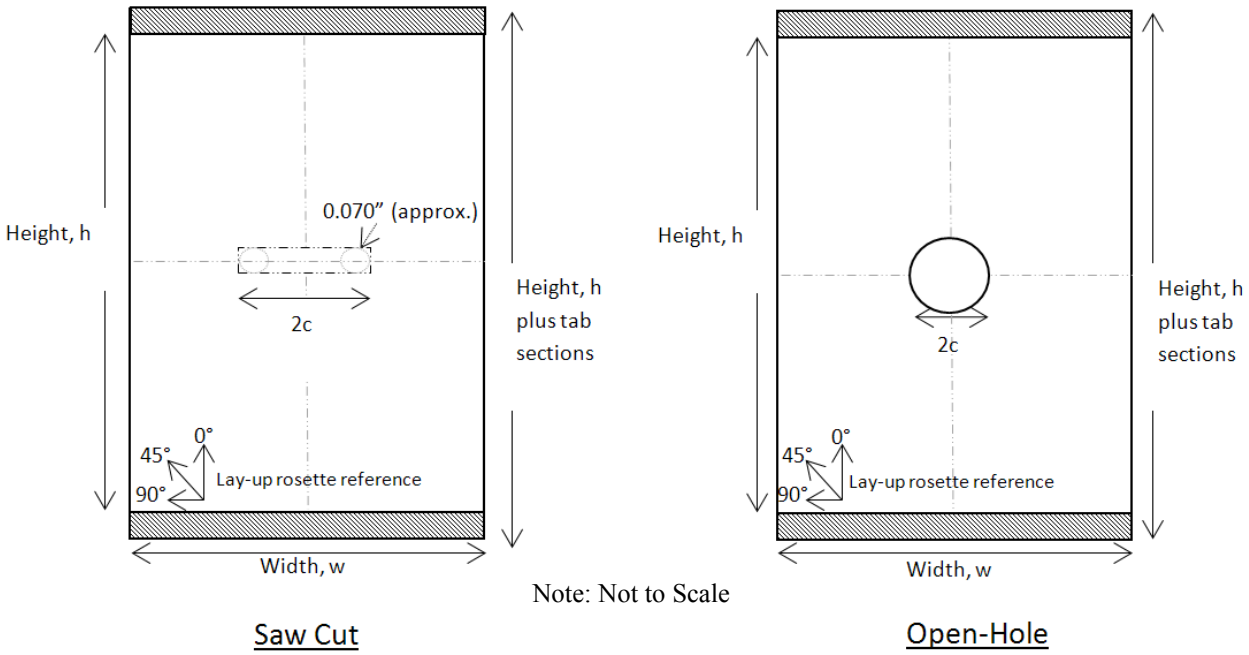

Figure 3-3 Test article configuration

Another design configuration tested was the co-cured splice configuration that has been more typical in aircraft design instead of secondary fastening or bonding of joints. The co-cured splice was achieved via gradual staggering of ply drop-offs across the joint as shown in Figure 3-4. In addition to the control of ply overlap tolerance, the butt-splicing gap between connecting plies at similar ply level or layer was also controlled to be within 0.050” to 0.080”. The nominal overlap dimension between plies was designed to be 0.750” minimum. Ply overlaps and butt-splice gaps in a co-cured splice are illustrated in Figure 3-5. Figure 3-6 shows the length of co-cured splice that was present on a test article via a Non-Destructive Inspection (NDI) C-scan image.

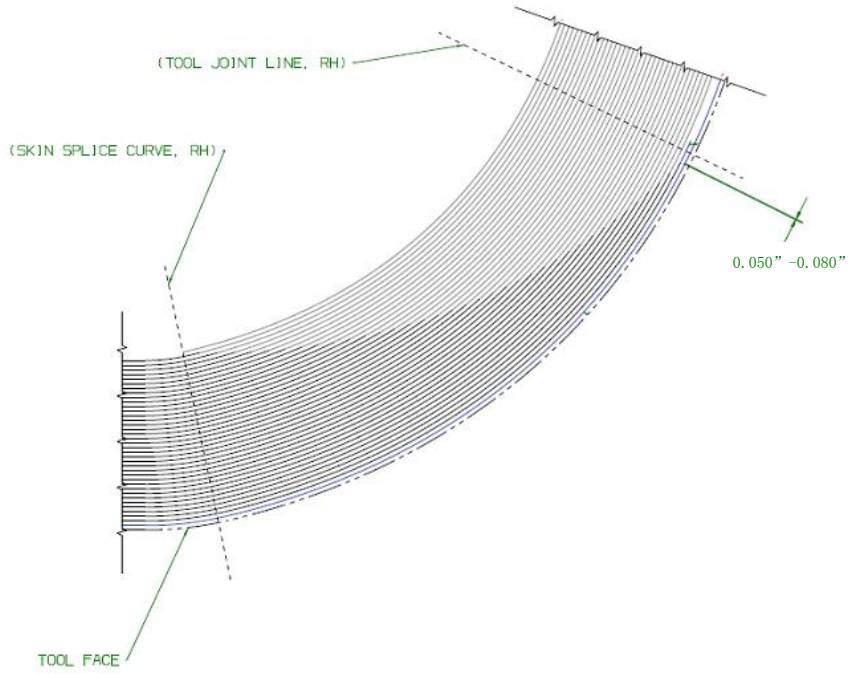

Figure 3-4 Co-cured splice configuration

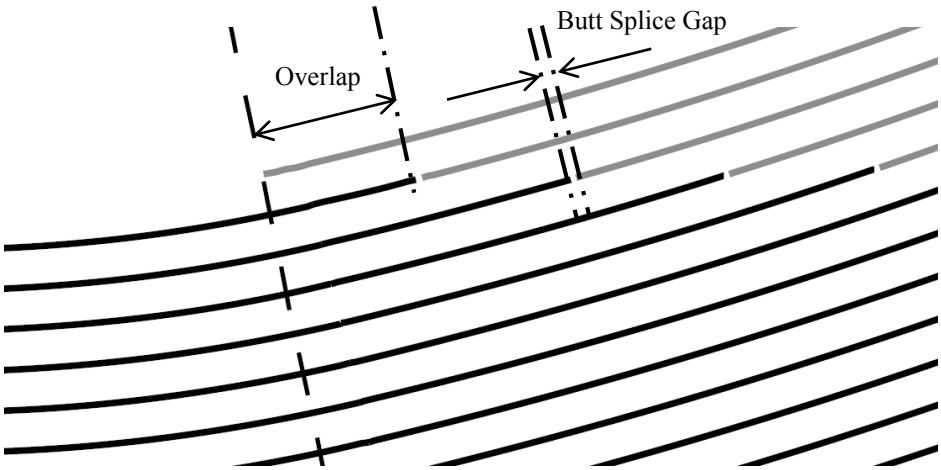

Figure 3-5 Overlap and butt-splice gap in plies

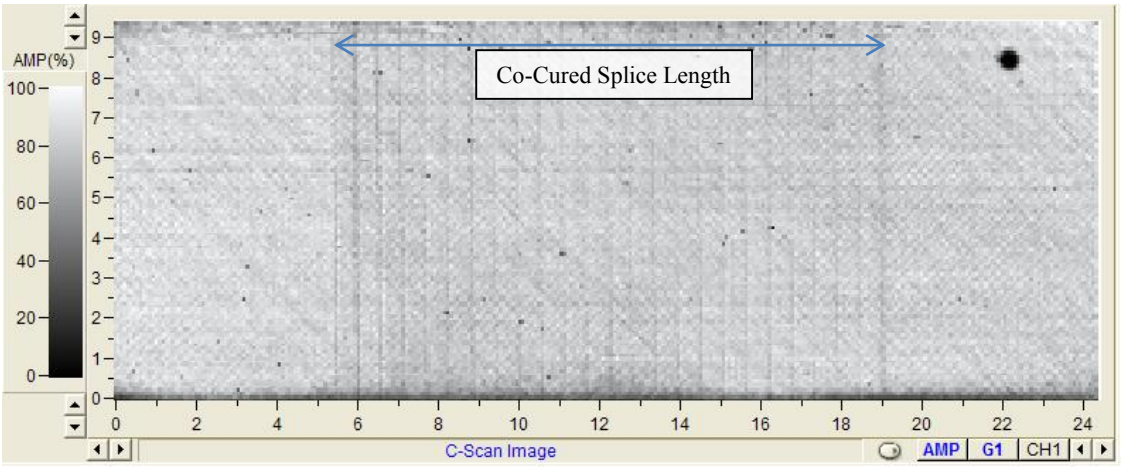

Notes: Scale is in inch.

Figure 3-6 NDI C-scan image of co-cured splice article

The first ply was laid up on a layer of solid release film. After the first four plies lay-up, the laid up laminate was debulked for at least 15 minutes with vacuum pressure. This intermediate debulking process was repeated for every subsequent four plies lay-up on the laminate with a minimum vacuum pressure of 24 inches of mercury (*inHg*). For laminate temperature monitoring during cure, two thermocouples were added at the mid-laminate thickness at least a quarter of an inch into the laminate from the edge. At the end of laminate lay-

up, the laminate was then covered with a release film layer, a peel ply layer, a breather layer, and a vacuum bagging film layer that were all part of the vacuum bagging scheme. The laminate edges were also covered with fiberglass yarns that serve as edge breathers. The laminate edges were then restrained with Teflon wrapped cured rubber dams. The general processing sequence is depicted in Figure 3-7.

The vacuum bag was then checked for any vacuum leak. With the vacuum line disconnected, the sealed laminate within the vacuum bag must have a leak less than two inHg in five minutes. If an acceptable vacuum leak result was found, the sealed laminate within the vacuum bag was further subjected to the final debulk operation in which the sealed laminate had to be under vacuum pressure for at least four hours. The intent was to remove as many air pockets as possible from the sealed laminate within the vacuum bag prior to cure.

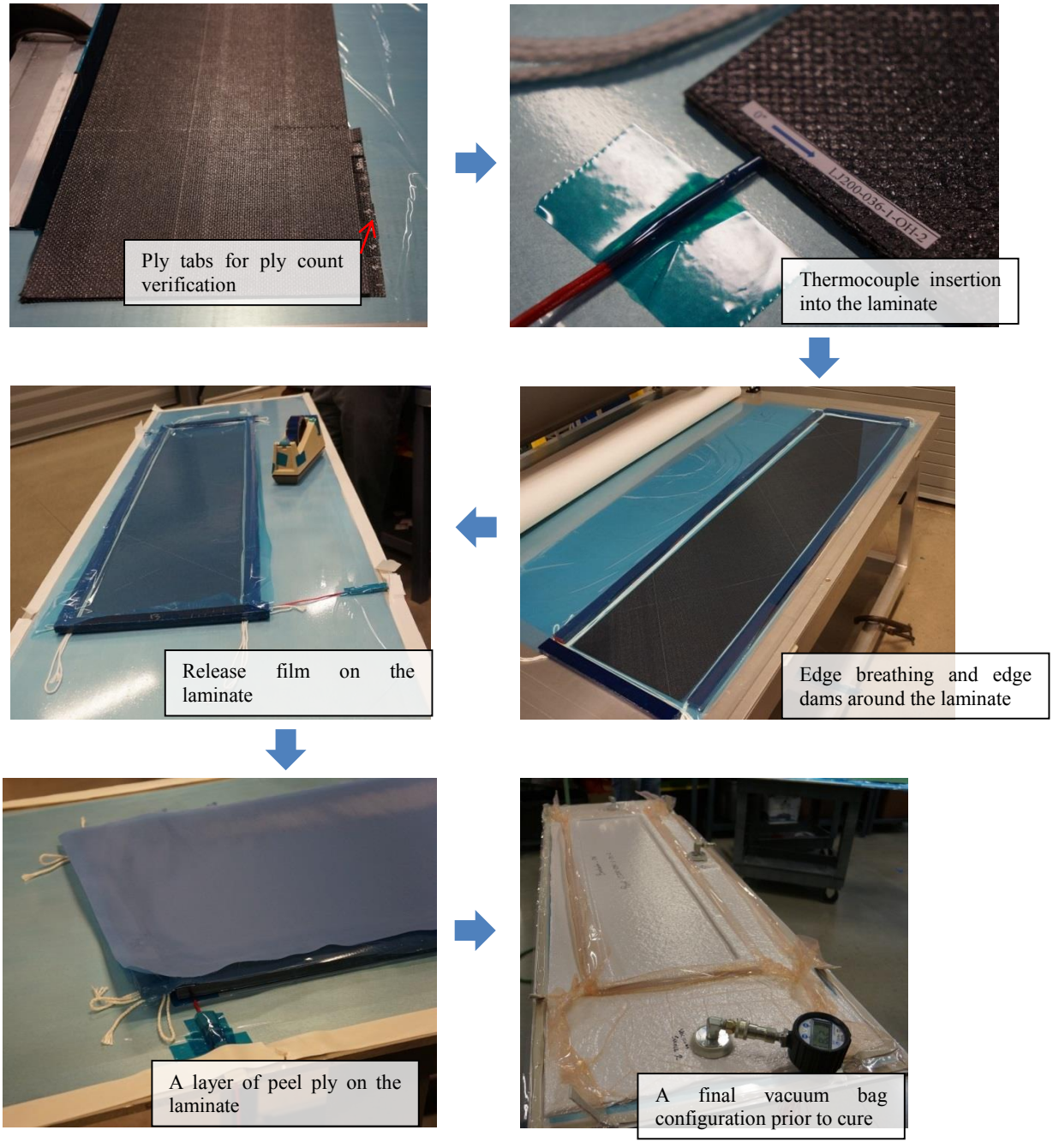

Figure 3-7 Composite manufacturing steps

3.3.4 Laminate Curing

After the final debulking operation, the sealed laminate within the vacuum bag was then transferred to the oven for the curing operation. Prior to the start of the cure, the sealed vacuum

bag was once again checked for leaks in its final placement within the oven. If the sealed vacuum leak rate was less than 2 inHg within five minutes, the laminate could proceed with the cure operation. The following cure schedule was followed:

1. From room temperature, part temperature was raised to 200°F±10°F at a target heat-up rate of 3°F/min.
2. At 200°F±10°F dwell, the part temperature was held for 6 hours nominal.
3. Then, the part temperature was raised to 290°F±10°F at a target heat-up rate of 3°F/min.
4. At 290°F±10°F dwell, the part temperature was held for two hours minimum.
5. The part was then cooled down to room temperature at a maximum rate of 5°F/min.
6. Vacuum level was ensured to be at least 24 inHg throughout the cure cycle.

3.3.5 Test Article Machining and Tabbing

After cure, all cured laminates were then rough cut to their specified final dimensions using the waterjet cutting operation for the small panels of eight inches wide and using a table saw for the large panels of 20 inches wide. The dimension tolerance at this stage was controlled to be within 0.100” from the final dimensions. Afterwards, fiberglass tabs were bonded at both ends of the test articles with AF 163-2 film adhesives to accommodate for the load transfer from the test fixtures to the test articles. This identical tabbing technique has also been used in typical ASTM test procedures such as ASTM D 3039 [18] as a mechanism of load transfer from the mechanical wedge fixture grips to the test article. The tabs also minimized the possibilities of specimen failure outside of gage sections and near to gripped regions. These tapered tabs provided stress reliefs at the transition areas between the test gage section and the gripped areas.

The film adhesives used to bond the tabs on the test articles were then cured at 250°F for 60 to 90 minutes. Exclusively for the large test articles of 20 inches wide, hole patterns were drilled through the tabbing sections of the articles for eventual bolted end grip configuration for testing. All test articles were then surface ground using Computer Numerical Control (CNC) machines to the final dimensions to be within 0.010" for width dimension and to be within 0.050" for height dimension.

Flaw details were subsequently machined depending on the flaw geometry. For saw cut flaw, the damage was initiated with two 0.070" small holes at two ends of the flaw length before the flaw geometry was finalized using a small end mill bit. The 0.070" dimension was chosen because it was still within typical composite machining capabilities and at the same time, because a high ratio of major axis dimension and minor axis dimension of the flaw could be retained such that the flaw was still representative of a narrow slit. The final flaw machining technique using water jet cutting operation, as adopted in Walker et al. [16], was not used in this study because of concerns about potential edge delamination from the machining operations and the machining precision. It must be noted that the actual saw cut flaw ends differ from the typical or ideal representation of saw cuts which generally is in rectangle shape. For an open hole flaw, the flaw end dimension was also finished using an end mill bit to provide a smooth flaw finish around the hole. Figure 3-8 provides an example of a test article undergoing the final flaw machining process on the CNC machine. Flaw end products of open hole and saw cut as machined are shown in Figure 3-9.

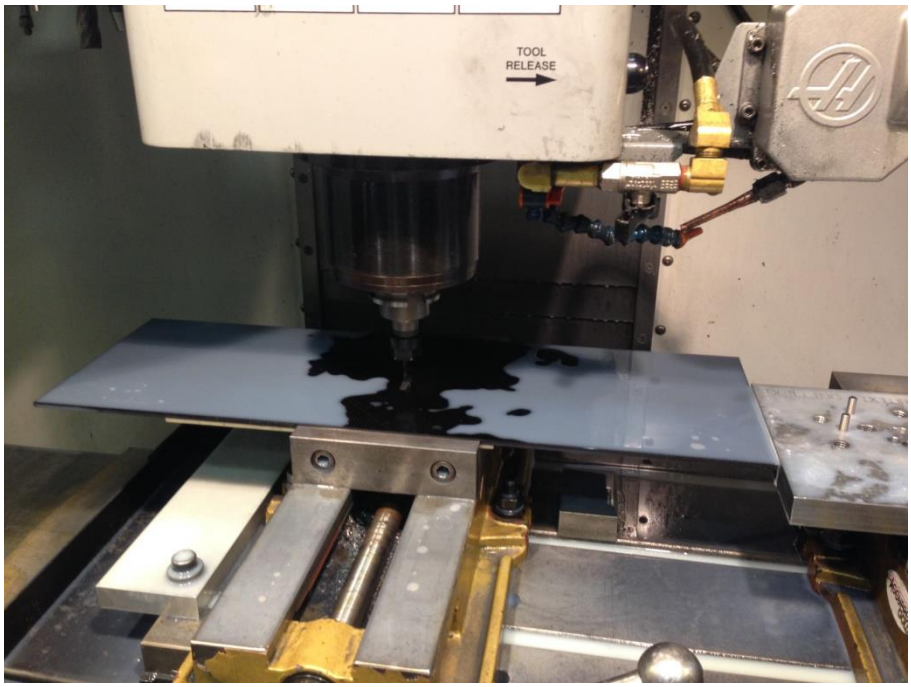

Figure 3-8 Test article in flaw machining process

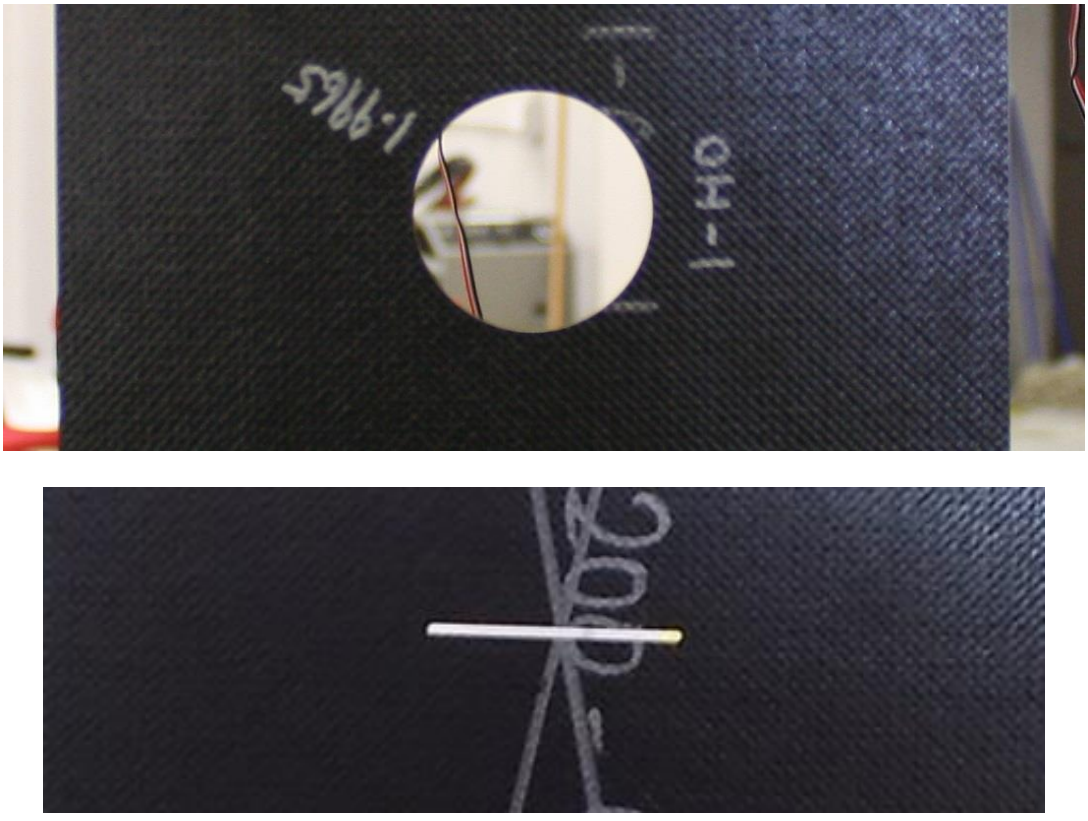

Figure 3-9 Flaw configurations

3.4 Test Article Identification

Test articles were identified with the identification scheme specified in Table 3-6.

TABLE 3-6

TEST ARTICLE CONFIGURATION

LJ200-036 - SC – 1 - 1

❶ ❷ ❸ ❹

Specimen identification

Field	Code	Description
❶ Test plan ID	036	Test plan identification
❷ Flaw ID	SC or OH	Flaw type identification
❸ Test ID	1, 2, 3 etc.	Test identification
❹ Specimen ID	1, 2, 3 etc.	Specimen identification

3.5 Non-Destructive Inspection

All the test articles were non-destructive inspected via ultrasonic inspection at the end of the cure and at the end of the machining processes. The Through-Transmission Ultrasonic (TTU) method was used to inspect for the following aspects:

1. Look for presence of any potential unintentional embedded flaws, foreign objects or delaminations within the test articles
2. Confirm the location of ply splices and co-cured splice joint feature
3. Check for the general laminate porosity level of the laminate

Prior to the NDI scans, the machine was calibrated to the polycarbonate glass reference standard and was set up to achieve at least 80% of backwall detection signal. The scan frequency of 5MHz was generally used for monolithic laminate NDI scans. A sample of NDI settings and

examples of NDI scans from the ultrasonic inspections are depicted in Table 3-7 and Figure 3-10 respectively.

TABLE 3-7

NDI CONFIGURATION SETTINGS

EQUIPMENT					
UT Instrument Manufacturer:	NDT Automation	Flaw Detector Manufacturer:	NDT Automation	Nozzle Size:	0.25 in dia
UT Instrument Model:	NDT Squirter System	Flaw Detector Model:	NDT Automation	Couplant:	Clean water
SCAN PARAMETERS					
Scan Speed:	8 in/s	Scan Index:	0.08 in	Scan Mode:	TTU C-Scan
UT PARAMETERS					
Gain*:	1.8 dB	Sound Velocity	0.1170 in/us	Gate Type:	Gate 1
Frequency:	5 MHz	Damping:	200 Ohm	Gate Width:	0.6 in
Transducer:	Standard Flat	Voltage:	250V	Gate Level:	65% threshold
Range:	2.5 in	Delay:	3.42 in	Gate Position:	4.73 in
** Adjust the gain such that Gate 1 shows 80% full screen height signal*					

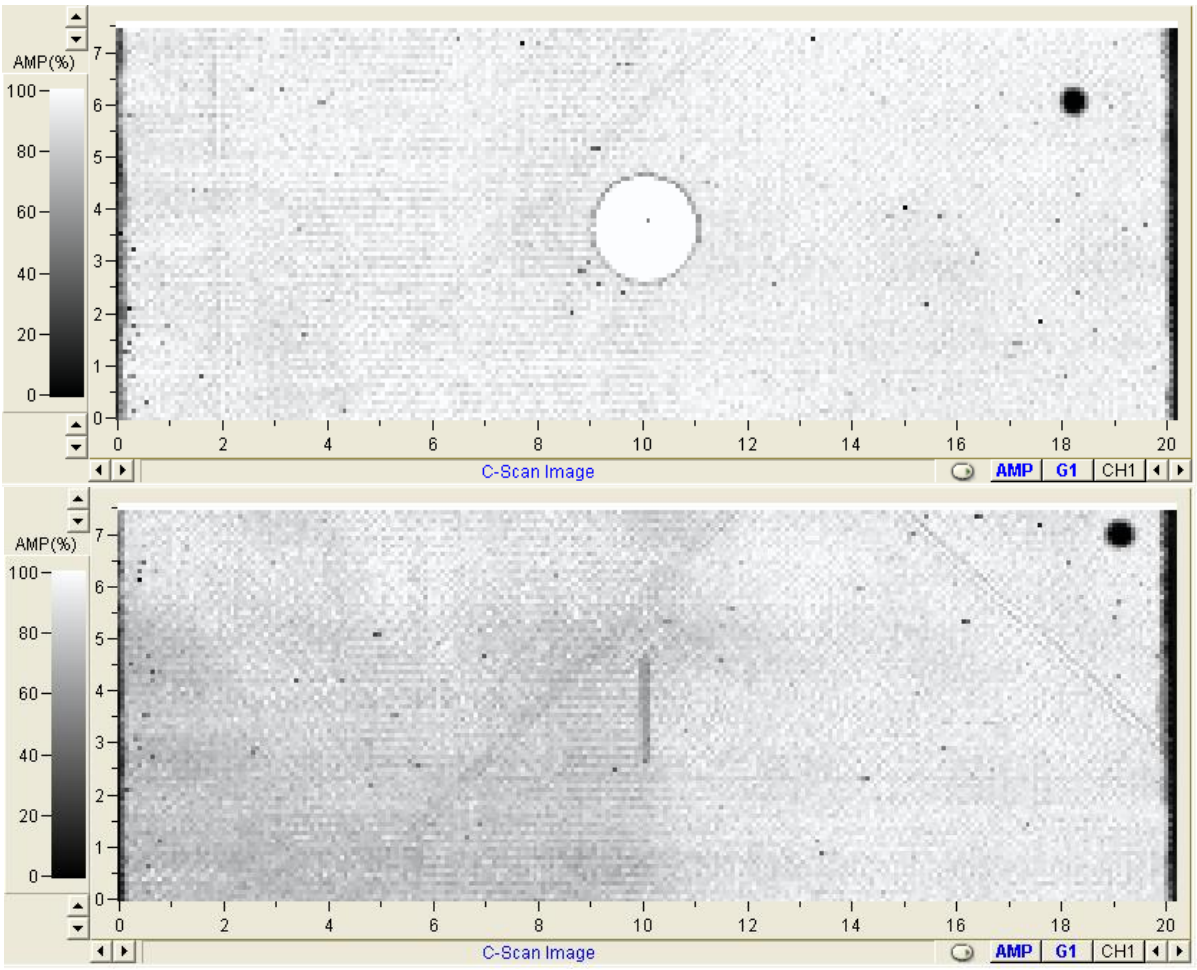

Notes: Scale is in inch.

Figure 3-10 NDI C-scans of test articles

3.6 Testing

3.6.1 Test Matrix

Table 3-8 presents the test matrix within the scope of results presented within this thesis.

3.6.2 Test Environment and Conditioning Requirements

Test Conditions/Environments

Two test conditions were tested:

RTA = Room Temperature Ambient, test temperature at 70°F ± 10°F, as-fabricated specimen moisture content

CTD = Cold Temperature Dry, test temperature at -94°F ± 5°F, dry moisture content.

Specimen Moisture State

Ambient = Specimens were in as-fabricated moisture state

TABLE 3-8

TEST MATRIX

Test Type	Test ID	Flaw Type	Flaw Length, 2c (in)	Laminate	AML	No. of Plies	Test Article Gage Height (in)	Total Test Article Height (in)	Test Article Width (in)	Test Condition[(1)]	No. of Specimens
Tension Fracture Strength Test	1	Circular Hole	2.0	SL-12	25	12	20	34.5	8	RTA	3
	2	Saw Cut	2.0	SL-12	25	12	20	34.5	8	RTA	3
	3	Saw Cut	2.0	SL-12	25	12	20	34.5	8	CTD	3
	5	Saw Cut	2.0	SL-24	25	24	20	34.5	8	RTA	3
	6	Saw Cut	2.0	SL-24 Co-cured Splice	25	24	20	34.5	8	RTA	3
	7	Saw Cut	5.0	SL-12	25	12	50	64.8	20	RTA	1
	8	Saw Cut	5.0	SL-24	25	24	50	64.8	20	RTA	1
										Total Tested	17

Notes:

(1) Test conditions: RTA = Room Temperature Ambient, test temperature at 70°F ± 10°F and specimen in as-is moisture content state.

CTD = Cold Temperature Dry, test temperature at -94°F ± 5°F, dry moisture content.

3.6.3 Test Instrumentation and Fixturing

All test articles had two rosette strain gages mounted near to the flaw details and three axial strain gages at far-field locations for various verification purposes that will be described later. Details of strain gages used are shown in Table 3-9:

TABLE 3-9

STRAIN GAGE DETAILS

Strain Gage Type	Strain Gage Designation	Resistance (Ω)	Supplier
Rosette	CEA-06-250UR-350	350±0.4%	Vishay Precision Group
Axial	CEA-06-250UW-350	350±0.3%	

For tension test articles, the strain gage layout and strain gage channel numbering scheme used are depicted in Figure 3-11 for open hole, and in Figure 3-12 and Figure 3-13 for saw cut depending on test article sizes.

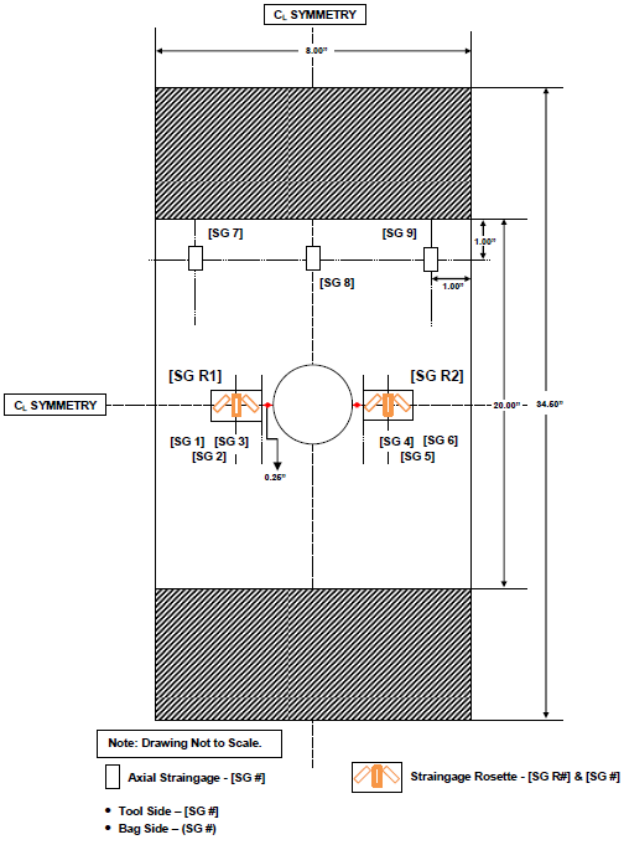

Figure 3-11 Strain gage layout for 8-inch wide article (open hole)

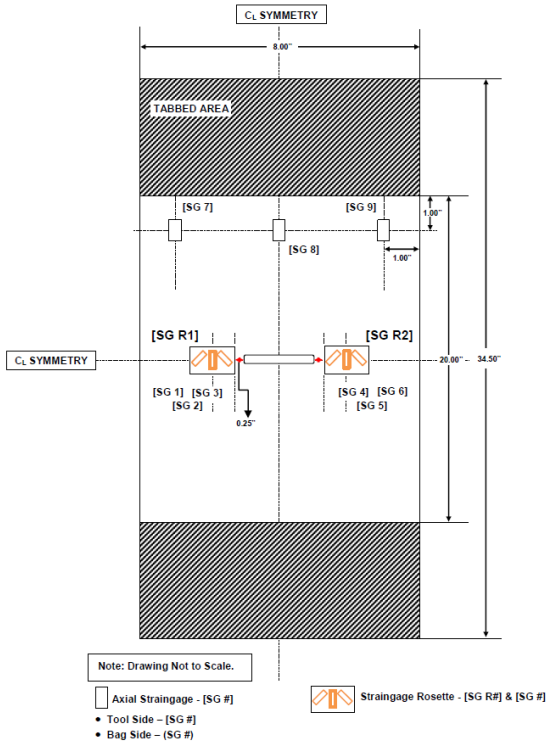

Figure 3-12 Strain gage layout for 8-inch wide article (saw cut)

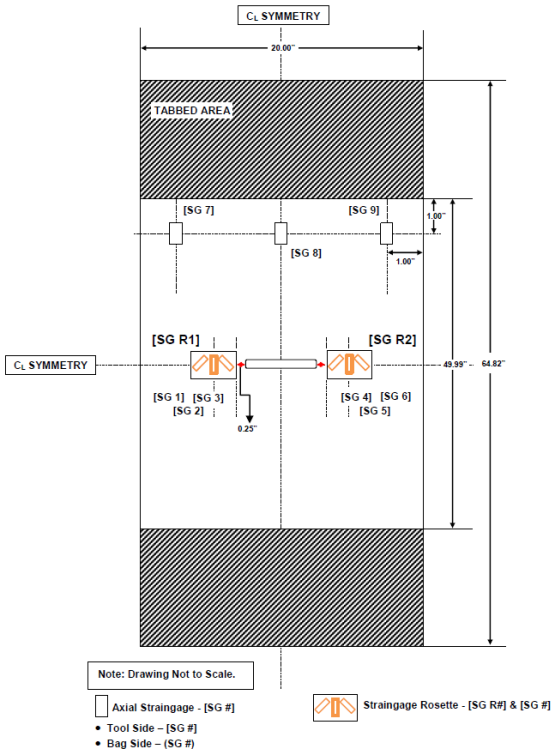

Figure 3-13 Strain gage layout for 20-inch wide article (saw cut)

Local strain readings around the flaw detail and around crack tip regions were continuously captured throughout the test using two rosette strain gages that were installed 0.25" away from the flaw ends. For tension fracture test specimens, three axial strain gages were installed at top end of the test article, one inch away from the tabbed area. Due to the width limitation on the tension hydraulic wedge grips, which were only six and a half inches in width, small tension articles of eight inch wide were not entirely gripped across the width. Figure 3-14 and Figure 3-15 illustrate the gripped areas on the hydraulic tension wedges and the imprints of gripped areas on a tested test article which show that there was half inch overhang (ungripped area) on each side of the specimen. Thus, three axial strain gage readings were used to gage whether there was any variation in loading across the width of the test article. For all test cases, it was found that the variation in between the far-field axial strain readings was low.

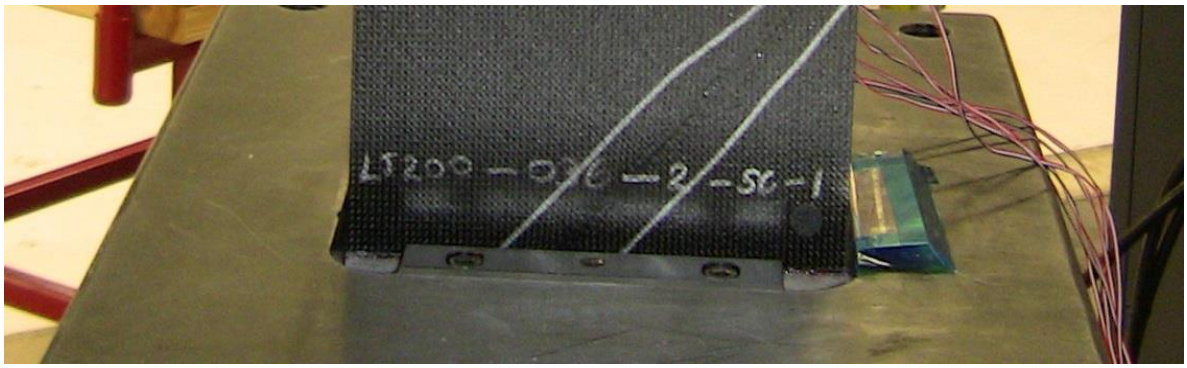

Figure 3-14 Hydraulic wedge grip width

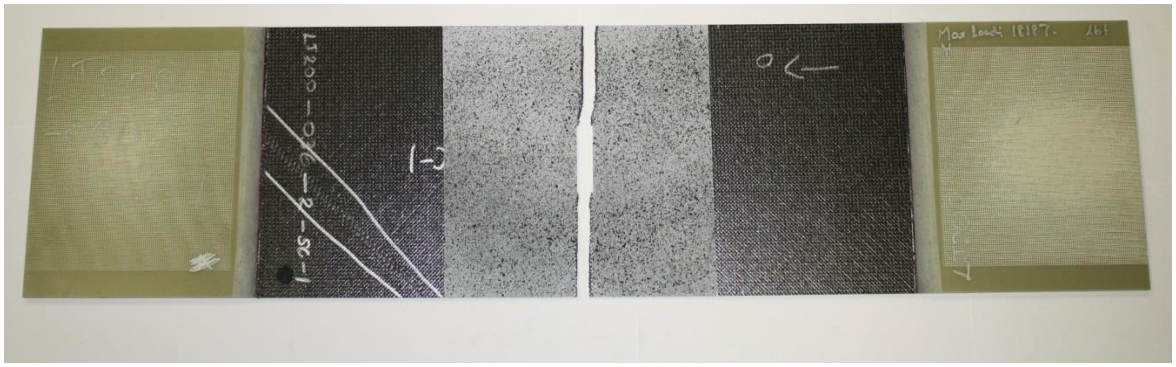

Figure 3-15 Imprints of gripped areas on end tabs

For large tension test articles, a bolted end plate fixture design connected to an end clevis was selected for test article clamping due to higher failure load requirements. Three rows of varying bolt diameters were adopted to distribute the loads from the test fixtures to the test articles.

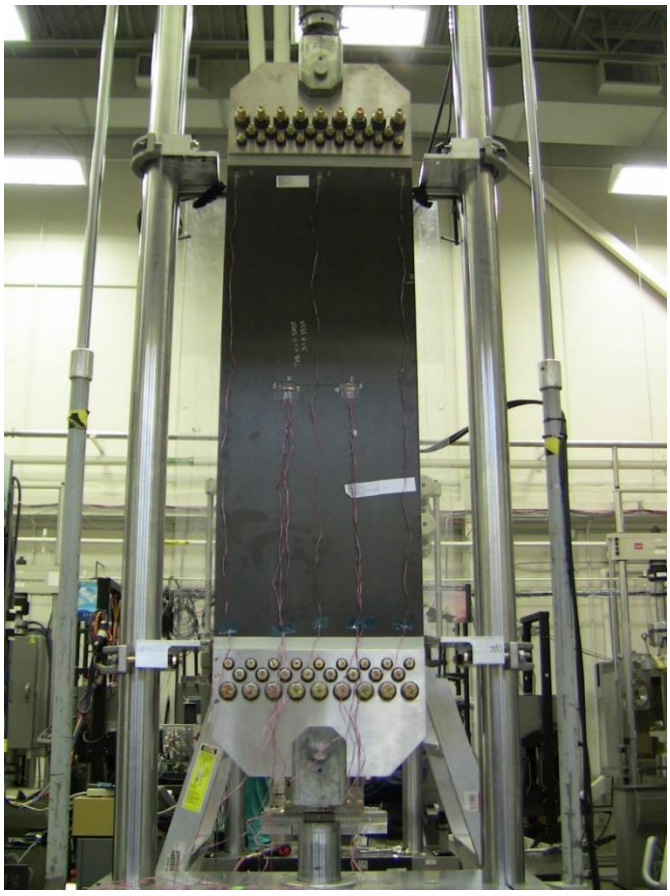

Figure 3-16 Bolted plate end fixture to clevis design

For global strain monitoring around the flaw details, the GOM ARAMIS® photogrammetric strain measurement system [19] was used to further map out strain response around flaw details in at least one test article from each tension fracture test ID. The ARAMIS® 3D 5M system was used with optimal camera resolution of 2448x2050 pixels and strain measuring accuracy up to 0.005% [19].

Speckle paint pattern was sprayed on the opposite side from the strain gaged surface of the test article covering about ten inches in height, centered on the flaw details. Strain measurements were captured at selected load points or intervals until the end of the test. The strain measurements from photogrammetric strain measurement system and strain gages were useful for subsequent comparison and correlation back to finite element analysis responses. An example of speckle pattern used on the test article is shown in Figure 3-17.

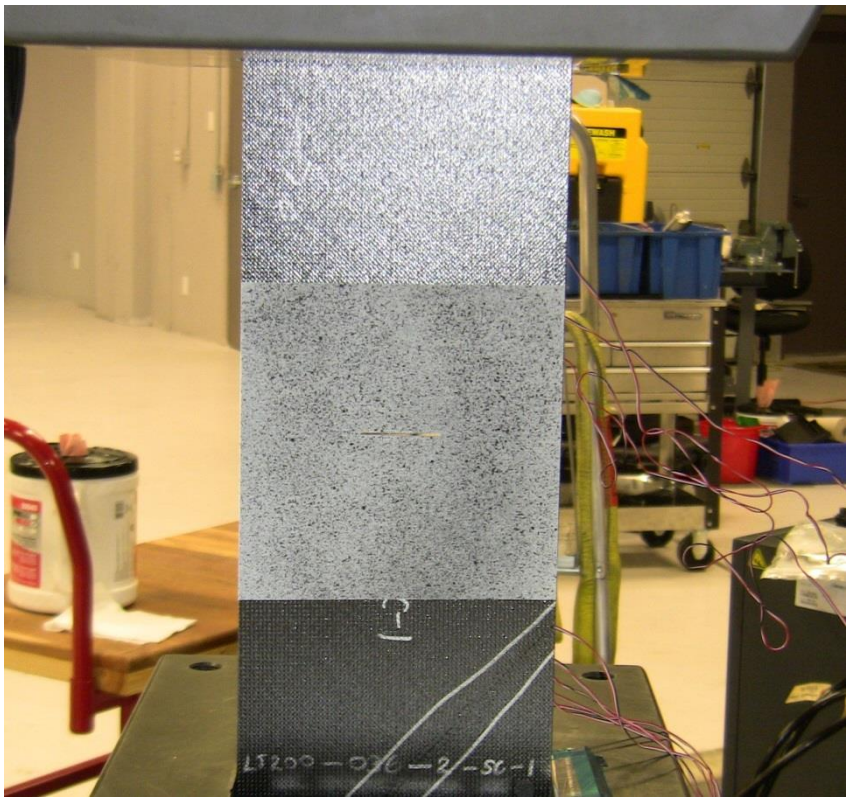

Figure 3-17 Photogrammetric speckle paint pattern

3.6.4 Test Setup

Test Machine (Small Tension Test Article)

For small tension test articles, a MTS 500-kip axial torsion load frame at the NIAR Aircraft Structural Test and Evaluation Center (ASTEC) was selected primarily because of its large hydraulic tension grips and its gripping range capability. Even though the test article's full width was eight inches wide, the acceptability of the use of smaller grip was justified with the verification that differences between far field strains recorded via three axial strain gages across the article width were very small across all test cases. A photograph of the test setup is shown in Figure 3-18.

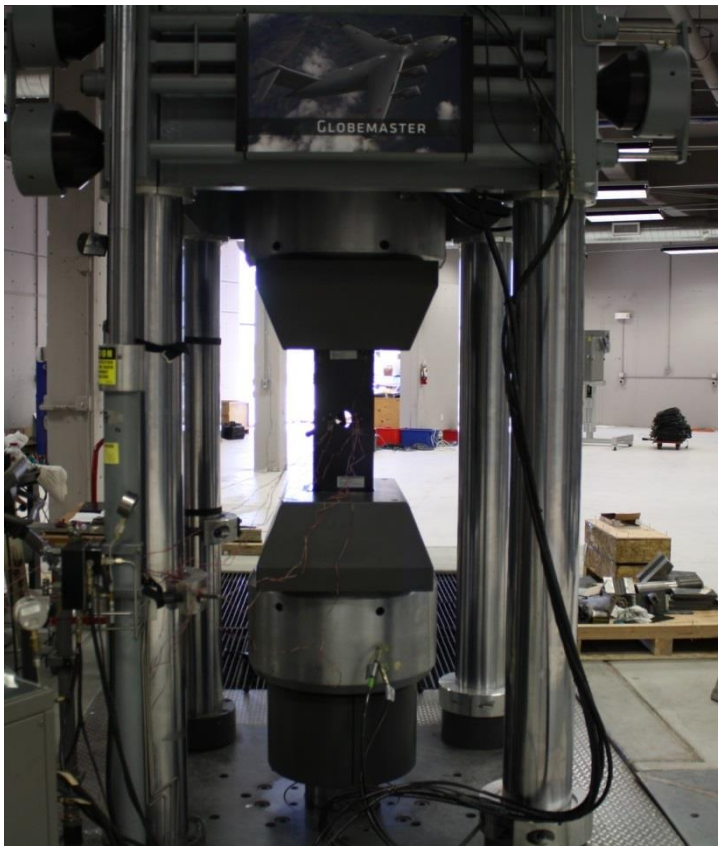

Figure 3-18 500 kip axial-torsion load frame

Another concern was in the loading accuracy since the load cell used was capable of applying 500kip maximum, which was well beyond the recorded failure loads for all small test articles that ranged from 15kip to 20kip. Typical load cell accuracy or repeatability was rated at 0.1%, thus implying that the load cell accuracy for this case was within 500lb which seemed to be high especially for the 15kip to 20kip failure loads recorded. The decision to proceed with the test using the current machine was made because the load cell had been calibrated to be within 100lbs for the first 100kip range of the load cell. Based on this, the results were not expected to deviate much should a lower load capacity load cell be used.

Test Machine (Large Tension Test Article)

For large tension test articles, a MTS 100-kip machine at the NIAR Wichita State University (WSU) campus was selected primarily due to its large actuator displacement range, in order to accommodate about a 65-inch long total test article height. Because of the 20 inches wide dimension and the expected failure load of 30kip to 60kip prior to test, the use of hydraulic wedge grips was not an option. The alternate was the use of clevis connected to bolted plate fixtures that would be clamping the test article ends. A photo of the test setup is shown in Figure 3-19.

Figure 3-19 100 kip axial load frame

3.6.5 Test Procedures

Tension fracture strength tests were performed in the following test sequence:

1. Prior to the start of test on a given day, each test setup was calibrated with a metallic reference standard test article to ensure that the test setup was functioning as expected and that no torsion loads were applied on the test article. This step

was particularly critical on the axial-torsion load frame since the test frame was capable of applying two modes of loads simultaneously.

2. The test article was then inserted in between the hydraulic wedge grips or bolted plate fixture depending on the test article size. For hydraulic wedge grips, the grip pressure was set to 3000psi.
3. Strain gages and actuator deflection were then zeroed. Photos were taken prior to the start of test for record. The preload value was also recorded.
4. Tensile load was then applied at a constant loading rate of 0.02 inch per minute to simulate quasi-static loading with continuous strain gage data collection and intermittent ARAMIS strain measurements at selected load intervals.
5. The first audible crack during the test was recorded as a reference, typically indicative of fiber failure initiation. Each test article was loaded to the ultimate failure and the maximum load applied was recorded.
6. After the completion of the test, test data were saved electronically for analysis. Photos of tested articles were taken for record prior to removal of the test article from the test fixture.

3.7 Summary of Experimental Results

Summaries of test results and their analysis are presented in the following sub-sections. Photographs of tested articles are included in Appendix A. Progressions of strain response throughout the test can be observed on the ARAMIS photogrammetric scans as shown in Appendix B.

These sections present as-measured values as well as normalized values to unnotched properties. Two types of strain data are reported for comparison and their location details are presented in Table 3-10 and illustrated in Figure 3-20.

TABLE 3-10

STRAIN MEASUREMENT LOCATION DETAILS

Strain Measurement	Strain Gage(1)	ARAMIS Photogrammetric(2)
Near Flaw Strain	1/4” away from crack tip on each side	Next to flaw tip
Far-Field Strain	1” away from tabbed area	5” away from the centerline of flaw

Notes:

(1) Strain gage lay-out schemes are based on strain gage instrumentation figures illustrated in Section 3.6.3. The middle strain grid of the rosette strain gage is approximately 3/8” away from the strain gage film edge. The two outer 45 degree grids were approximately 1/8” away from the strain gage film edge.

(2) ARAMIS system is not able to detect strain output close to the edge. The masked out area is about 0.020” to 0.025” away from the specimen or flaw periphery.

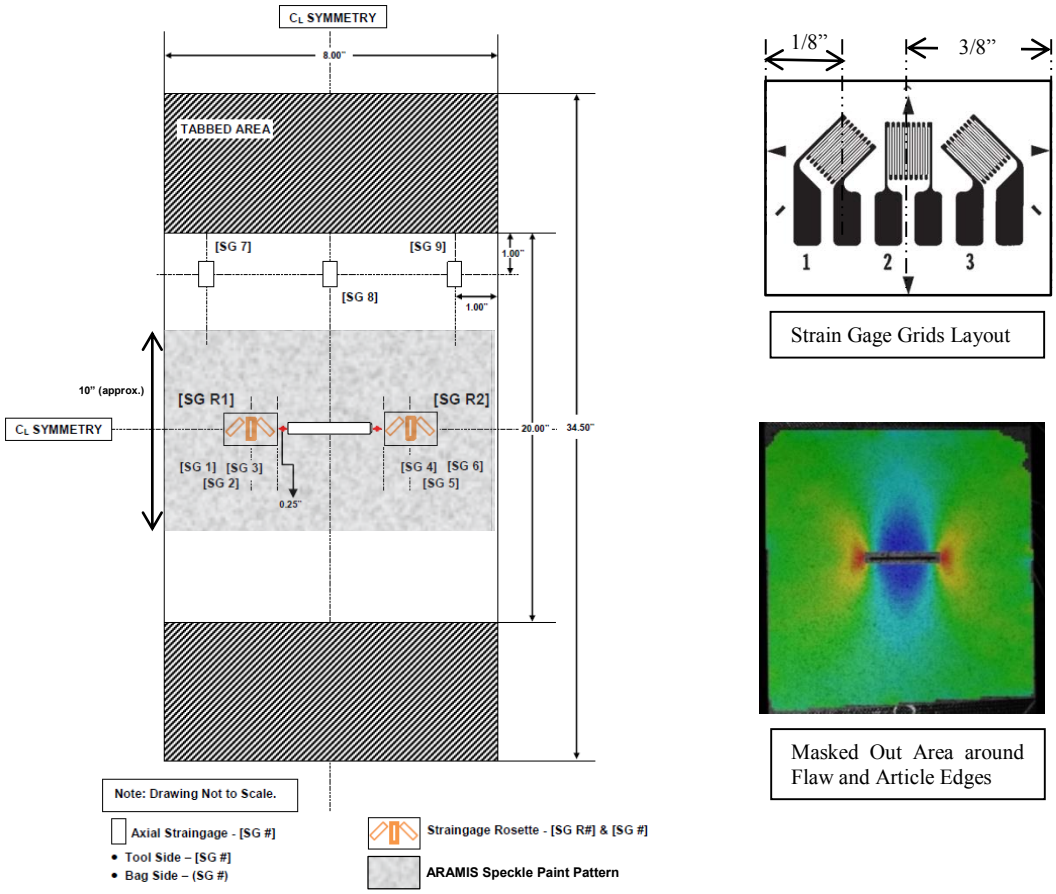

Figure 3-20 Strain monitoring instrumentation details

Additionally, there are differences in strain measurement time frames between strain gages and ARAMIS photogrammetric measurements as shown in Table 3-11 when reported in this section. Thus, it must be emphasized that should there be significant differences in near flaw and far-field maximum strains reported, these differences must be due to the differences in terms of locations on the test article and also the time frames from which the strain readings were reported.

TABLE 3-11

STRAIN MEASUREMENT TIME FRAME DETAILS

Strain Measurement	Strain Gage	ARAMIS Photogrammetric
Near Flaw Strain	At maximum load	The nearest strain scan prior to failure[(1)]
Far-Field Strain		

Notes: (1) Strain scans were performed at selected load intervals. In all test cases, the maximum difference between the final load interval and the maximum load record was about 1000lbs.

The maximum ARAMIS readings from selected test articles at the last load point are reported for each test ID for reference. The source of the reported ARAMIS data is also noted in each table. Meanwhile, for strain gage readings, maximum strain values were aggregated across all tested articles and available strain gages on the test articles. Detailed comparisons between the two sources of experimental strain outputs along with Finite Element Methods (FEM) calculated strains will be presented in Chapter 5.

Similarly, for loads and strength values, the reported values are the average values of all tested articles within each test ID. Furthermore, whenever possible, the load reading at which the first audible noise/tick occurred is also reported for reference.

3.7.1 Tension Test Results

Two-Inch Open Hole, SL12 Laminate

Table 3-12 provides test results summary for the control case, a two-inch long open hole flaw on a SL-12 laminate. It can be observed that the standard deviation is really low. From the strain outputs comparison, the differences are rather large where the difference is about 14% for far-field strains and about 22% for near flaw strains.

TABLE 3-12

TEST RESULTS SUMMARY (2-INCH OPEN HOLE, SL12)

	Open Hole-SL12 Laminate Test ID 1		RTA	
			Measured	Normalized
Tension Fracture Strength Test	Tension Strength	Mean [psi]	34809	0.329
		Standard Deviation [psi]	1031	0.010
		Coefficient of Variation [%]	2.96	2.961
		Minimum [psi]	34084	0.322
		Maximum [psi]	35989	0.340
		Number of Samples	3	3
		Number of Batches	1	1
	Near Flaw Max Strain	Strain Gage [με]	6754	0.446
		ARAMIS(1) [με]	8680	0.573
	Far-Field Max Strain	Strain Gage[με]	4904	0.324
		ARAMIS(1) [με]	4240	0.280
	Load	First Audible Crack [lbs]	24500	0.936
		Maximum [lbs]	26177	1

Notes: (1) ARAMIS reading was captured from 036-1-OH-2 article at 25,000lbs load level (Stage 15).

Two-Inch Saw Cut, SL12 Laminate

Table 3-13 provides the test results summary for the two-inch saw cut flaw on SL-12 laminate across two test environments, RTA and CTD. It can be observed that the difference in tension strengths between these two environmental conditions is very minimal, at 1.1%. Similar to the control case, strain output differences are rather large.

TABLE 3-13

TEST RESULTS SUMMARY (2-INCH SAW CUT, SL12)

	2" Saw Cut-SL12 Laminate Test ID 2 and 3		RTA		CTD	
			Measured	Normalized	Measured	Normalized
Tension Fracture Strength Test	Tension Strength	Mean [psi]	24640	0.233	23204	0.222
		Standard Deviation [psi]	706	0.007	209	0.002
		Coefficient of Variation [%]	2.86	2.864	0.90	0.899
		Minimum [psi]	24185	0.229	23045	0.221
		Maximum [psi]	25453	0.241	23440	0.225
		Number of Samples	3	3	3	3
		Number of Batches	1	1	1	1
	Near Flaw Max Strain	Strain Gage [με]	4578	0.302	4276	0.286
		ARAMIS [με]	6707(1)	0.443	-(2)	-
	Far-Field Max Strain	Strain Gage [με]	3509	0.232	3290	0.220
		ARAMIS [με]	2647(1)	0.175	-(2)	-
	Load	First Audible Crack [lbs]	12900	0.696	-(2)	-
		Maximum [lbs]	18529	1	17449	1

Notes:

(1) ARAMIS reading was captured from 036-2-SC-1 article at 18,000lbs load level (Stage 21).

(2) ARAMIS reading and first audible crack point could not be captured from CTD articles because of articles placement in the environmental chamber during the tests.

Two-Inch Saw Cut, SL24 Laminate

Table 3-14 provides the test results summary for two-inch saw cut flaw on the thicker SL-24 laminate with the comparison between pristine laminate and laminate with co-cured splice. It can be concluded that there is no strength reduction from having the co-cured splice in the test article, as is normally feared.

TABLE 3-14

TEST RESULTS SUMMARY (2-INCH SAW CUT, SL24)

	2" Saw Cut-SL24 Laminate vs with Co-Cured Splice Test ID 5 and 6		RTA		RTA	
			Measured	Normalized	Measured	Normalized
Tension Fracture Strength Test	Tension Strength	Mean [psi]	22901	0.216	23926	0.226
		Standard Deviation [psi]	489	0.005	643	0.006
		Coefficient of Variation [%]	2.13	2.133	2.69	2.687
		Minimum [psi]	22352	0.211	23355	0.221
		Maximum [psi]	23286	0.220	24623	0.233
		Number of Samples	3	3	3	3
		Number of Batches	1	1	1	1
	Near Flaw Max Strain	Strain Gage [με]	4157	0.274	4239	0.280
		ARAMIS [με]	6306(1)	0.416	5760(2)	0.380
	Far-Field Max Strain	Strain Gage [με]	3140	0.207	3288	0.217
		ARAMIS [με]	3381(1)	0.223	2970(2)	0.196
	Load	First Audible Crack [lbs]	25633	0.752	26933	0.757
		Maximum [lbs]	34077	1	35602	1

Notes:

(1) ARAMIS reading was captured from 036-5-SC-2 article at 32,000lbs load level (Stage 17).

(2) ARAMIS reading was captured from 036-6-SC-3 article at 35,000lbs load level (Stage 20).

Five-Inch Saw Cut, SL12 Laminate

Table 3-15 provides the test results summary for the five-inch saw cut flaw on SL-12 laminate. There is only one reported data point and no ARAMIS output available for this test ID.

TABLE 3-15

TEST RESULTS SUMMARY (5-INCH SAW CUT, SL12)

	5" Saw Cut-SL12 Laminate		RTA	
	Test ID 7		Measured	Normalized
Tension Fracture Strength Test	Tension Strength	Mean [psi]	15191	0.144
		Number of Samples	1	1
		Number of Batches	1	1
	Near Flaw Max Strain	Strain Gage [με]	3537	0.244
	Far-Field Max Strain	Strain Gage [με]	2112	0.146
	Load	First Audible Crack [lbs]	22500	0.756
		Maximum [lbs]	29775	1

Five-Inch Saw Cut, SL24 Laminate

Table 3-16 provides the test results summary for the five-inch saw cut flaw on thicker SL-24 laminate. Similar to test ID 7, there is only one data point reported.

TABLE 3-16

TEST RESULTS SUMMARY (5 INCH SAW CUT, SL24)

	5" Saw Cut-SL24 Laminate		RTA	
	Test ID 8		Measured	Normalized
Tension Fracture Strength Test	Tension Strength	Mean [psi]	15433	0.146
		Number of Samples	1	1
		Number of Batches	1	1
	Near Flaw Max Strain	Strain Gage [με]	3741	0.258
	Far-Field Max Strain	Strain Gage [με]	2093	0.144
	Load	First Audible Crack [lbs]	38000	0.638
		Maximum [lbs]	59570	1

3.7.2 Tension Failure Mode

In all tension test cases, failures started from the flaw periphery at the mid-height of the flaw and rapidly propagated across the whole article width at the ultimate load application resulting in test article separation as shown in Figure 3-21. In contract to metallic materials, there was no gradual crack propagation observed throughout the test prior to ultimate failure.

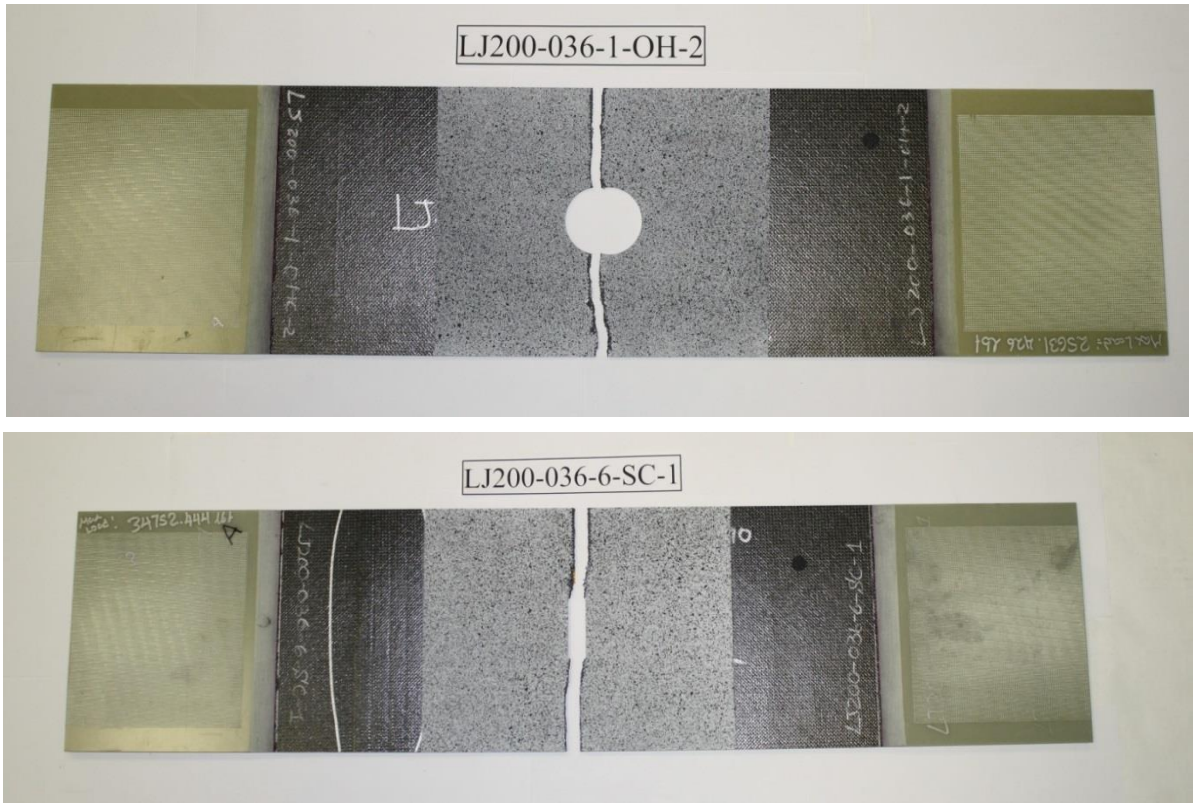

Figure 3-21 Fracture tension-failure mode

3.8 Discussion of Experimental Test Results

3.8.1 Tension Strength

In general, tension fracture test data yielded a very low coefficient of variation within each test ID. Figure 3-22 presents the average tension strength across all the tests. Several noticeable trends can be observed from the average tension strength trends across the test IDs, as shown in Figure 3-22. Tension strength of the laminate showed a 29% drop when flaw type was

varied from open hole to saw cut type and all other test variables were fixed. In addition, the strength reductions from the increased size of saw cuts between both laminate thicknesses tested seem to be similar. It was initially thought that the tension fracture strength in thin laminates would be lower than that in thicker laminates due to possible out-of-plane bending from grips during testing. The data, however, show that the fracture strength in thicker laminate is slightly lower than that in thin laminate for about 7% at RTA environment for pristine laminate case. A smaller difference of 2.8% is found in between the average fracture strength of pristine SL-12 laminate and that of co-cured splice SL-24 laminate.

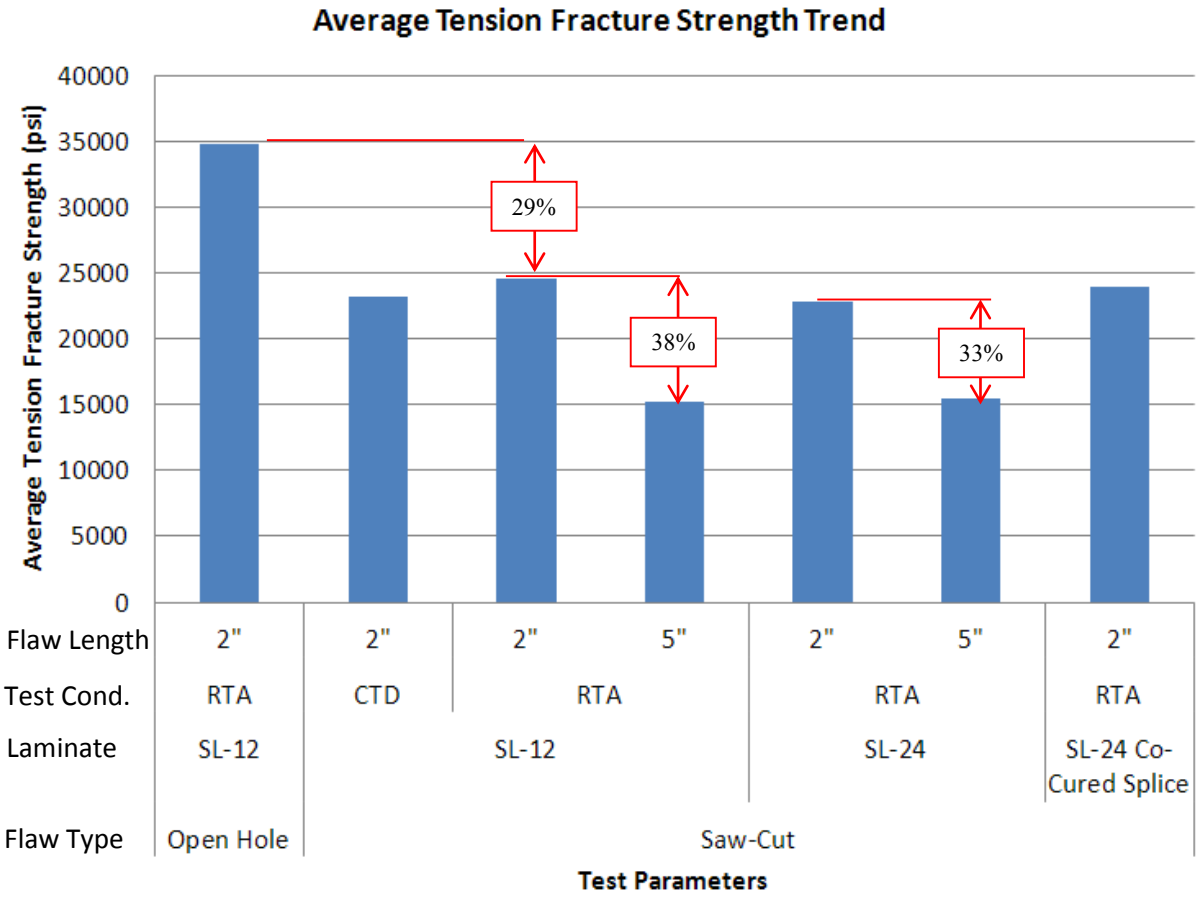

Figure 3-22 Fracture tension-average tension strength distribution

On the other hand, Figure 3-23 illustrates near flaw average max strain from the strain gages across the tests respectively. The reduction in tension fracture strengths from the flaw size increase previously observed, however, does not translate into a similar trend of near flaw max strain reductions across the two laminates tested, as illustrated in Figure 3-23.

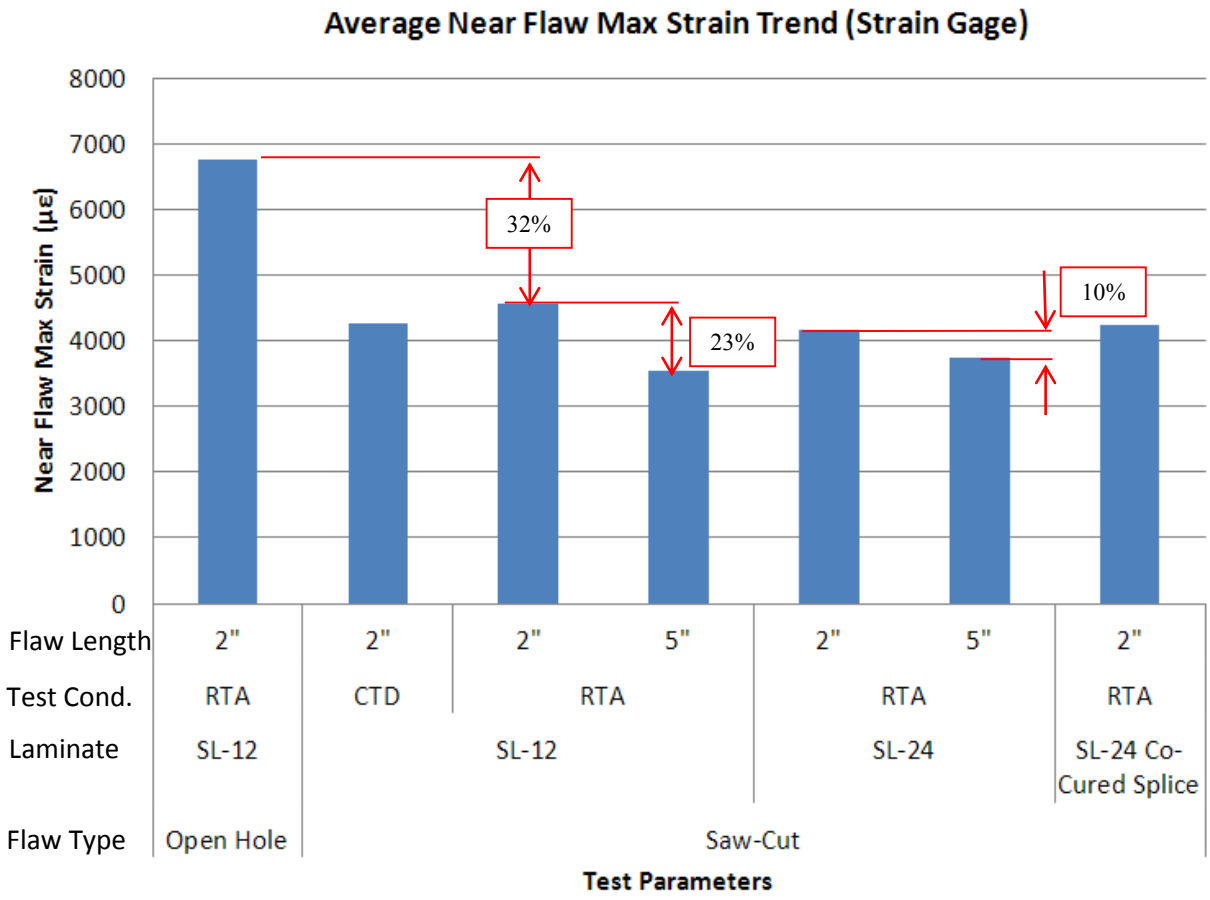

Figure 3-23 Fracture tension-average near flaw max strain distribution

CHAPTER 4

ANALYTICAL STUDY

Stress analyses around circular holes have long been studied and the stress concentration around the flaw is well understood. However, the complexity factor increases when dealing with saw cut or straight crack flaw types. Thus, the focus of this chapter is to discover the best practice in stress analyses of composite laminates with saw cut flaw damages.

4.1 Finite Element Method Scope

Throughout this analytical study, open hole case served as the control case while more emphasis was put on saw cut test cases. The primary objectives of the analytical study were to perform the following:

1. Discover the FEM best practices for precise prediction of fracture strengths in associated test cases
2. Evaluate the residual strength prediction accuracy via the use of WN fracture model
3. Assess mesh size sensitivities around flaw region
4. Evaluate several options to model narrow slit or crack flaws in FEM
5. Perform comparative evaluations of different failure theories used
6. Explore the use of micromechanics or multi-scale modelling as a source of material card generation
7. Correlate FEM predicted failure strengths to reported experimental failure strengths.

For this study, all test articles were modelled as a plane stress problem since the ratio of thickness to the width or length dimension is significantly small. Part modelling, material card

input, meshing and boundary condition assignments that are part of pre-processing tasks were performed in MSC Patran [20]. Similarly, post-processing tasks were also performed using MSC Patran where primarily stress or strain fringe plots and reports were created. MSC Nastran solver [21] was opted as the solver for the analyses. Details on MSC Patran/Nastran terms used within this thesis can be found in the Patran and Nastran reference manuals [22].

The analysis was mainly run for a linear static solution (SOL 101). The fracture mechanics model employed for analytical studies was the Whitney-Nuismer (WN) model with the Point Stress criterion [11]. The Point Stress criterion was selected due to its simplicity to be applied in the FEM. The peak stress tangential to flaw or crack tip was used to predict the residual strength of laminated composite articles. Subsequent sub-sections describe in detail the methods that were used to predict the residual strength of laminated composite articles.

4.1.1 Geometry

The test article was modelled as a planar surface broken into a number of sub-surfaces, primarily for the ease of subsequent meshing process. A higher number of sub-surfaces were concentrated around the flaw geometry so that finer mesh sizes could be used around the flaw details.

4.1.2 Material Properties

The plain weave fabric prepreg per Table 3-2 was classified as a two dimensional homogeneous orthotropic material with one plane of material symmetry (MAT8), sufficient for a plane stress analysis. Linear elastic properties used were derived from material lamina allowables using the reduced sampling method per guidance documented in Composite Materials Handbook [23]. In the case of when lamina or laminate failure theory was chosen to further

enhance the laminated composite failure strength prediction, appropriate failure model data were populated with strength values derived from lamina and laminate allowables.

As for the laminated composite definition, the laminate was modelled as a shell element with the use of composite element (PCOMP) which carry the assumptions that:

1. Each lamina is in a state of plane stress
2. Bonding in between lamina (ply) is perfect. Thus, interlaminar failure is ignored.
3. Two dimensional plate theory is adopted.

4.1.3 Meshing

The shell element primarily consisted of CQUAD4 elements with a few CTRIA3 elements at tight radius locations. Elements were generated with the use of Isomesh option. In general, three varying mesh sizes were used throughout the shell element with the size increases when the distance from the flaw details increases.

All shared grid points or nodes were made equivalent except for the case of intentional grid point disconnect to represent a flaw that is further described in Section 4.2.1. Element quality was also checked against aspect ratio, warp, skew and taper requirements.

4.1.4 Loads and Boundary Conditions

To simulate uniaxial tension testing, two displacement boundary conditions were enforced on end edge elements at top and bottom edges. Translational and rotational degrees of freedom were constrained to zero for bottom edge elements to simulate the fixed end of the test article. The top edge elements were enforced with an arbitrary forced displacement boundary condition to simulate quasi-static tensile force application on the test article.

4.1.5 Analysis Setting

A linear static (SOL101) analysis was run for each test ID. It must be noted that strain and stress outputs were extracted at the centroid of each element. Furthermore, the fiber strain outputs were requested so that a correlation to strain gage and ARAMIS readings could be performed at outermost plies. As expected, the highest stress or strain response occurred at elements next to the flaw tip on both sides. This is illustrated in Figure 4-1.

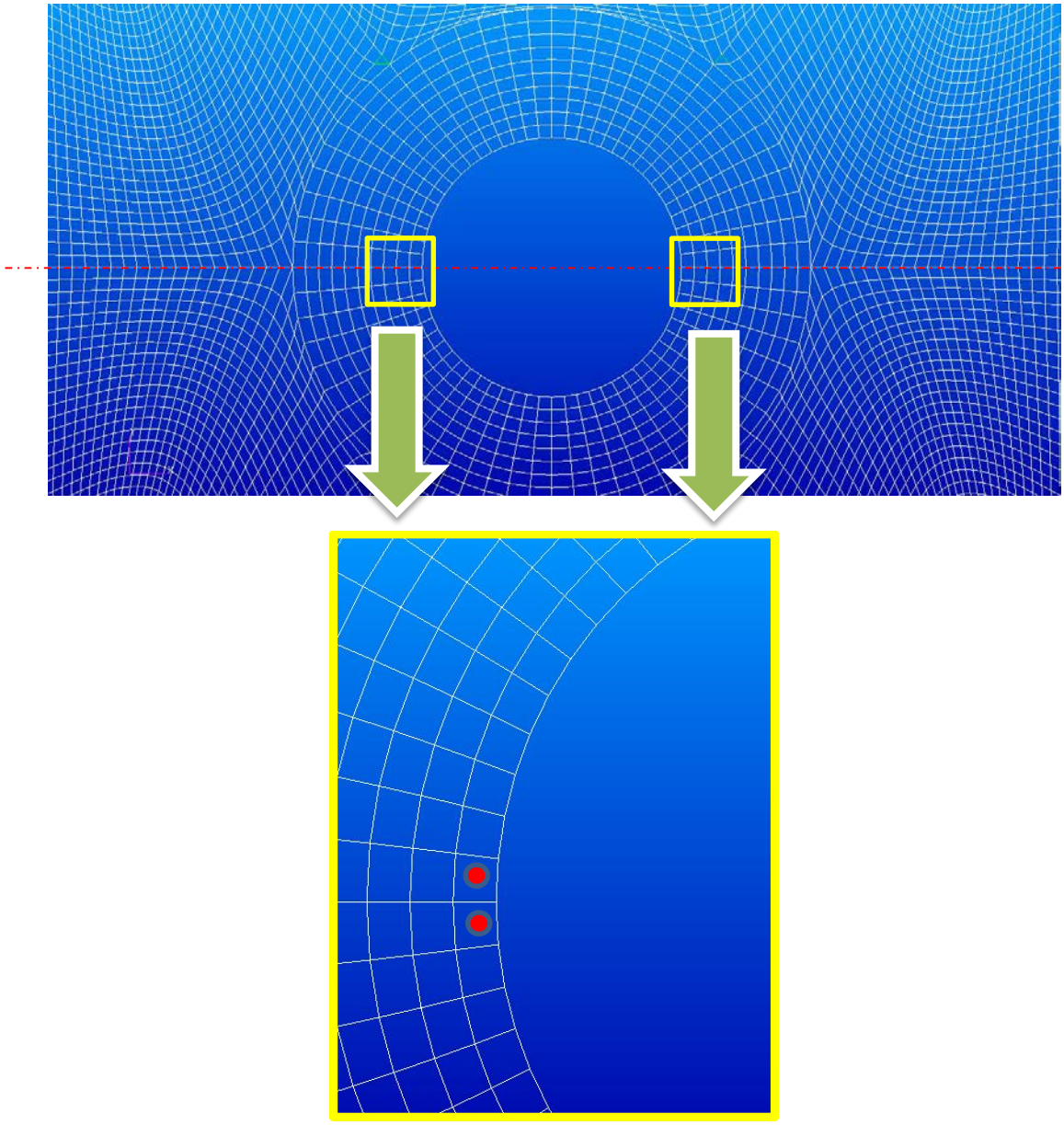

Figure 4-1 Centroids of elements near to flaw details

4.2 Analysis Variables

Several analysis variables were studied to evaluate the influence of each parameter on the failure prediction capability and to find the optimal analysis methods to evaluate residual strength of laminated composites especially for saw cut flaws. Table 4-1 describes the extent and types of variables studied along with the baseline settings used across the analyses of saw cut flaw. Details of each FEM variable are described in the sub-sections.

TABLE 4-1

ANALYSIS VARIABLES STUDIED

<table>
<tr><th></th><th>Flaw Type</th><th>Mesh Size Around Flaw Details (inch)</th><th>Flaw Representation</th><th>Laminated Composite Failure Theory</th><th>Material Card Source</th></tr>
<tr><td>Control Case Setting</td><td>Circular Hole</td><td>0.050
0.100</td><td>Geometry</td><td>Laminate-based Failure</td><td>Experimental</td></tr>
<tr><td>Baseline Setting</td><td rowspan="3">Saw Cut</td><td>0.040 to 0.050</td><td>Grid Point Disconnect</td><td>Laminate-based Failure</td><td>Experimental</td></tr>
<tr><td rowspan="2">Other Setting</td><td>0.015 to 0.030</td><td>Geometry-Ideal</td><td rowspan="2">Lamina-based Failure</td><td rowspan="2">Micromechanics</td></tr>
<tr><td>0.100</td><td>Geometry-Actual</td></tr>
</table>

4.2.1 Mesh Sensitivity

Mesh sensitivity studies were performed to find the reasonable mesh size to be used around the flaw details. Various arbitrary mesh sizes were used in analyses, and the predicted test article failure loads were compared against the experimental failure loads from Chapter 3. Analytical results were then curve-fitted to find the optimum mesh size to be used to predict failure load response when compared to the experimental data.

4.2.2 Flaw Representation

There are several ways of representing narrow slit flaws in the FEM from as simple as grid point disconnect and all the way to actual geometry modelling of the flaw.

Grid Point Disconnect

Using this method, saw cut damage was represented via the grid point (node) disconnect. This method idealized fine saw cut damage without having to emphasize much on the actual geometry of the saw cut damage. This was achieved by excluding grid points along the flaw length during the grid point equivalence process. For verification, two grid points can be seen along the flaw length as shown in Figure 4-2.

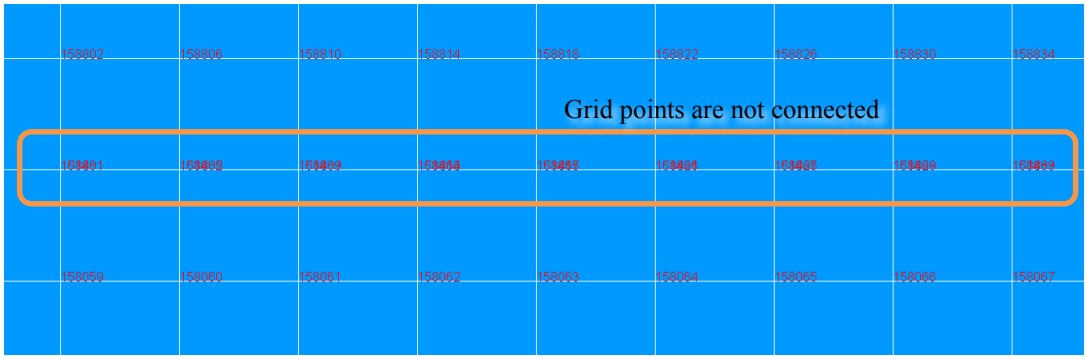

Figure 4-2 Grid point disconnect representation of flaw

Geometry-Ideal

Using this method, saw cut damage was represented by its simplified and ideal geometry, which is in the form of a rectangle. The only different feature from this representation to the actual flaw geometry is the shape of flaw ends. The actual flaw height of 0.070" was modelled. An example of the flaw representation at a flaw detail location is shown in Figure 4-3.

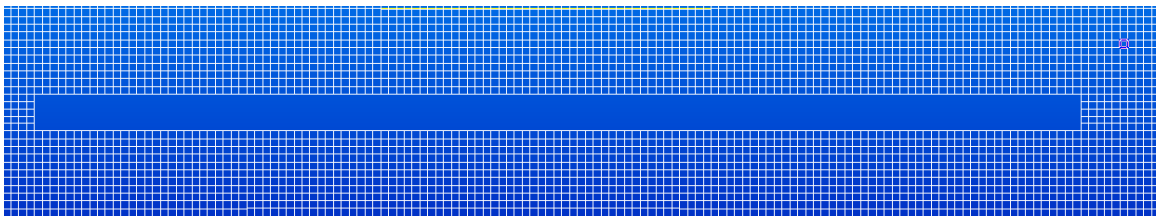

Figure 4-3 Ideal geometry representation of flaw

Geometry-Actual

Similar to the previous method, this method represents saw cut damage with the emphasis on the actual semi-circular shape of flaw ends. The actual flaw height as tested was also modelled. An example of the flaw representation at flaw detail location is shown in Figure 4-4.

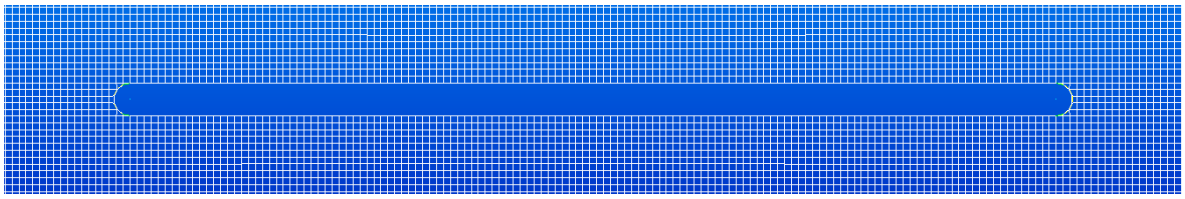

Figure 4-4 Actual geometry representation of flaw

4.2.3 Laminated Composite Failure Theory

In general, laminated composite failure theories can be categorized into these common material levels [23]:

1. Macroscale (laminate) level: A multi-layer composition of fixed oriented plies such as quasi-isotropic, 'hard' or 'soft' laminates.
2. Macroscale (lamina) level: A single layer of ply.
3. Mesoscale (constituent) level: Fiber (reinforcement) and resin (matrix).
4. Microscale level: Each point within fiber and resin.

Within this thesis, the two most commonly used laminated composite failure theory levels, which are laminate-based and lamina-based levels, were exercised. To describe the difference between the two levels of failure theories, it would make more sense to start from the lamina-based failure theories and then progress to the laminate-based failure theories.

Lamina-based Failure Theories

Lamina-based failure theories can be further classified into three common types per [25]:

1. Limit theories, in which the failure is predicted from the corresponding strengths or strain limits. Examples of such theories are the Maximum Stress and Maximum Strain failure theories.
2. Interactive theories, in which stresses in all directions are contained within one expression. Examples of commonly adopted interactive failure theories are the Tsai-Wu and Tsai-Hill theories.
3. Partially interactive or failure mode based theories, where separate failure criteria are assigned for fiber and interfiber (matrix or fiber-matrix interface) failures. Examples of such theories are the Puck and Hashin-Rotem theories.

For the purpose of this study, one limit-based failure theory (Maximum Stress) and one interactive failure theory (Tsai-Wu) were used to predict residual strength of notched laminates. The input for failure theories were derived from lamina level testing and MSC Nastran was used to calculate failure indices. The resulting failure indices were then extracted from results (f06) file and evaluated to find the predicted failure load.

For Maximum Stress failure criteria [25], the failure is predicted in a lamina when the stress exceeds the specified limit in the particular loading direction. A lamina would fail if any of the criteria for plane stress problem is violated. It can be observed here that each stress component is evaluated independently without the coupling of other stress components.

$$\begin{aligned} -S_1 < \sigma_1 < S_1 \\ -S_2 < \sigma_2 < S_2 \\ -S_{12} < \tau < S_{12} \end{aligned} \tag{22}$$

On the other hand, for the Tsai-Wu interactive failure theory [26], the interaction between all stress components is taken into consideration. In the tensor notation, the Tsai-Wu failure can be represented as shown in Equation (23):

$$f_i\sigma_i + f_{ij}\sigma_i\sigma_j = 1 \tag{23}$$

For a two-dimensional state of stress, the above equation can be reduced into this form:

$$f_1\sigma_1 + f_2\sigma_2 + f_{11}\sigma_{11}^2 + f_{22}\sigma_{22}^2 + f_6\tau_{66}^2 + 2f_{12}\sigma_1\sigma_2 = 1 \tag{24}$$

All necessary second-order strength tensor (f_i) and fourth-order strength tensor (f_{ij}) values can be determined per Ref. [26]. Per Ref. [25], for carbon fiber reinforced composite laminates, it has been shown that the interactive strength tensor (f_{12}) can be reasonably approximated from Equation (25).

$$f_{12} \cong -\frac{1}{2}\sqrt{f_{11}f_{22}} \tag{25}$$

Laminate-based Failure Theories

Common laminate-based theories available at this time are mostly designed to validate and correlate lamina failure prediction theories for first ply failure (FPF) prediction and for the ultimate laminate failure (ULF) prediction with experimental data. The two most recognized laminate based failure theory validation efforts were performed by C.T. Sun [27] and the "Worldwide Failure Exercise" by Hinson et al. [28].

Based on the ULF prediction, an empirical approach was adopted for the purpose of this study. The empirical-based approach provides maximum strain cut-off values in varying Angled Minus Longitudinal (AML) laminates depending on the loading mode and the environment. These maximum strain cut-off values were again derived from extensive building block level testing. Specifically for this study, for the notched failure prediction in each test case, maximum

strain cut-off values of unnotched tension at the applicable test condition were used depending on the AML of the laminate.

4.2.4 Material Card

Two approaches were adopted to define material elastic properties to be entered in the FEM material card. One way was primarily via a full experimental approach where properties were derived from building block level testing. The other was via the use of micromechanics approximation or multi-scale modelling. While the experimental approach has been a generally accepted material characterization approach, this approach has its own disadvantages and limitations, such as high variability due to inherent material, processing and testing scatters, size or scaling effects [29], and real-life challenges in performing the required tests. On the other hand, the micromechanics approach is a relatively new material characterization or prediction approach that has been making its way into higher levels of material characterization, namely at laminate and element levels. One great advantage of the use of micromechanics software is the ability to predict material response with minimal testing and to predict failure progression, which in return provides greater understanding and better ability in general micro-level and macro-level failure predictions of composites. Thus, the inclusion of micromechanics modelling technique within this study is to provide comparative evaluation of the technique in comparison to the traditional purely empirical approach.

Micromechanics

The two most commonly adapted micromechanics idealization models are based on Mori-Tanaka [30] and Double Inclusion (Nemat-Naser and Hori) [31]. Two softwares were employed to predict the lamina elastic properties which were:

1. MSC Digimat MF module [32]

2. Autodesk Composite Simulation Design (ASCD) or previously known as Firehole Composites Helius [33]

The Digimat module gives users a lot of flexibility in selecting the preferred micromechanics idealization method and in customizing the micromechanics Representative Volume Element (RVE) model depending on suitability and material model prediction accuracy need. For ASCD software, the micromechanics idealization method is standardized and cannot be further customized. Furthermore, the micromechanics idealization method used in ASCD could not be determined and is proprietary at the time of writing.

For carbon fiber, an elastic constitutive law was used and the fiber was assumed to be transversely isotropic with the plane 2-3 as the plane of symmetry. For matrix, the elastic constitute law was selected and due to the nature of epoxy matrix, the isotropic material model was chosen. For micromechanics analyses, the lamina property prediction was initiated from the micro-scale level with the known properties at inclusion and matrix level as reported in Section 3.2.2 and Section 3.2.3 respectively. For carbon fiber, a lot of elastic properties were not known due to the experimental challenges of fiber characterization, especially in the transverse direction. Due to the unavailability of these properties, they were estimated based on reported legacy material properties recorded in Ref. [25] and manually iterated until satisfactory lamina properties were achieved. For simplicity, a material property estimation exercise was performed first at unidirectional (UD) prepreg level. Once an acceptable property estimation was made at the UD level, plain weave (PW) prepreg material estimation was run using the previously best found fiber and matrix properties or initiated again from scratch. Table 4-2 and Table 4-3 illustrate the iteration process for phase property prediction for Digimat. Table 4-4 shows the predicted phase properties for ASCD for both UD and PW prepreg forms.

TABLE 4-2

ESTIMATED PHASE MATERIAL PROPERTIES FOR UNIDIRECTIONAL (DIGIMAT)

	Unidirectional Prepreg			Literature Guidance Ref. [25]
	Properties	Initial Estimate	Final Estimate	Reported Value (Product Name)
Inclusion (Carbon Fiber) Properties	Fiber Transverse Modulus, E_{22_f}	2.2 Msi	2.5 Msi	2.2 Msi (T-300)
	Fiber Transverse Shear Modulus, G_{23_f}	1 Msi	0.8 Msi	1 Msi (T-300)
	Fiber Poisson's Ratio, ν_{12_f}	0.2	0.13	0.2 (T-300)
	Fiber Poisson's Ratio, ν_{23_f}	0.2	0.32	N/A

TABLE 4-3

ESTIMATED PHASE MATERIAL PROPERTIES FOR PLAIN WEAVE (DIGIMAT)

	Plain Weave Prepreg			Literature Guidance Ref. [25]
	Properties	Initial Estimate	Final Estimate	Reported Value (Product Name)
Inclusion (Carbon Fiber) Properties	Fiber Transverse Modulus, E_{22_f}	2.5 Msi	2.2 Msi	2.2 Msi (T-300)
	Fiber Transverse Shear Modulus, G_{23_f}	0.8 Msi	4 Msi	1 Msi (T-300)
	Fiber Poisson's Ratio, ν_{12_f}	0.13	0.2	0.2 (T-300)
	Fiber Poisson's Ratio, ν_{23_f}	0.32	0.2	N/A

TABLE 4-4

ESTIMATED PHASE MATERIAL PROPERTIES FOR UNIDIRECTIONAL AND PLAIN WEAVE (ASCD)

	Unidirectional and Plain Weave Prepreg			Literature Guidance Ref. [25]
	Properties	Initial Estimate	Final Estimate	Reported Value (Product Name)
Inclusion (Carbon Fiber) Properties	Fiber Transverse Modulus, E_{22_f}	2.2 Msi	2.4 Msi	2.2 Msi (T-300)
	Fiber In-Plane Shear Modulus, G_{12_f}	4 Msi	6 Msi	4 Msi (T-300)
	Fiber Transverse Shear Modulus, G_{23_f}	1 Msi	700 ksi	1 Msi (T-300)
	Fiber Poisson's Ratio, ν_{12_f}	0.2	0.28	0.2 (T-300)
	Fiber Poisson's Ratio, ν_{23_f}	0.2	0.24	N/A
	Fiber Longitudinal Compression Strength, $-S_{1_f}$	350 ksi	430 ksi	N/A
Matrix (Epoxy) Properties	Matrix Transverse Modulus, E_{22_m}	604 ksi	604 ksi	620 ksi (3501-6)
	Matrix In-Plane Shear Modulus, G_{12_m}	215 ksi	225 ksi	240 ksi (3501-6)
	Matrix Tensile Strength, $+S_{1_m}$	20.9 ksi	10.1 ksi	10 ksi (3501-6)
	Matrix Compression Strength, $-S_{1_m}$	45 ksi	42 ksi	30 ksi (3501-6)
	Matrix In-Plane Shear Strength, S_{12_m}	22.5 ksi	25.5 ksi	15 ksi (3501-6)

For the lamina property estimation using Digimat, the Double Inclusion method was chosen over the Mori-Tanaka approach, as it seemed to produce a better property prediction. For PW prepreg form, using Digimat, the RVE definition was further enhanced with the use of the 'Advanced Yarn' module where the yarn and fabric properties were as shown in Table 4-5 and Figure 4-5. Generally, a yarn height to width geometry ratio of 0.1 is reasonable for plain weave fabric [34]. However, from this exercise, the yarn height to width geometry ratio of 0.052 was found to produce the best predicted lamina properties. On the other hand, using the ASCD software, PW prereg properties were predicted using the 'Fabric Builder' module where fabric properties are as shown in Table 4-6.

TABLE 4-5

ESTIMATED YARN AND FABRIC PROPERTIES (DIGIMAT)

	Plain Weave Yarn and Fabric Properties
Properties	Digimat
Yarn	
Filament Count	3000
Fiber Diameter (mm)	0.0068
Yarn Height (mm)	0.104
Yarn Width (mm)	2
Woven Fabric	
Woven Fabric Orientation	0/90
Warp Yarn Count (yarns/cm)	5
Weft Yarn Count (yarns/cm)	5
Areal Weight (gsm)	185.55
Inter-Yarn Porosity (%)	0.21
Fiber Volume (%)	52.47

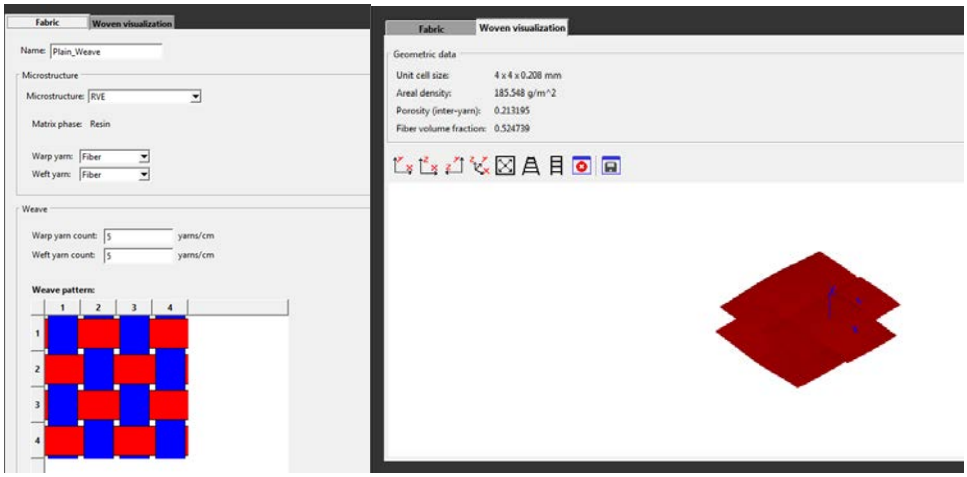

Figure 4-5 Advanced yarn module output (Digimat)

TABLE 4-6

ESTIMATED FABRIC PROPERTIES (ASCD)

	Plain Weave Fabric Properties
Properties	ASCD
Woven Fabric	
Fiber Volume in Warp (%)	50
Fiber Volume in Weft (%)	50
Areal Weight (gsm)	200
Fiber Weight (%)	50
Void Volume (%)	0
Fabric Thickness (in)	0.0082

From numerous manual iterations of the lamina property prediction exercises, the results of lamina property for each prepreg form when compared to experimental data are shown in Table 4-7. While Digimat only offered engineering constants output, ASCD could also predict the lamina strengths in different loading directions and mode. Because of the proprietary nature of lamina allowables, the experimental lamina properties cannot be published for absolute value comparisons.

TABLE 4-7

MICROMECHANIC PROPERTY PREDICTIONS DIFFERENCE TO EXPERIMENTAL DATA

	Unidirectional Prepreg Lamina Properties		Plain Weave Prepreg Lamina Properties	
Comparison to Experimental Data	Digimat Difference (%)	ASCD Difference (%)	Digimat Difference (%)	ASCD Difference (%)
Fiber Volume	0	0	-5.71	0.07
Longitudinal Modulus, E_{11}	5.21	7.54	0.39	12.42
Transverse Modulus, E_{22}	12.99	0.21	-0.67	11.24
Interlaminar Modulus, E_{33}	N/A	8.76	-11.56	7.87
In-plane Shear Modulus, G_{12}	-30.30	-3.71	-8.95	-13.92
Transverse Shear Modulus, G_{13}	-24.03	4.97	18.55	5.42
Transverse Shear Modulus, G_{23}	16.34	-0.65	12.35	-0.09
Poisson's Ratio, ν_{12}	32.60	4.46	-12.30	-28.42
Poisson's Ratio, ν_{13}	17.74	-7.24	-4.45	-6.12
Poisson's Ratio, ν_{23}	-21.17	6.33	-3.71	-5.39
Density, ρ	-1.91	-1.91	-3.49	-2.73
Longitudinal Tensile Strength, $+S_1$	N/A	-1.67	N/A	11.99
Transverse Tensile Strength, $+S_2$	N/A	-0.18	N/A	14.57
Longitudinal Compression Strength, $-S_1$	N/A	5.80	N/A	14.21
Transverse Compression Strength, $-S_2$	N/A	-3.83	N/A	20.91
In-plane Shear Strength, S_{12}	N/A	-2.18	N/A	-4.66

It can be observed that in the case of Digimat simulation, surprisingly, a greater challenge was faced in calibrating the micromechanics model for UD prepreg form, especially for shear modulus and Poisson's ratio properties. The micromechanics simulation for the Digimat PW form was found to be acceptable, with all predicted properties except for transverse shear modulus, G_{13}, are within ±15% from the experimental data. From the ASCD simulations, the UD predicted lamina properties were very exceptional, with all predicted properties falling within ±10% from the reported experimental lamina data. For the PW form, in general, all properties seemed to fall within ±15% except most noticeably Poisson's ratio, ν_{12}.

Some of these differences are attributed to the fact that micromechanics modelling assumed that the material was a perfect transverse orthotropic with the plane 2-3 as the plane of symmetry. From experimental evaluations, however, it is known that properties in the 1-2 material plane is not always similar to those in the 1-3 material plane, potentially due to inherent experimental approach scatters previously discussed. Because of the balanced one 'up' and one 'down' yarn weave style, the micromechanics modelling approach also assumed that properties in warp direction of the yarn were similar to the ones in weft direction of the yarn. In reality, because of less weaving tension in the weft yarn compared to the warp yarn during the weaving process, the properties in the transverse direction tend to be lower than those of in the longitudinal direction. In terms of loading direction, similarly, modulus properties in tension and compression in micromechanics idealization are assumed to have a similar value. Meanwhile, in a practical material characterization experimental exercise, it is well known that the modulus in compression tends to be different than that in tension.

4.3 Summary of Analytical Results

To obtain predicted test article failure load for each test ID, the following procedures were followed:

1. One end was constrained as the fixed end. The other end was applied with an arbitrary enforced displacement.
2. Max resultant strain due to an arbitrary enforced displacement was extracted from results (.f06) file. Constraint forces or reaction forces at the fixed end grid points were extracted and added.
3. Predicted failure load was calculated using Equation (26). The equation is valid because of the linear elastic analysis performed.

$$P_{fail} = \frac{\varepsilon_{UNT}}{\varepsilon_{arbitrary}} P_{fixed\ end} \quad (26)$$

4.3.1 Mesh Sensitivity

With the use of varying arbitrary mesh sizes around the flaw details, FEM predicted failure loads were then calculated per the procedures previously described. All the predicted load points were then curve-fitted to observe the effects of mesh sensitivity towards failure load prediction. As illustrated in Figure 4-6, finer mesh sizes around the flaw details result in higher maximum strains, thus consequently predicting lower failure loads. All the obtained test data were then inserted into the plot to see how well the derived mesh sensitivity curve-fit functions compare to the test data. From this exercise, it can be observed that the curve-fit functions correlate well with the experimental data. It also shows that the optimum mesh size to be used for failure prediction for all saw cut test cases is found to be in the region of 0.040 to 0.070 inch mesh sizes.

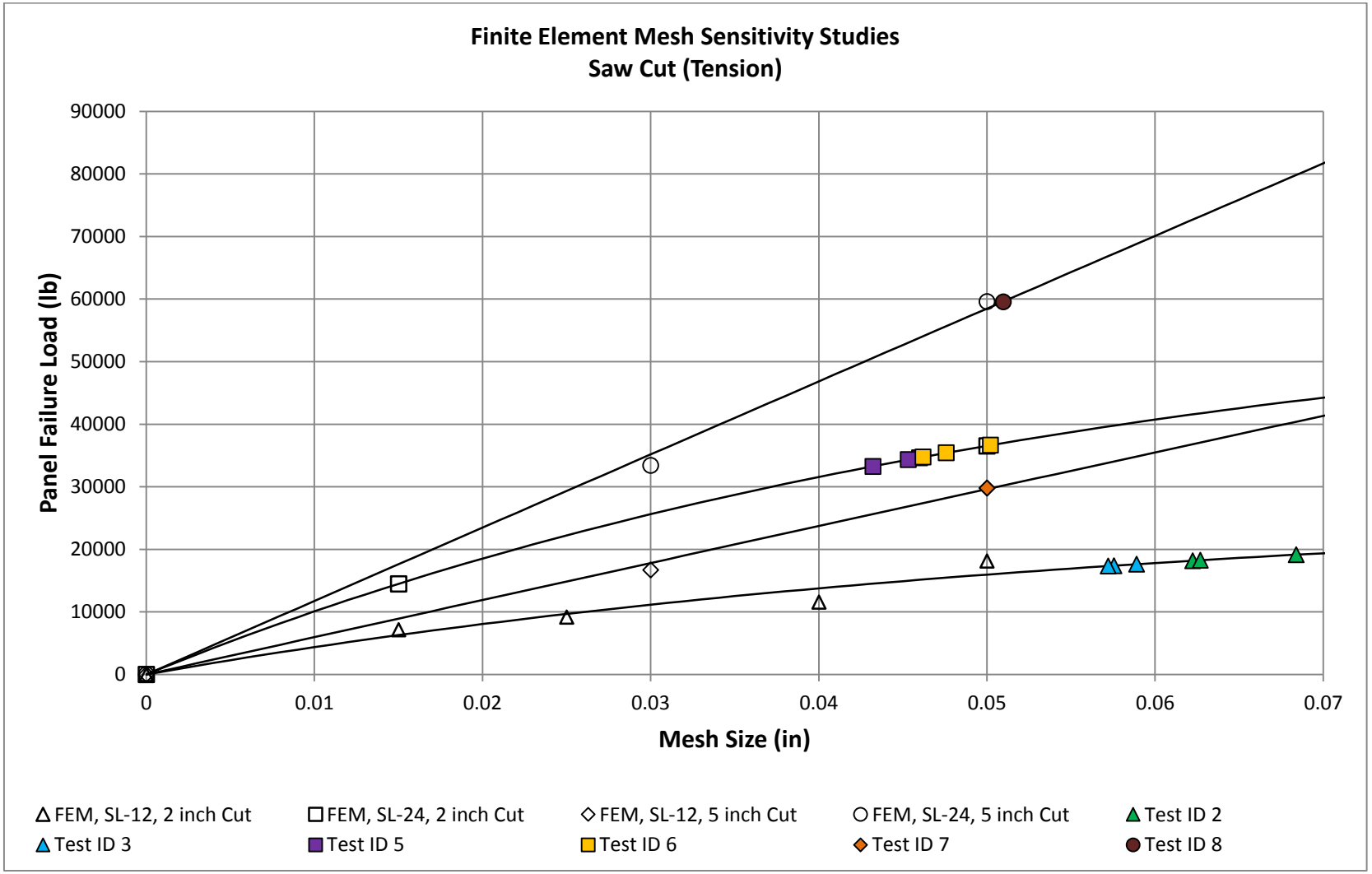

Figure 4-6 Finite element mesh sensitivity studies for saw cut (tension)

4.3.2 Evaluation of Control Case

For circular hole analysis, the analysis variables were set to the control case settings per Table 4-1. Two mesh sizes of 0.050" and 0.1" were used around the open hole geometry and the predicted failure loads are reported in Table 4-8. It can be observed that mesh size variation seems to have relatively little effects on the predicted failure loads.

TABLE 4-8

CONTROL CASE EVALUATION

Test ID	Type	Flaw Length	Mesh Size	Predicted Failure (kip)	Average Actual Failure Load (kip)
1	Open Hole	2	0.050	24.900	26.177
			0.100	26.583	

4.3.3 Flaw Representation

For saw cut flaw type, three saw cut flaw representation techniques as previously described in Section 4.2.1 were evaluated using a fixed mesh size of 0.050". The predicted failure loads are shown in Table 4-9. It must be noted that flaw representation via geometry technique, either ideal or actual, tends to produce more conservative predictions.

TABLE 4-9

FLAW REPRESENTATION EVALUATION

Test ID	Type	Flaw Representation	Mesh Size (in)	Predicted Failure (kip)	Average Actual Failure Load (kip)
2,3	Saw Cut	Disconnected Grid Points	0.050	18.151	18.529
		Geometry (Ideal)		13.848	
		Geometry (Actual)		11.013	

4.3.4 Laminated Composite Failure Theory

Two approaches for failure theories from mechanics of laminated composites were evaluated as previously described in Section 4.2.3. Predicted failure loads from each evaluated failure theory type are presented in Table 4-10.

TABLE 4-10

FAILURE THEORY EVALUATION

Test ID	Type	Micromechanics Approach	Mesh Size (in)	Predicted Failure (kip)	Average Actual Failure Load (kip)
2,3	Saw Cut	Laminate: AML	0.050	18.151	18.529
		Lamina: Max Stress		18.616	
		Lamina: Tsai-Wu		17.666	

The predicted failure load from the use of Maximum Stress lamina failure theory was first expected to be lower due to the fact that the lamina failure theory would have indicated a first ply failure in comparison to the AML laminate failure theory which would indicate the ultimate laminate failure. A further look into the resultant failure indices of Maximum Stress theory indicates that the failed plies were 0°/90° plies. Since the lamina longitudinal tensile strength, S_1 was derived from tensile coupon with only 0° plies, thus the tensile strength is intuitively higher than that of a balanced and symmetric laminate. Because of this, a higher strength limit was used in the Maximum Stress theory thus causing the predicted failure to be higher than the predicted failure load from the AML laminate-based failure theory.

Also, it must be noted that since the AML laminate failure theory and the Maximum Stress lamina failure theory are mainly made of linear functions and non-interactive terms, the failure load prediction is rather a straightforward exercise, as outlined in the beginning of Section 4.3. A similar approach however cannot be applied to the Tsai-Wu failure criterion due to the

fact that the failure index equation is not a linear function but rather a quadratic function and dependent upon all stress components. Because of this, a failure load prediction can only be approximated once the trend of the failure index function against a varied FEM parameter is well understood. To illustrate this point, FEM analyses were performed with multiple arbitrary enforced displacement values and the maximum calculated failure indices from all the plies were evaluated. The interaction of the enforced displacement with the Tsai-Wu failure index is shown in Figure 4-7. Because of the form of the Tsai-Wu failure index equation, Equation (24), similarly these data were then curve-fitted to a quadratic function. Since it is known that the first ply failure within the laminate occurs when the failure index equals one, the appropriate enforced displacement was found to be 0.0725". The FEM analysis was then performed and the predicted failure load was found to be 17.666kip. Because of the interactive nature of the failure theory, the Tsai-Wu produces the most conservative prediction of the failure load.

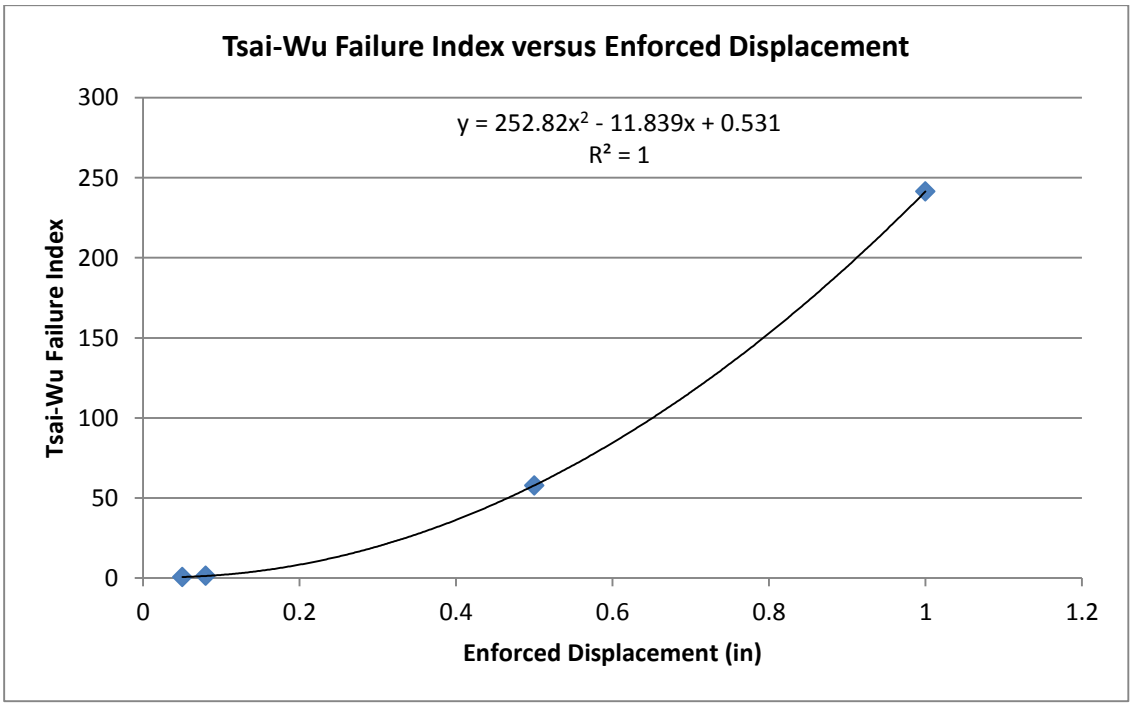

Figure 4-7 Enforced displacement interaction with Tsai-Wu failure index

4.3.5 Material Card

Two sources of micromechanics modelling approaches were evaluated, and the predicted failure loads are reported in Table 4-11.

TABLE 4-11

MICROMECHANICS APPROACH EVALUATION

Test ID	Type	Micromechanics Approach	Mesh Size (in)	Predicted Failure (kip)	Average Actual Failure Load (kip)
2,3	Saw Cut	Digimat	0.050	17.989	18.529
		ASCD		19.959	

A lower failure prediction from the Digimat run is expected due to the lower predicted lamina properties in primary variables such as E_{11}, E_{22} and G_{12} in Table 4-7 when compared to those of experimental data and ASCD predictions. Over-prediction from the ASCD run is, on the other hand, due to the over-prediction of lamina properties in Table 4-7.

4.4 Analytical Method Recommendation

Table 4-12 summarizes the analytical recommended parameters to be used to evaluate residual strength around flaw details. Most importantly, as stated earlier, the use of appropriate mesh size in high stress concentration and intensity regions has great effects in the analysis results. From this study, it is concluded that a mesh size of 0.060” and 0.050” is appropriate for open hole and saw cut flaw types respectively for the purpose of failure prediction. However, for a more conservative analysis, it is to the advantage of stress analysts to choose a lower mesh size than that proposed in Table 4-12. It must also be cautioned, however, that these suggested mesh sizes would no longer be appropriate for small radius holes or small saw cut sizes, outside of the range studied here, i.e., less than two inches in size, since the results of the FEM analyses may no longer be conservative and accurate.

TABLE 4-12

ANALYSIS RECOMMENDED SETUPS

Flaw Type	Mesh Size Around Flaw Details (inch)	Flaw Representation	Laminated Composite Failure Theory	Material Card Source
Circular Hole	0.060	Geometry	Laminate-based Failure	Experimental
Saw Cut	0.050	Grid Point Disconnect	Laminate-based Failure	Experimental

While various flaw representation techniques can be adopted for FEM analyses, it is strongly felt that the flaw representation via grid point disconnect is the most convenient way for stress analysts without having to focus much on the details of physical flaw geometry or damage threats. For the selection of failure theories, the appropriate selection would be upon the FEM exercise objectives. With the use of lamina failure theories, it would generally under predict the residual strength of a notched laminate due to the fact that the theories are primarily associated with the first ply failure. Thus, for more precise prediction, the use of laminate-based failure theory such as the AML failure theory which is based on the ULF prediction would be more desirable.

It must be noted that the use of micromechanics modelling technique shows reasonable prediction results considering numerous approximations and estimations were made at inclusion and matrix levels. More iterations along with major calibration efforts at lamina and laminate using simple unnotched and notched coupons have to be initiated to further improve the prediction accuracy of the micromechanics material models. Thus, for the time being, the use of the experimental based material card is recommended.

CHAPTER 5

DISCUSSION OF RESULTS

5.1 Experimental and Analytical Studies Correlation

This chapter focuses on correlations between experimental and analytical studies. Several items of interest are compared between these two studies:

1. Failure loads and ultimate strengths.
2. Near flaw and far-field strain readings.
3. Strain and stress distributions near the flaw across the horizontal axis.
4. General global strain fringe plots.

FEM output extraction was made from elements from the mid-height of the flaw across the test article width as highlighted in Figure 5-1. For comparison purposes, only the y-component of stress and strain outputs were used since the y-direction was the primary loading direction. For comparison to strain gage readings, the FEM strain outputs were selected from a few representative elements at similar locations as of the strain gages on the test article. In addition, the FEM strain outputs were corrected through strain coordinate transformation to match the rosette strain gage orientation. Extra attention must be made to the strain gage orientation with respect to the fiber direction on the outermost ply of interest and the material rosette reference.

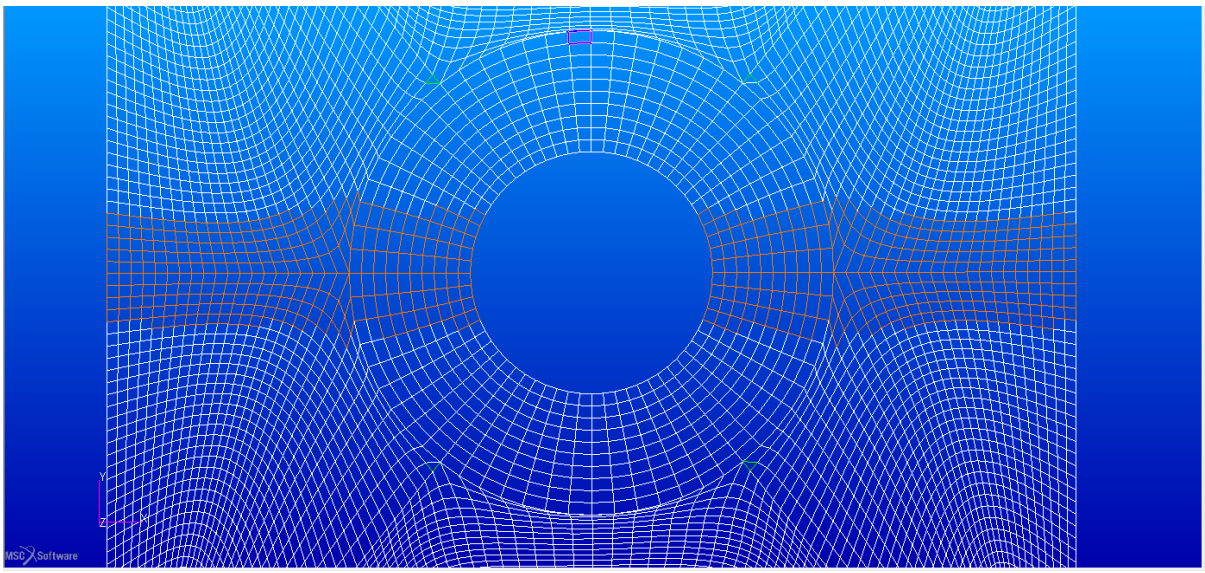

Figure 5-1 FEM output exctraction around flaw across article width

5.1.1 Open Hole Flaw

Test ID 1

Table 5-1 shows the comparison between the ARAMIS and FEM strain readings at the last available load point prior to the ultimate failure locally near flaw. The difference between the two sources seems to be very little. For a global view of the strain distribution near the flaw across the test article width, all three strain outputs for strain in y-direction, ε_y along the flaw centerline are shown in Figure 5-2. It must be noted that strain distribution across the three sources seems to match well across the article width. The ARAMIS strain outputs are somewhat distorted next to the flaw boundary due to the measurement system's inability to accurately monitor strain readings near to edges. The masked out area out of the ARAMIS capability is illustrated in Figure 5-3 where the areas of about 0.020" to 0.025" from the flaw edges and the article periphery are ignored. Adjustments were then made to the FEM where several elements away from the flaw details were not posted to match the ARAMIS strain area coverage.

TABLE 5-1

STRAIN COMPARISON AT ARAMIS LAST LOAD POINT (TEST ID 1)

{Test ID 1} Open Hole		At ARAMIS Last Load Point		
Room Temperature Ambient		Experimental [ARAMIS[1]]	Analytical [FEM]	Difference (%)
Epsilon y, Near Flaw Max Strain[2] [με]	Right to Flaw	8656	8560	-1.11
	Left to Flaw	8494	8562	0.80

Notes:
(1) ARAMIS readings were taken on LJ200-036-1-OH-2, at 25000lbs load (Stage 15)
(2) Near flaw strain readings were taken 0.25" away from the flaw tip/edge along flaw horizontal centerline

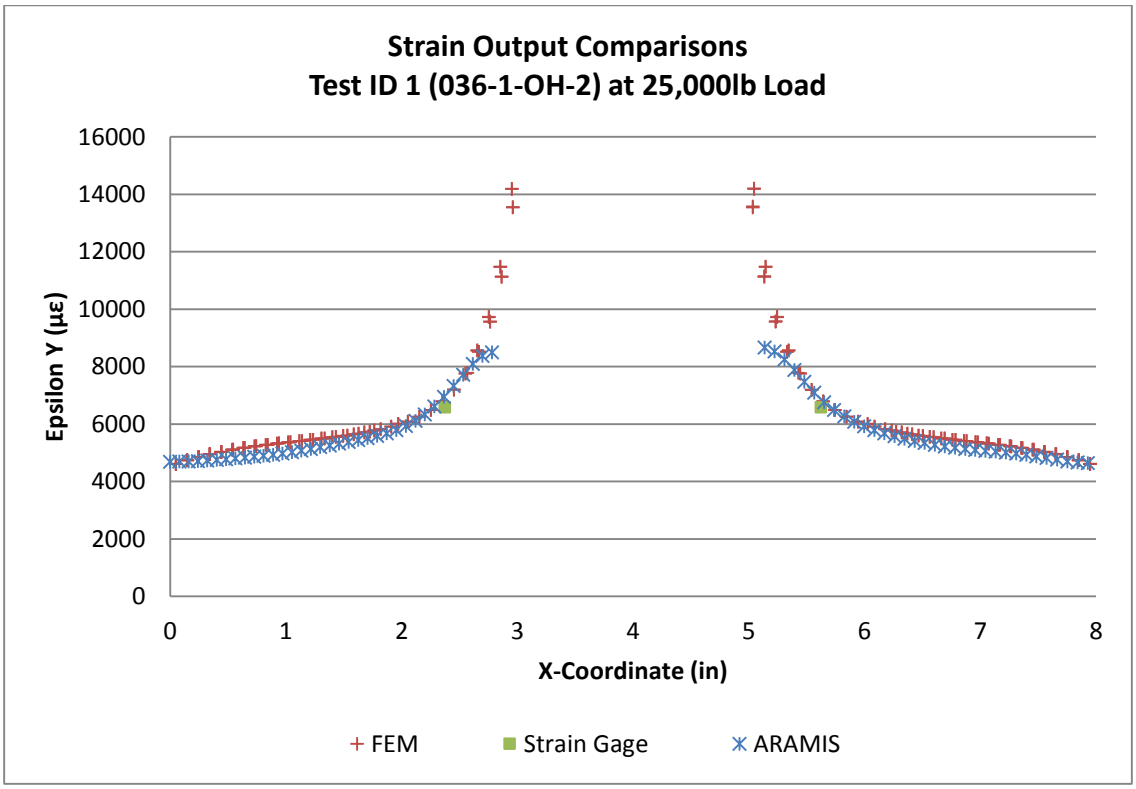

Figure 5-2 Epsilon y strain output comparisons (test ID 1)

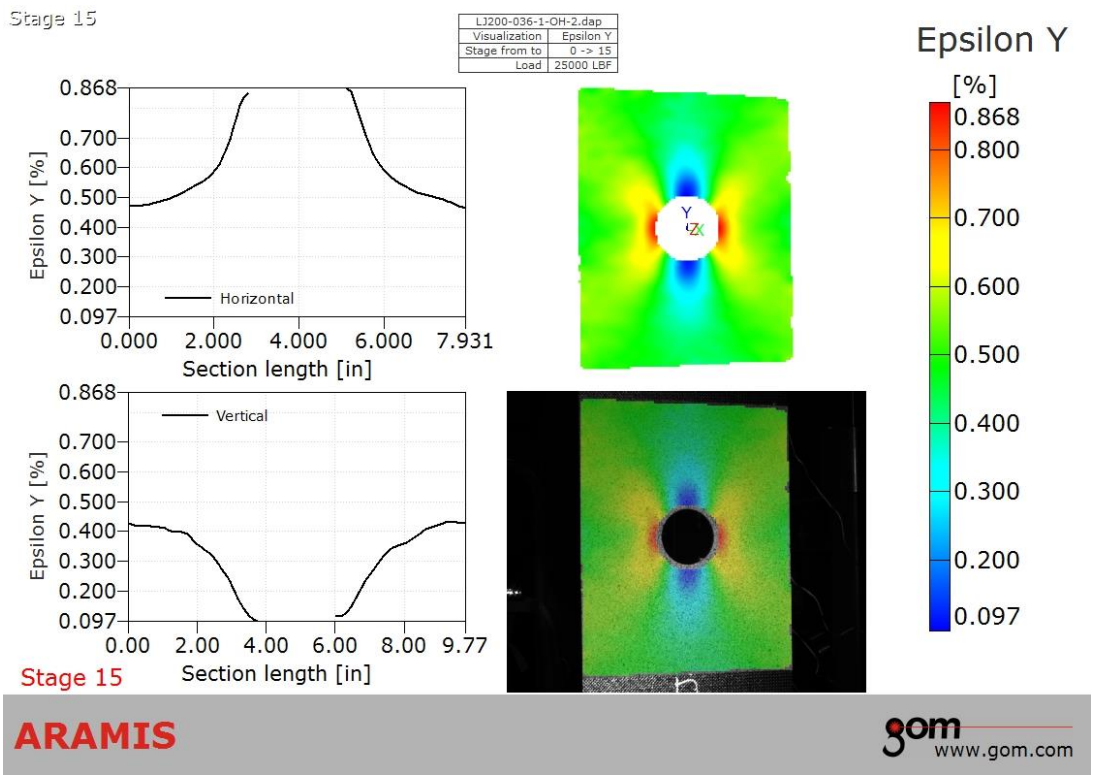

Figure 5-3 Epsilon y distribution from ARAMIS (test ID 1)

It must be noted that ARAMIS strain output was reported in percentage (%). Strain fringe plots of y-component of strain, ε_y from ARAMIS and FEM are shown in Figure 5-4 and Figure 5-5 respectively. For better comparison of maximum strain values between the two sources, the averaging option within FEM fringe plotting was not selected as shown in Figure 5-6. The difference in maximum strain between the two sources is about 1%.

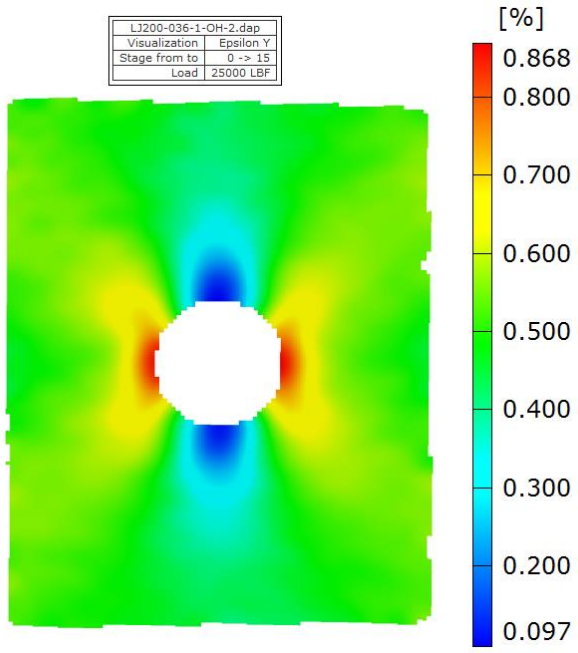

Figure 5-4 Epsilon y ARAMIS output (test ID 1)

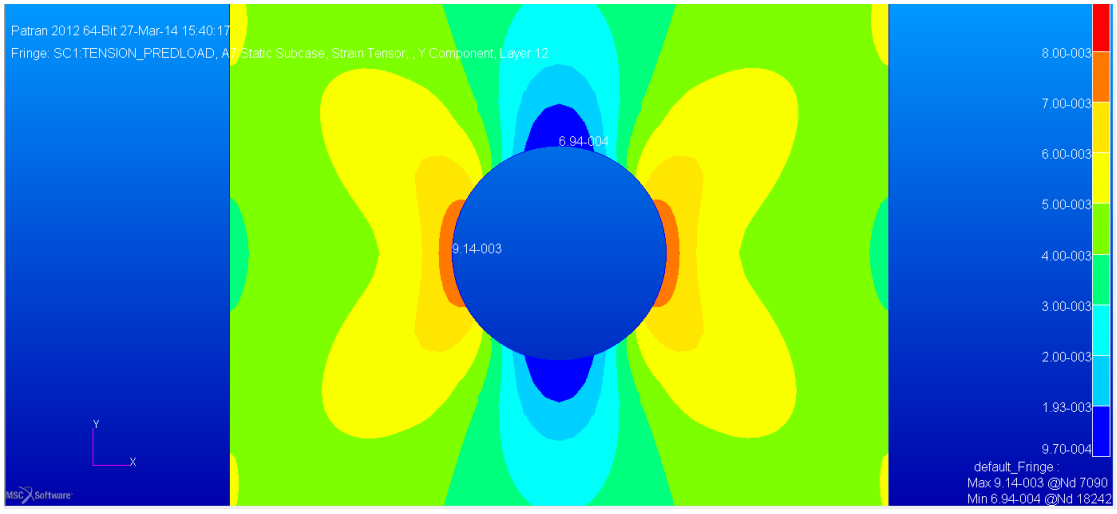

Figure 5-5 Epsilon y FEM output (test ID 1)

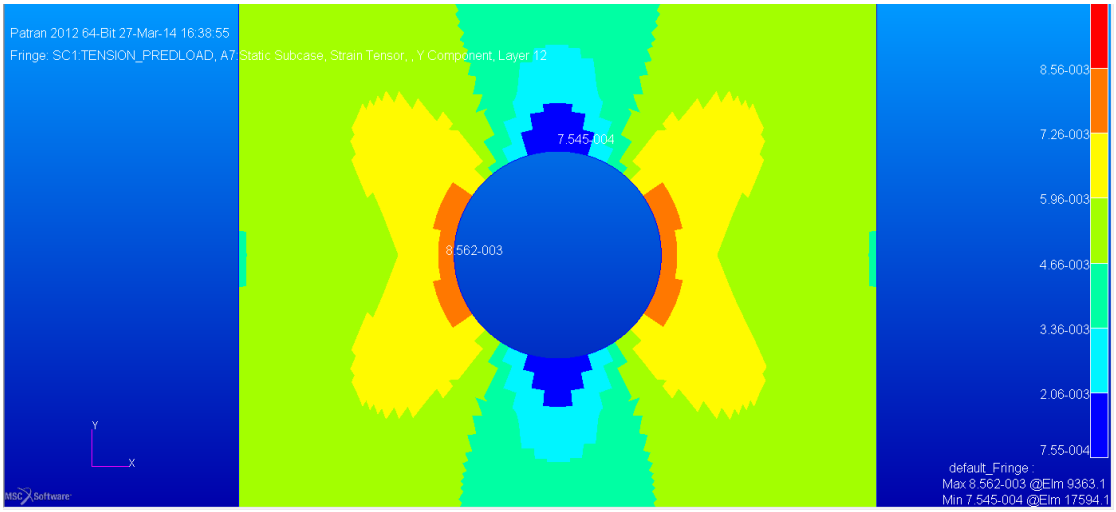

Figure 5-6 Epsilon y FEM output-no averaging (test ID 1)

Furthermore, stress outputs were used to compare the stress field distribution along the horizontal axis ahead of the flaw tip region. The stress distribution proposed by Konish and Whitney [12] for a circular hole as shown in Equation (10) was plotted and Figure 5-7 shows the comparison between the calculated stress function and outputs from FEM and ARAMIS. Strain outputs seem to match exceptionally well in comparison to the theoretical stress distribution except in a region of 0.25" away from the flaw edge where, as expected, the ARAMIS strain output accuracy deteriorates significantly. Meanwhile, Table 5-2 shows the comparison between strain gage and FEM strain readings at ultimate load. It can be observed that the difference between the two sources seems to be within ±10%.

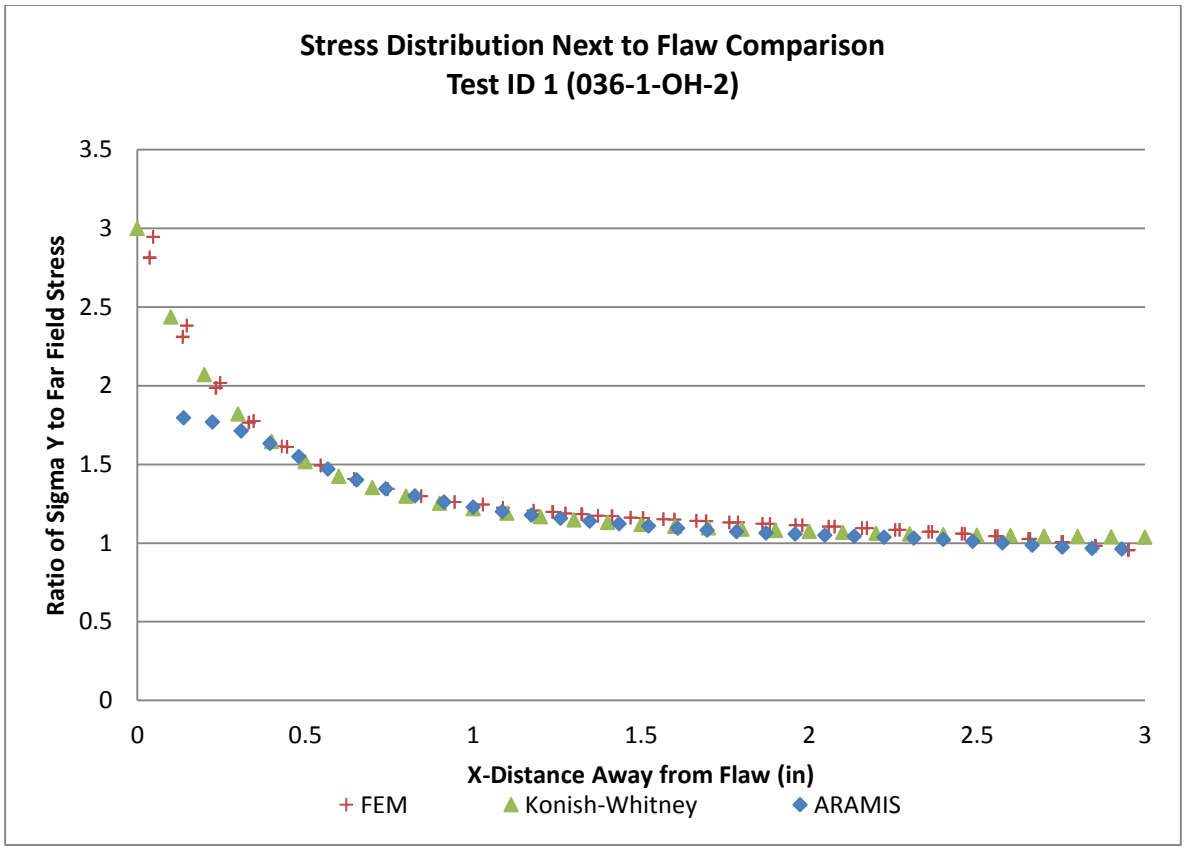

Figure 5-7 Stress distribution comparison (test ID 1)

TABLE 5-2

STRAIN COMPARISON AT ULTIMATE LOAD (TEST ID 1)

{Test ID 1} Open Hole		At Ultimate Load		
Room Temperature Ambient		Experimental [Strain Gages[1]]	Analytical [FEM]	Difference (%)
Tension Strength [ksi]		34.08	35.35	3.71
Left Rosette Strain[2] [με]	Channel 1	2722	2823	3.70
	Channel 2	6743	7217	7.04
	Channel 3	3633	3787	4.23
Right Rosette Strain[2] [με]	Channel 4	3619	3881	7.23
	Channel 5	6747	7216	6.96
	Channel 6	2703	2849	5.40
Far Field Strain[2] [με]	Channel 7	4900	5290	7.96
	Channel 8	4911	5243	6.76
	Channel 9	4843	5290	9.23
Load [lbs]	Maximum	25631	26583	3.71

Notes:
(1) Strain gage readings were taken on LJ200-036-1-OH-2, at ultimate load
(2) Strain gage schematics are as described in Section 3.6.3

5.1.2 Saw Cut Flaw

Test ID 2

Table 5-3 shows the comparison between ARAMIS and FEM strain readings at the last available load point prior to the ultimate failure locally near flaw. The difference between the two sources seems to be reasonable. For a global view of the strain distribution near the flaw across the test article width, all three strain outputs for strain in the y-direction, ε_y along the flaw centerline are shown in Figure 5-8. It must be noted that the strain distribution across the three sources seems to match considerably well across the article width except in regions of 0.5" away from the crack tips.

TABLE 5-3

STRAIN COMPARISON AT ARAMIS LAST LOAD POINT (TEST ID 2)

{Test ID 2} Saw Cut		At ARAMIS Last Load Pt		
Room Temperature Ambient		Experimental [ARAMIS[1]]	Analytical [FEM]	Difference (%)
Epsilon y, Near Flaw Max Strain[2] [με]	Right to Flaw	6650	6162	-7.34
	Left to Flaw	6670	6162	-7.61

Notes:
(1) ARAMIS readings were taken on LJ200-036-2-SC-1, at 18000lbs load (Stage 21)
(2) Near flaw strain reading was taken 0.25" away from the flaw tip/edge along flaw horizontal centerline

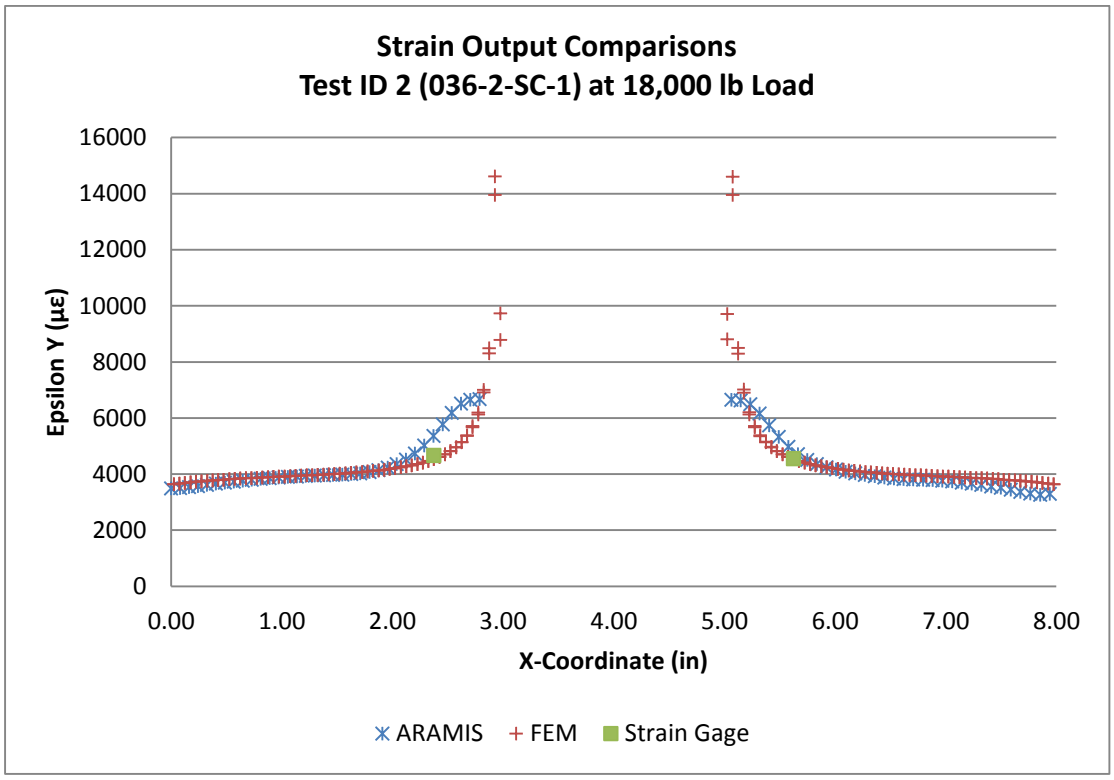

Figure 5-8 Epsilon y strain output comparisons (test ID 2)

It must be noted that ARAMIS strain output was reported in percentage (%). Strain fringe plots of the y-component of strain, ε_y from ARAMIS and FEM are shown in Figure 5-9 and Figure 5-10 respectively. The FEM fringe without averaging is shown in Figure 5-11. The

difference in maximum strain between the two sources is significant, close to 19%, even after the correction was made to the FEM to match up to the ARAMIS edge strain monitoring limitation.

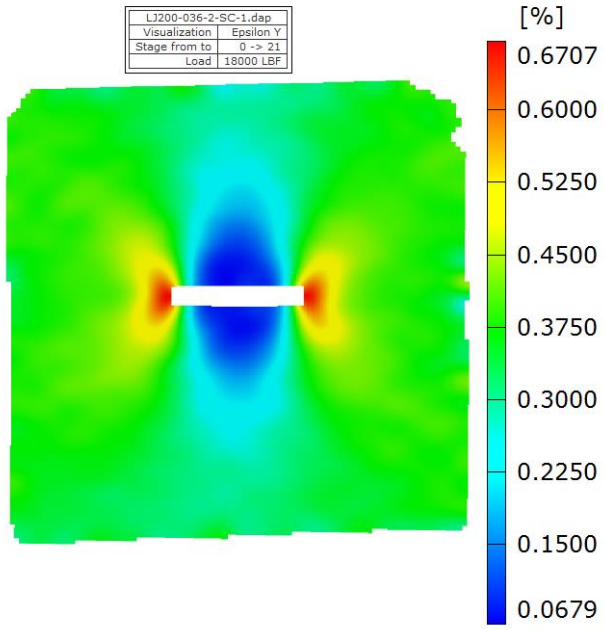

Figure 5-9 Epsilon y ARAMIS output (test ID 2)

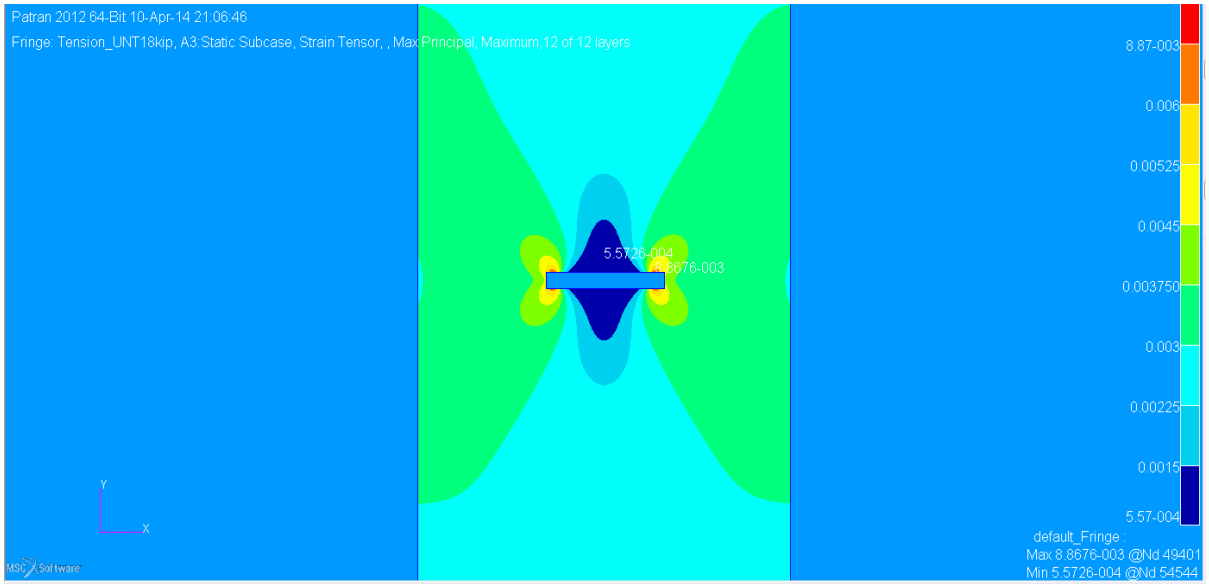

Figure 5-10 Epsilon y FEM output (test ID 2)

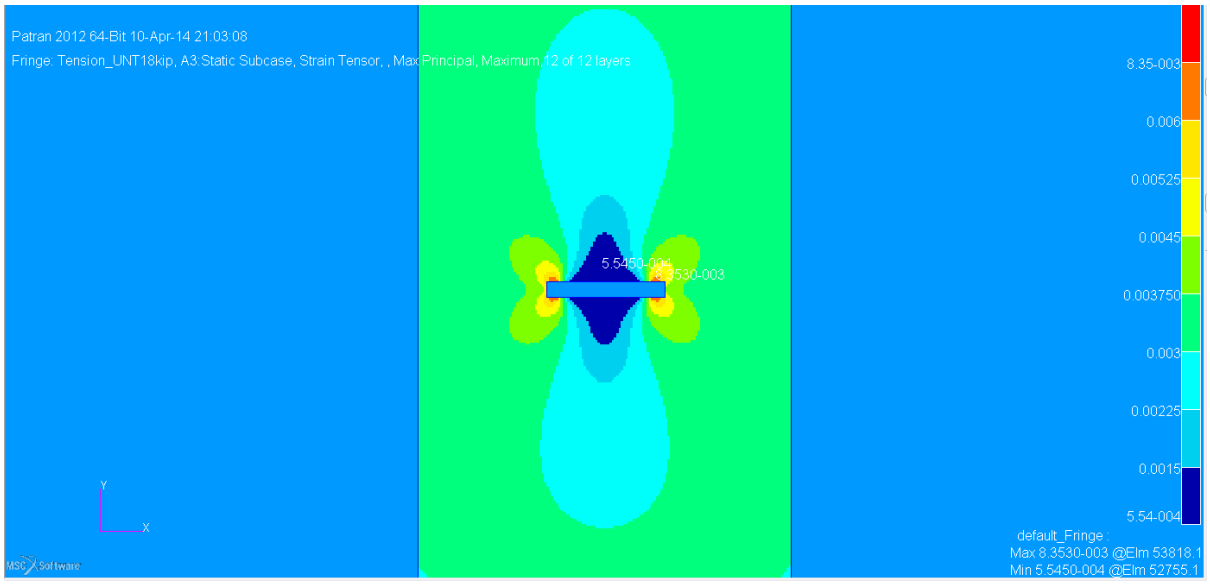

Figure 5-11 Epsilon y FEM output-no averaging (test ID 2)

Stress field distribution along the horizontal axis ahead of the flaw tip region was compared among all output sources. The stress distribution proposed by Lekhnitskii [13] for straight crack as shown in Equation (14) was plotted, and Figure 5-12 shows the comparison between the calculated stress function and outputs from FEM and ARAMIS. Strain outputs seem to match considerably well in comparison to the theoretical stress distribution, except in a region of 0.5" away from the flaw edge where ARAMIS strain output seems to deviate. Table 5-4 shows the comparison between the strain gage and FEM strain readings at ultimate load. It can be observed that the difference between the two sources seems to be within ±10% except in one strain reading.

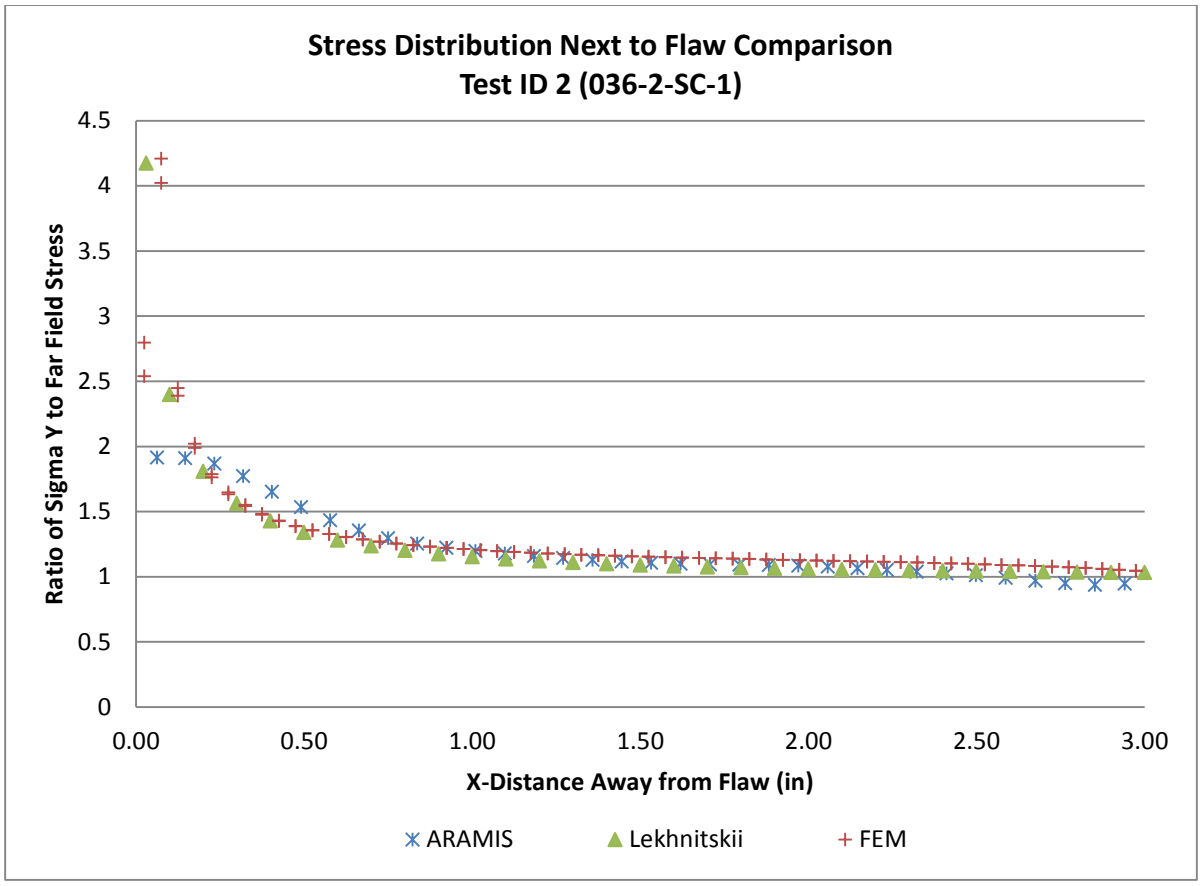

Figure 5-12 Stress distribution comparison (test ID 2)

TABLE 5-4

STRAIN COMPARISON AT ULTIMATE LOAD (TEST ID 2)

{Test ID 2} Saw Cut		At Ultimate Load		
Room Temperature Ambient		Experimental [Strain Gages[1]]	Analytical [FEM]	Difference (%)
Tension Strength [ksi]		24.19	24.14	-0.20
Left Rosette Strain[2] [με]	Channel 1	1809	1875	3.62
	Channel 2	4711	4578	-2.82
	Channel 3	3037	2641	-13.05
Right Rosette Strain[2] [με]	Channel 4	2484	2616	5.32
	Channel 5	4594	4578	-0.35
	Channel 6	1951	1807	-7.39
Far Field Strain[2] [με]	Channel 7	3490	3616	3.61
	Channel 8	3469	3602	3.82
	Channel 9	3416	3616	5.85
Load [lbs]	Maximum	18187	18151	-0.20

Notes:

(1) Strain gage readings were taken on LJ200-036-2-SC-1, at ultimate load

(2) Strain gage schematics are as described in Section 3.6.3

Test ID 5

The comparison between the ARAMIS and FEM strain readings at the last available load point prior to the ultimate failure locally near the flaw is shown in Table 5-5. The difference between the two sources seems to be very little. For a more generalized view of the strain distribution near the flaw across the test article width, all three strain outputs for strain in the y-direction, ε_y along the flaw centerline are shown in Figure 5-13. Similar to the previous two cases, the strain distribution across the three sources seems to match considerably well across the article width except in a localized region ahead of the crack tip.

TABLE 5-5

STRAIN COMPARISON AT ARAMIS LAST LOAD POINT (TEST ID 5)

{Test ID 5} Saw Cut		At ARAMIS Last Load Point		
Room Temperature Ambient		Experimental [ARAMIS[1]]	Analytical [FEM]	Difference (%)
Epsilon y, Near Flaw Max Strain[2] [με]	Right to Flaw	5917	5824	-1.57
	Left to Flaw	5231	5274	0.82

Notes:
(1) ARAMIS readings were taken on LJ200-036-5-SC-2, at 32000lbs load (Stage 17)
(2) Strain reading for near flaw was taken 0.25" away from the flaw tip/edge along flaw horizontal centerline

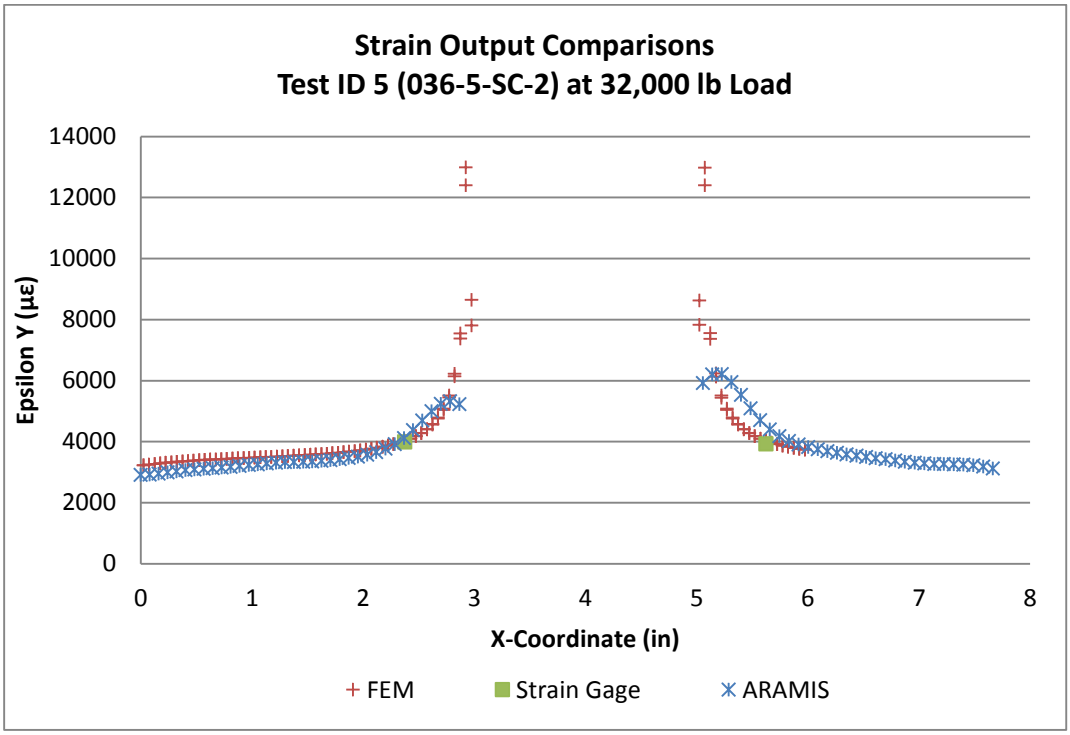

Figure 5-13 Epsilon y strain output comparison (test ID 5)

Strain fringe plots of the y-component of strain, ε_y from ARAMIS and FEM are shown in Figure 5-14 and Figure 5-15 respectively. For comparison of maximum strain values between the two sources, the averaging option within the FEM fringe plotting was not selected as shown in Figure

5-16. The difference in maximum strain between the two sources is in the region of 14% after the correction was made to FEM to match up to the ARAMIS edge strain monitoring limitation.

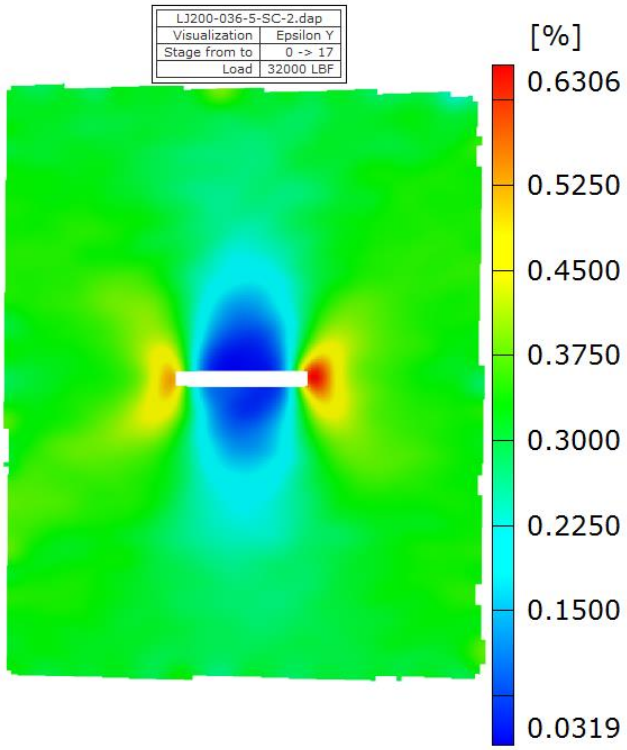

Figure 5-14 Epsilon y ARAMIS output (test ID 5)

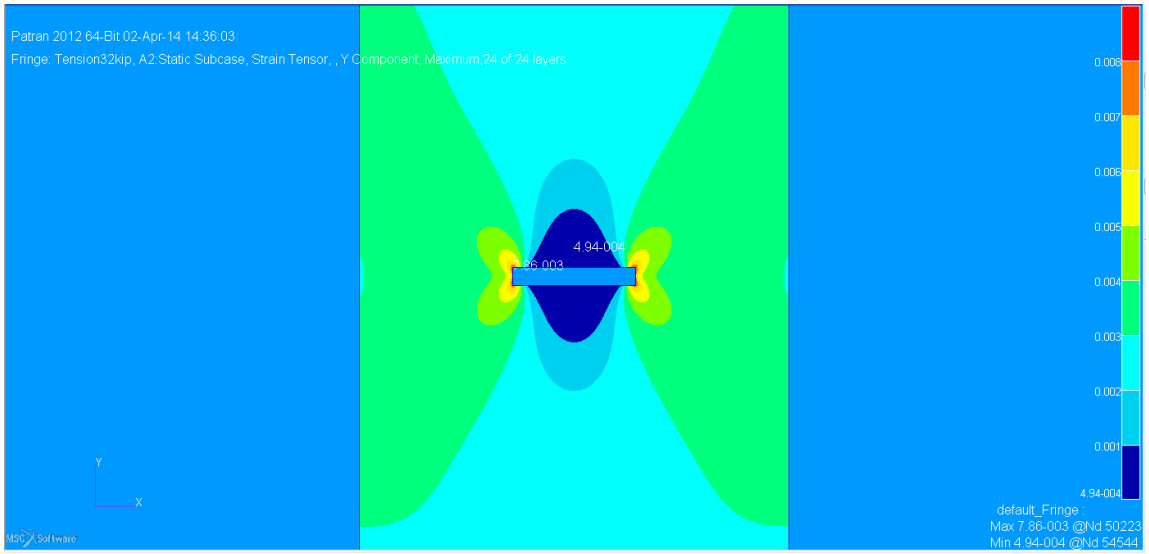

Figure 5-15 Epsilon y FEM output (test ID 5)

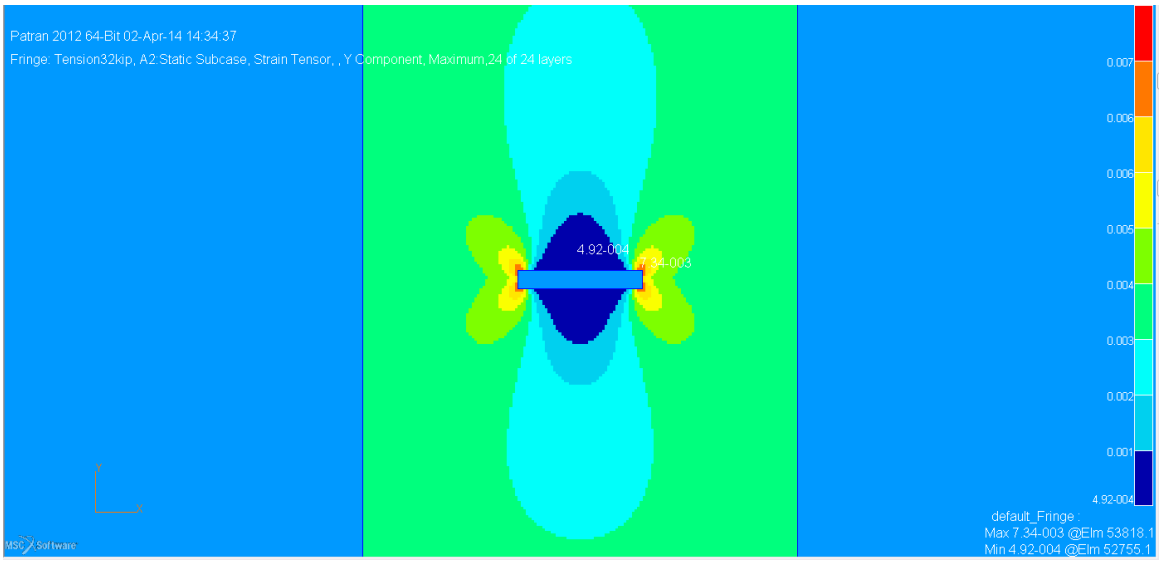

Figure 5-16 Epsilon y FEM output-no averaging (test ID 5)

The stress field distribution along the horizontal axis ahead of the flaw tip region was compared among all output sources. The stress distribution proposed by Lekhnitskii [13] for straight crack as shown in Equation (14) was plotted against outputs from FEM and ARAMIS in Figure 5-17. As seen in the previous cases, the strain outputs seem to match considerably well in comparison to the theoretical stress distribution except in a region of about 0.6" away from the flaw edge where ARAMIS strain output seems to deviate. Table 5-6 shows the comparison between the strain gage and the FEM strain readings at ultimate load. It can be observed that the difference between the two sources seems to be within ±10% in all strain readings.

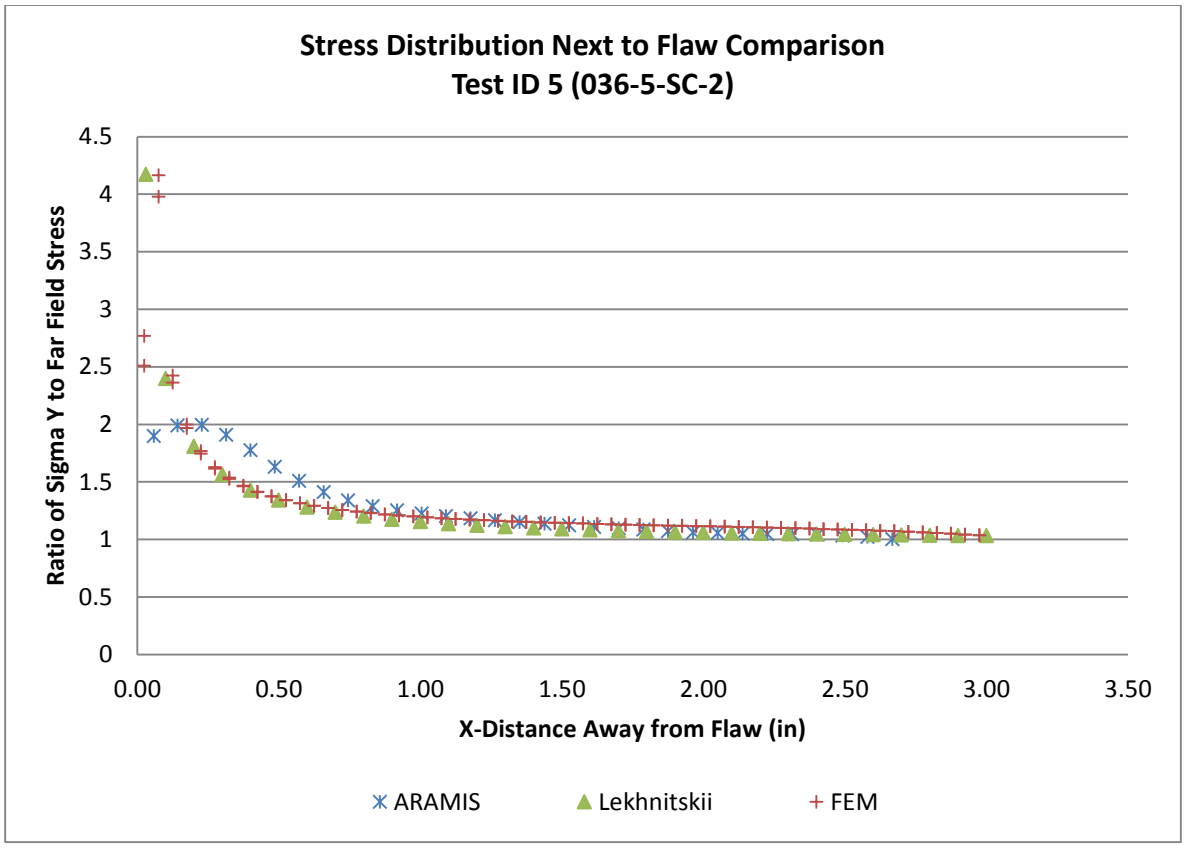

Figure 5-17 Stress distribution comparison (test ID 5)

TABLE 5-6

STRAIN COMPARISON AT ULTIMATE LOAD (TEST ID 5)

{Test ID 5} Saw Cut		At Ultimate Load		
Room Temperature Ambient		Experimental [Strain Gages[1]]	Analytical [FEM]	Difference (%)
Tension Strength [ksi]		22.35	24.56	9.88
Left Rosette Strain[2] [με]	Channel 1	1595	1715	7.55
	Channel 2	4153	4186	0.80
	Channel 3	2556	2415	-5.53
Right Rosette Strain[2] [με]	Channel 4	2290	2392	4.46
	Channel 5	4083	4186	2.51
	Channel 6	1633	1652	1.17
Far Field Strain[2] [με]	Channel 7	3036	3306	8.90
	Channel 8	3252	3294	1.30
	Channel 9	2984	3306	10.78
Load [lbs]	Maximum	33259	36546	9.88

Notes:

(1) Strain gage readings were taken on LJ200-036-5-SC-2, at ultimate load

(2) Strain gage schematics are as described in Section 3.6.3

Test ID 7

For this test ID, there are no ARAMIS data available to date. Thus, the FEM strain output comparison can only be made against the strain gage readings. Table 5-7 shows how well the strain gage and FEM strain readings at ultimate load fare. The difference between the two sources seems to be quite large in some strain readings but most of them seem to fall within ±10%.

TABLE 5-7

STRAIN COMPARISON AT ULTIMATE LOAD (TEST ID 7)

{Test ID 7} Saw Cut		At Ultimate Load		
Room Temperature Ambient		Experimental [Strain Gages[1]]	Analytical [FEM]	Difference (%)
Tension Strength [ksi]		15.19	15.20	0.08
Left Rosette Strain[2] [με]	Channel 1	1529	1707	11.63
	Channel 2	3585	3706	3.37
	Channel 3	2241	2732	21.92
Right Rosette Strain[2] [με]	Channel 4	2244	2706	20.58
	Channel 5	3490	3706	6.20
	Channel 6	1403	1724	22.86
Far Field Strain[2] [με]	Channel 7	2073	2366	14.14
	Channel 8	2133	2362	10.72
	Channel 9	2128	2366	11.17
Load [lbs]	Maximum	29775	29800	0.08

Notes:

(1) Strain gage readings were taken on LJ200-036-7-SC-1, at ultimate load

(2) Strain gage schematics are as described in Section 3.6.3

Test ID 8

Similar to the previous case, there are no ARAMIS data available to date for this test ID. Thus, the FEM strain output comparison can only be made against the strain gage readings. The difference between the two sources seems a lot better than that of test ID 7, with all of the readings falling within ±17% as shown in Table 5-8.

TABLE 5-8

STRAIN COMPARISON AT ULTIMATE LOAD (TEST ID 8)

{Test ID 8} Saw Cut		At Ultimate Load		
Room Temperature Ambient		Experimental [Strain Gages[1]]	Analytical [FEM]	Difference (%)
Tension Strength [ksi]		15.43	15.44	0.05
Left Rosette Strain[2] [με]	Channel 1	1689	1708	1.15
	Channel 2	3560	3707	4.13
	Channel 3	2850	2733	-4.11
Right Rosette Strain[2] [με]	Channel 4	2867	2707	-5.58
	Channel 5	3923	3707	-5.50
	Channel 6	2048	1724	-15.81
Far Field Strain[2] [με]	Channel 7	2033	2367	16.45
	Channel 8	2207	2363	7.06
	Channel 9	2039	2367	16.06
Load [lbs]	Maximum	59570	59600	0.05

Notes:

(1) Strain gage readings were taken on LJ200-036-8-SC-1, at ultimate load

(2) Strain gage schematics are as described in Section 3.6.3

5.2 Residual Strength of Composite Laminates

All experimental data obtained from Chapter 3 were combined with unnotched tension and open hole tension data evaluated at lamina and laminate level testing. The WN Point Stress criterion and the ML fracture model were evaluated and fitted with the experimental data. For the ML model, the two constants, H_C and n were determined from the linear regression analysis of Equation (20) which is in log-log plot. From the exercise, it was observed that the two constants vary with the flaw type as reported in Table 5-9 and Figure 5-18.

TABLE 5-9

MAR-LIN MODEL CONSTANT DETERMINATION

Flaw Type	Order of Singularity (n)	Fracture Toughness (H_C)
Open Hole	0.157	39.99 ksi
Saw Cut	0.437	32.98 ksi
Combined	0.367	33.54 ksi

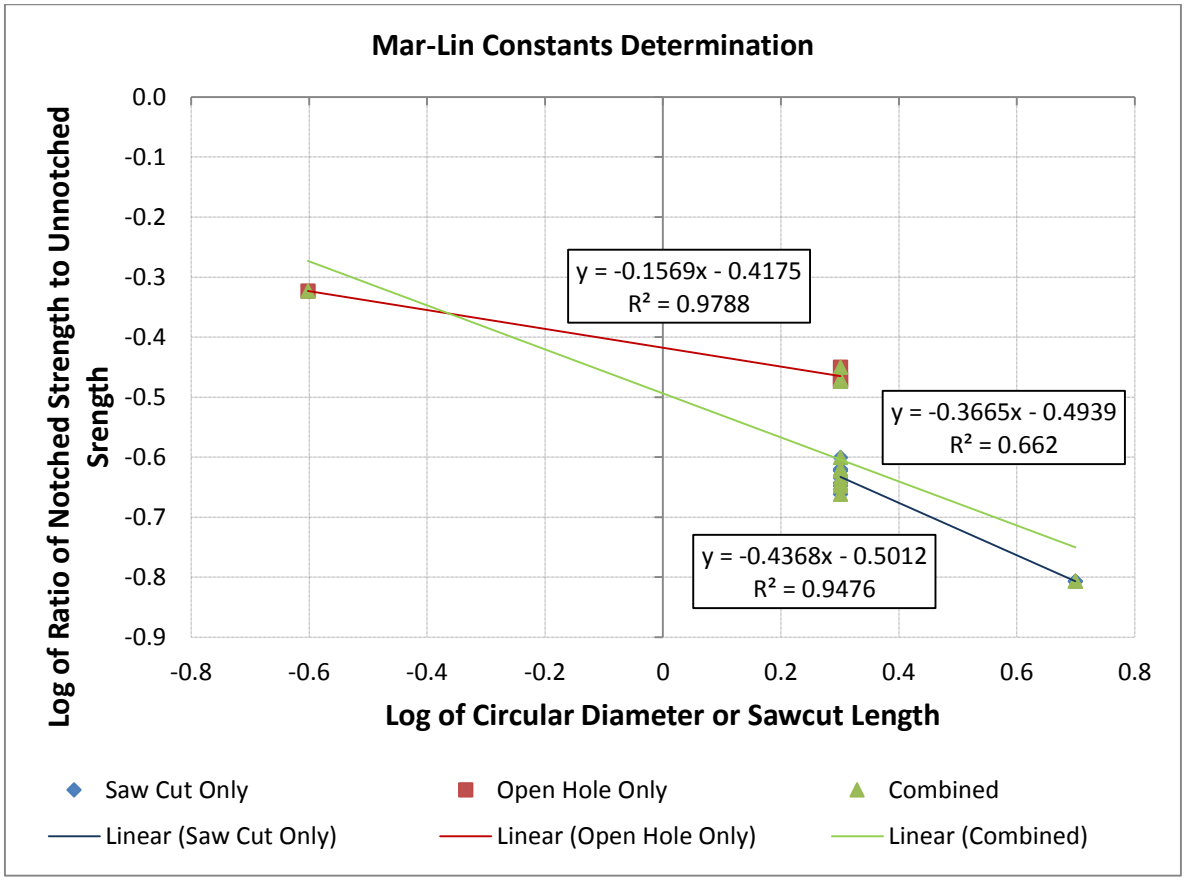

Figure 5-18 Linear regression analysis for Mar-Lin constants determination

Shown in Figure 5-19 are the residual strength curves for the open hole and saw cut flaws with various characteristic distances used. For the WN Point Stress criterion, a several selection of characteristic dimension, a was selected to show the effects of characteristic dimension on the residual strength curves. It must be noted that using the Point Stress WN fracture model, the best

selections of characteristic dimension, *a* that produce the best curve-fit for the open hole and saw cut flaws are 0.020" and 0.030" respectively. From the mesh sensitivity studies in Section 4.3.1, the optimum mesh size range for all test cases was determined to be in the region of 0.040" to 0.070". Due to the fact that centroidal strain and stress outputs were used (refer to Section 4.1.5), this means that the analytical-based characteristic dimensions are in the region of 0.020" to 0.035". The experimental-based characteristic dimensions match perfectly with the analytical-based characteristic dimensions.

As for the ML fracture model, the model fits very well with the experimental data sets and produces similar residual strength curves to those of the WN model for a saw cut flaw. On the other hand, the ML model produces a more conservative residual strength curve for the circular hole, especially in the region of two-inch hole size and larger. For illustrations of the best curve-fit functions for each flaw type and each fracture model, the curves are shown in Figure 5-20.

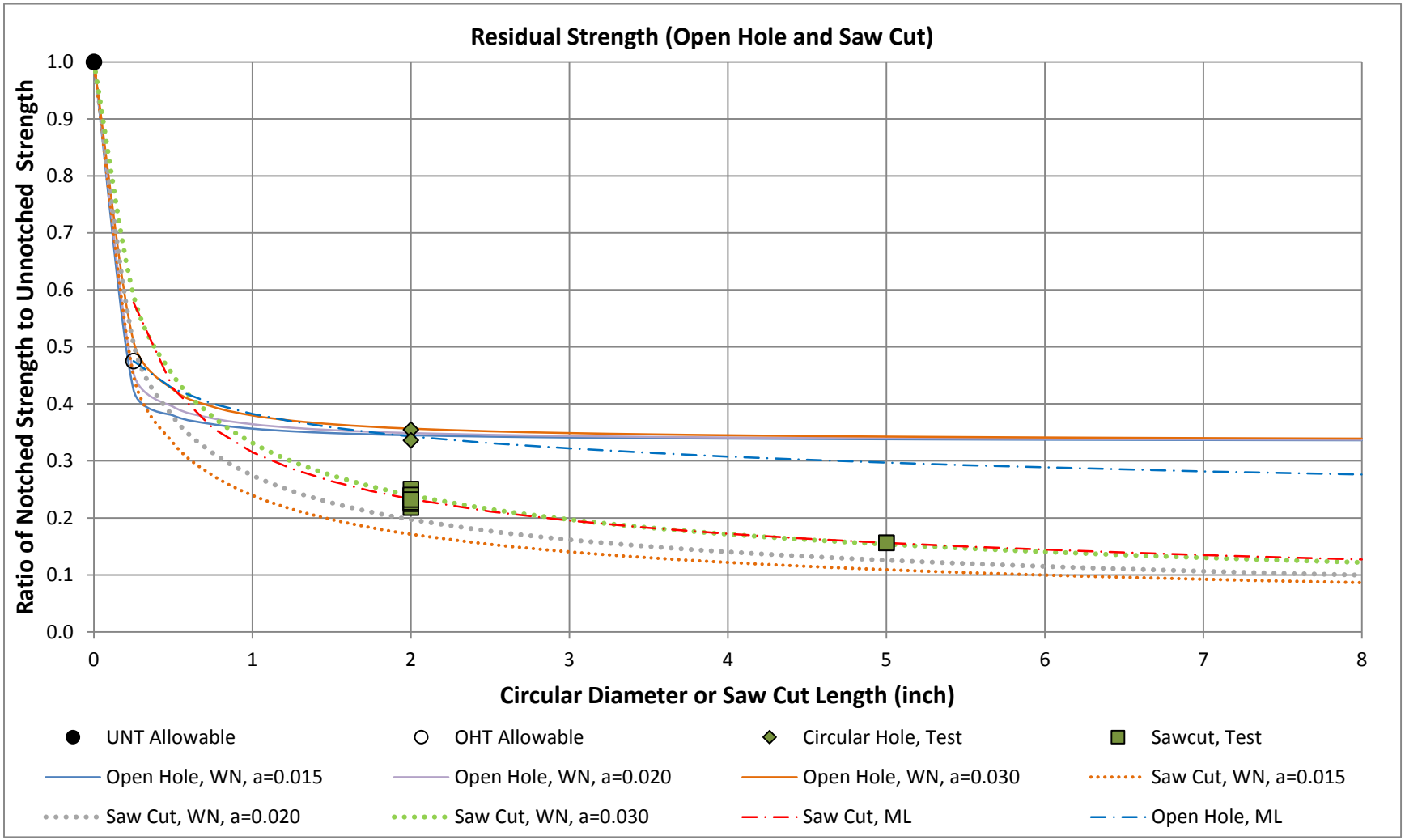

Figure 5-19 Residual strength plot comparisons (open hole and saw cut)

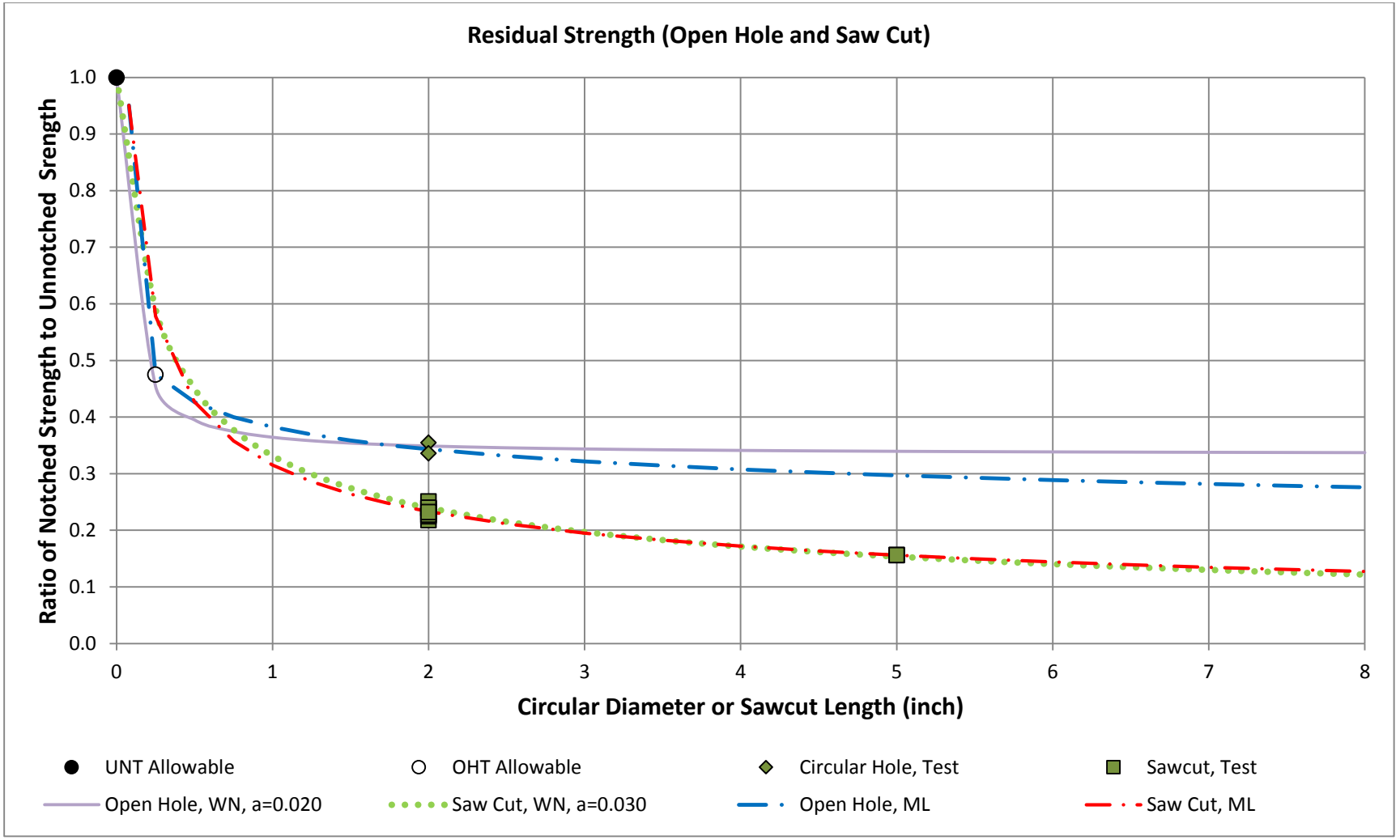

Figure 5-20 Best curve-fit residual strength plot (open hole and saw cut)

CHAPTER 6

CONCLUSIONS

6.1 Summary

In this study, the evaluation of the notched residual strength of laminated composite materials under uniaxial tension was performed with an extra focus on large damage sizes and narrow slit notch types. The effects of flaw size and flaw type on the residual strength of a laminate can be observed, and the difference between the flaw types gets more substantial for a notch size of one inch and larger. This shows that a narrow slit or a saw cut damage is far more critical than a circular hole cut-out due to the ellipsoidal nature of the flaw. The notch sensitivity is also well described via the order of the singularity of the function. Thus, it must be cautioned that if a residual strength prediction is only generated from small notch data, the resulting residual strength estimate will be unconservative.

In addition, the subject prepreg system studied shows residual strength properties that correlate well with commonly used composite fracture mechanics models, namely the WN and ML models with the best-fit characteristic dimensions matching up well with those used in the FEM. It is also worth noting how the analytical outputs correlate well with the responses found in the experimental study. Parametric studies of the FEM analysis variables also pointed out the influence of the studied variables when compared to the experimental data. The analysis methods as proposed within this thesis will provide a path for analysts to gain insights on the influence of each FEM parameter in failure prediction of notched composites.

6.2 Future Work

6.2.1 Experimental Study

An expanded scope of the study and the overall test matrix is presented in Appendix C. As shown in Appendix C, an additional loading case will be studied, focusing on compression loading. With the compression loading, the complexity level increases with the possibilities of flaw collapse or closing for the case of narrow slits. Verification of the best-fit characteristic dimensions for each notch type will be performed to evaluate if similar dimensions are still applicable for a different mode of loading.

In addition, a typical full operating temperature envelope for an aircraft will be further studied. This means performing tests at an elevated temperature and high humidity level, which is normally deemed as the worst case condition for matrix-dominated or –dependent failures. Proper balance has to be struck when testing at the elevated wet test condition, as it becomes easily unfeasible in reality as test article size or thickness increases. Additionally, from the literature review, it was reported that notch sensitivity is a function of laminate configuration and notch types. Thus, a wide spectrum of varying AML typical in aircraft design will be included in the next study. Another scope of interest is how much notch orientation relative to loading direction is an influencing factor in the resulting residual strength. Variations of notch orientation, such as in angled position relative to the primary loading direction, introduce an additional complexity as the loading mode is no longer a typical Mode I dominant loading.

Improvements can also be made on the flaw edge strain monitoring capability by the ARAMIS photogrammetric system. One idea is to put a soft dummy material such as putty to fill in the notch to smooth out the edge boundary effect. In future experimental tests, strain

monitoring efforts will also be entirely focused on the localized region ahead of the flaw tip for greater strain resolution in this critical region.

6.2.2 Analytical Study

Future analytical study will further explore an expanded use of micromechanics softwares to better understand failure progression involved with notched laminates associated with micromechanical phenomena such as fiber breakage, interply delamination and matrix micro-cracking [4]. The study would hope to bring in a sense of limit load capability of notched laminates which is normally associated with first ply failure at greater scrutiny on damages at the macro-level and micro-level. One of the intents is to correlate the simulation to the reported first audible crack in the experimental data. Another would be to improve the first ply failure prediction, thus providing an additional safety margin to residual strength prediction of a structure.

REFERENCES

REFERENCES

[1] ASTM D 5766/D5766M-11, "Standard Test Method for Open-Hole Tensile Strength of Polymer Matrix Composite Laminates," (2011)

[2] Irwin, G. R., "Analysis of Stresses and Strains Near the End of a Crack Traversing a Plate," ASME *Journal of Applied Mechanics* (1957)

[3] Yeh, H.-Y., Berryhill, R. K. and Yeh, H.-L., "Analytical Damage-Zone Size Predictions for Notched Laminated Composites," *Journal of Reinforced Plastics and Composites* (2004)

[4] Talreja, R. and Singh, C. V., "Damage and Failure of Composite Materials," First Edition, Cambridge University Press (2012)

[5] Awerbuch, J. and Madhukar, M. S., "Notched Strength of Composite Laminates: Prediction and Experiments-A Review," *Journal of Reinforced Plastics and Composites*, (1985)

[6] Zhen, S., "The D Criterion Theory in Notched Composite Materials," *Journal of Reinforced Plastics and Composites* (1983)

[7] Waddoups, M. E., Eisenmann, J. R. and Kaminski, B. E., "Macroscopic Fracture Mechanics of Advanced Composite Materials," *Journal of Composite Materials*, Vol. 5, (1971)

[8] Paris, P.C. and Sih, G. C., "Stress Analysis of Cracks," *Fracture Toughness Testing and Its Applications*, ASTM STP 381, American Society of Materials (1965)

[9] Irwin, G. R., "Fracture Dynamics, " *Fracturing of Metals*, American Society of Metals (1948)

[10] Wu, E. M., "Fracture Mechanics of Anisotropic Plates," *Composite Materials Workshop*, S. W. Tsai, J.C. Halpin and N. J. Pagano, Eds., Technomic Pub. Co., Inc., Lancaster, PA (1968)

[11] Whitney, J. M. and Nuismer, R. J., "Stress Fracture Criteria for Laminated Composites Containing Stress Concentrations," *Journal of Composite Materials* (1974)

[12] Konish, H. J. and Whitney, J. M., "Approximate Stresses in an Orthotropic Plate Containing a Circular Hole," *Journal of Composite Materials* (1975)

[13] Lekhnitskii, S. G., "Anisotropic Plates," Translated from the Second Russian Edition by S.W. Tsai and T. Cheron, Gordon and Breach, Science Publishers, Inc., New York (1968)

[14] Mar, J.W. and Lin, K. Y., "Fracture Mechanics Correlation for Tensile Failure of Filamentary Composites with Holes," *Journal of Airctaft*, Vol. 14, No. 7, pp. 703-704 (1977)

[15] Mar, J. M. and Lin, K. Y., "Fracture of Boron/Aluminum Composites with Discontinuities," *Journal of Composite Materials,* Vol. 11, pp. 405-421 (1977)

[16] Walker, T. H., Avery, W. B., Ilcewicz, L. I., Poe, C. C., Jr., and Harris, C. E., "Tension Fracture of Laminates for Transport Fuselage-Part I: Material Screening," *Second NASA Advanced Technology Conference*, NASA CP 3154, pp. 197-238 (1991)

[17] Gerber Technology, URL: http://www.gerbertechnology.com [cited April 9, 2014]

[18] ASTM D3039/D3039M-08, "Standard Test Method for Tensile Properties of Polymer Matrix Composite Materials," (2008)

[19] GOM ARAMIS Optical 3D Deformation Analysis Measuring System, URL: http://www.gom.com/metrology-systems/system-overview/aramis.html [cited April 9, 2014]

[20] MSC Patran 2012, URL: http://www.mscsoftware.com/product/patran [cited April 9, 2014]

[21] MSC Nastran 2008, URL: http://www.mscsoftware.com/product/msc-nastran [cited April 9, 2014]

[22] MSC SimCompanion, URL:http://simcompanion.mscsoftware.com/infocenter/index?page=content&channel=documentation [cited April 9, 2014]

[23] Composite Materials Handbook, "Polymer Matrix Composites-Guidelines for Characterization of Structural Materials," Vol. 1, Rev. F

[24] Composite Materials Handbook, "Polymer Matrix Composites: Materials Usage, Design and Analysis," Vol. 3, Rev. F

[25] Daniel, I. M. and Ishai, O., "Engineering Mechanics of Composite Materials," Second Edition, Oxford University Press (2006)

[26] Tsai, S. W., "A Survey of Macroscopic Failure Criteria for Composite Materials," *Journal of Reinforced Plastics and Composites*, Vol. 3, pp. 40-62 (1984)

[27] Sun, C. T., "Strength Analysis of Unidirectional Composites and Laminates," *Comprehensive Composite Materials*, pp. 641-666 (2000)

[28] Hinton, M. J., Soden, P. D. and Kaddour, A. S., "Failure Criteria in Fibre-Reinforced Polymer Composites," Elsevier, Oxford (2004)

[29] Wisnom, M. R., Khan, B. and Hallett, S. R., "Size Effects in Unnotched Tensile Strength of Unidirectional and Quasi-isotropic Carbon/Epoxy Composites," *Journal of Composite Structures*, Vol. 84, Issue 1, pp. 21-28 (2008)

[30] Mori, T. and Tanaka, K., "Average Stress in the Matrix and Average Elastic Energy of Materials with Misfitting Inclusions," *Acta Metallurgica*, Vol. 21, Issue 5, pp. 571-574 (1973)

[31] Nemat-Nasser, S. and Hori, M., "Micromechanics: Overall Properties of Heterogeneous Solids," *Elvesier Science* (1993)

[32] MSC Digimat-MF, Version 5.0.1, URL: http://www.mscsoftware.com/product/digimat [cited April 9, 2014]

[33] Autodesk Simulation Composite Design, Version 2014.0.0, URL: http://www.autodesk.com/products/autodesk-simulation-family/features/simulation-composite-design/all/gallery-view [cited April 9, 2014]

[34] Wang, X., Ravirala, N., Abichou, H. and Dixon, M., "Finite Element Prediction of Effect of Ribbon Sensor on the Mechanical Properties of Carbon Fibre/Epoxy Woven Composites," International Conference on Composite Materials (2009)

APPENDICES

APPENDIX A

PHOTOGRAPHS OF TESTED ARTICLES

LJ200-036-1-OH-1

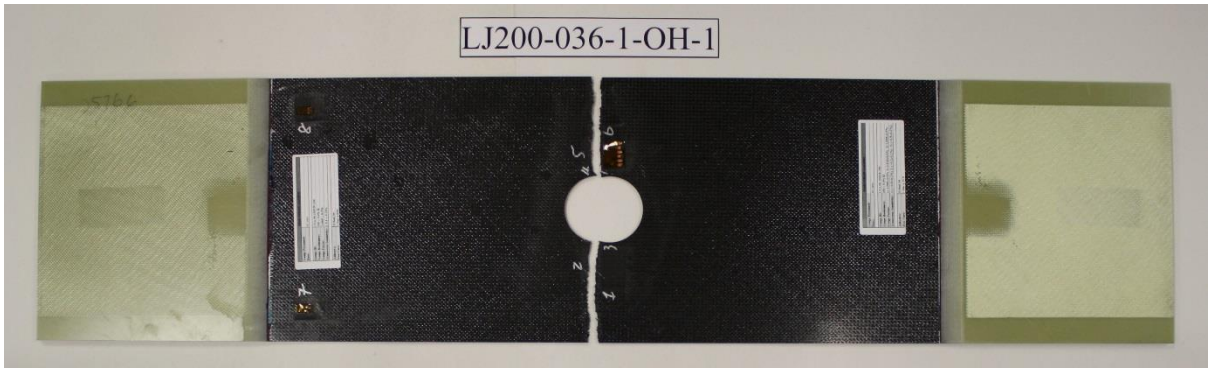

FRONT SIDE

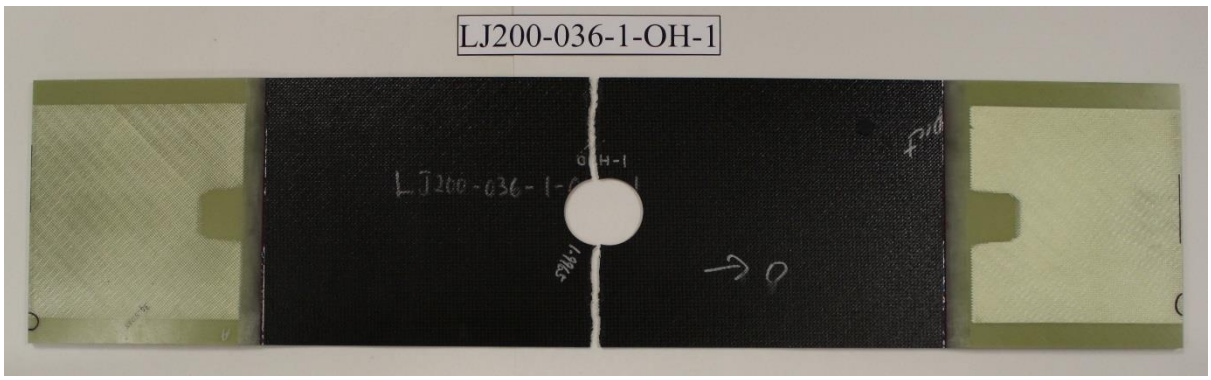

BACK SIDE

LJ200-036-1-OH-2

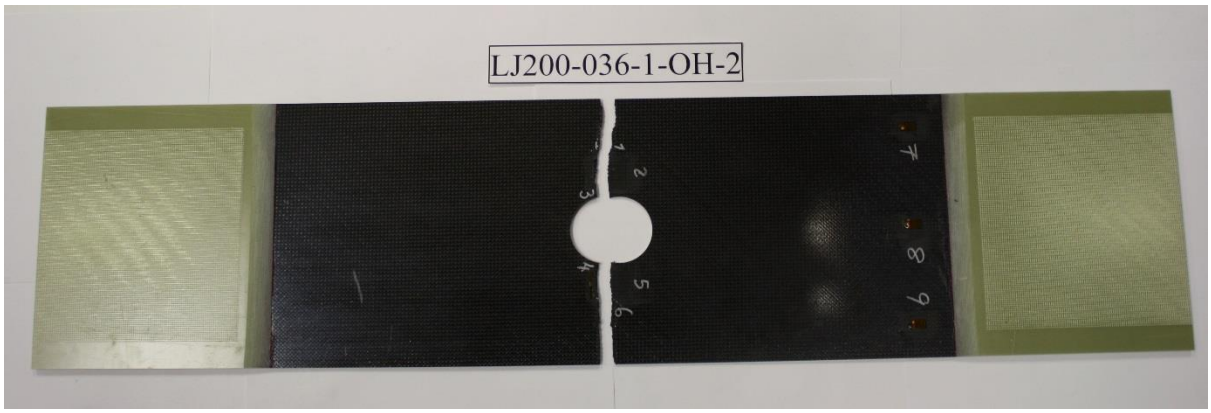

FRONT SIDE

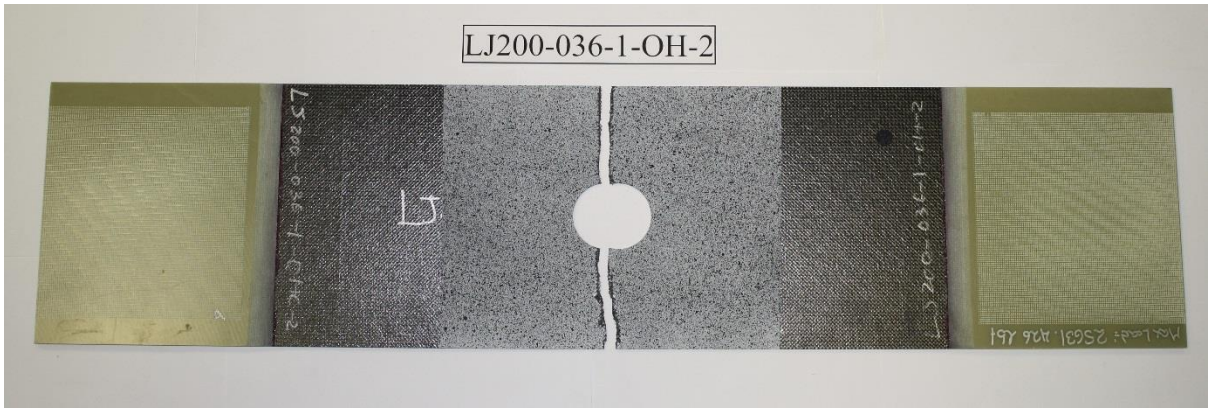

BACK SIDE

LJ200-036-1-OH-3

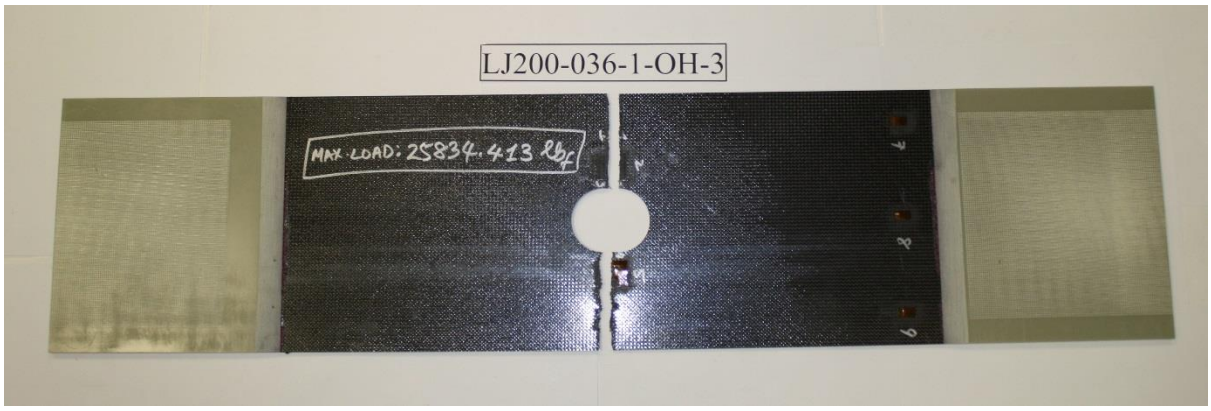

FRONT SIDE

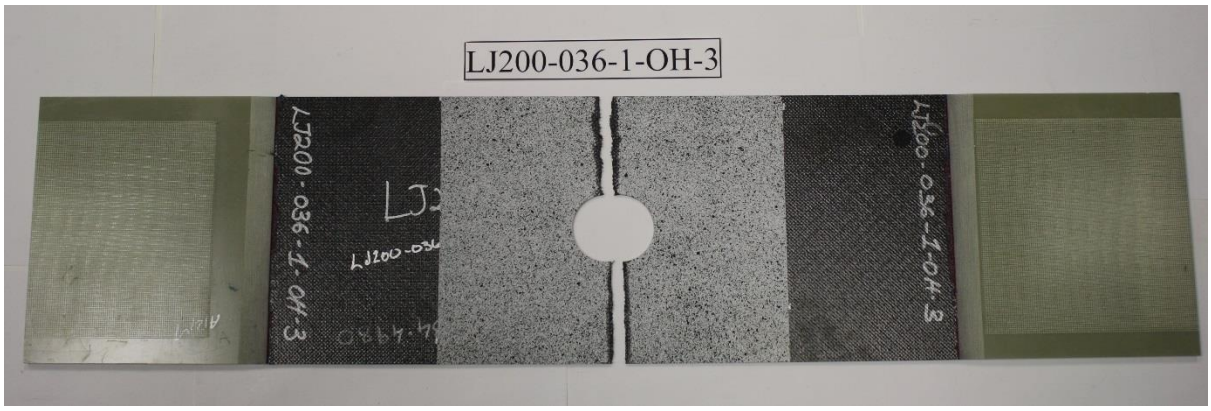

BACK SIDE

LJ200-036-2-SC-1

FRONT SIDE

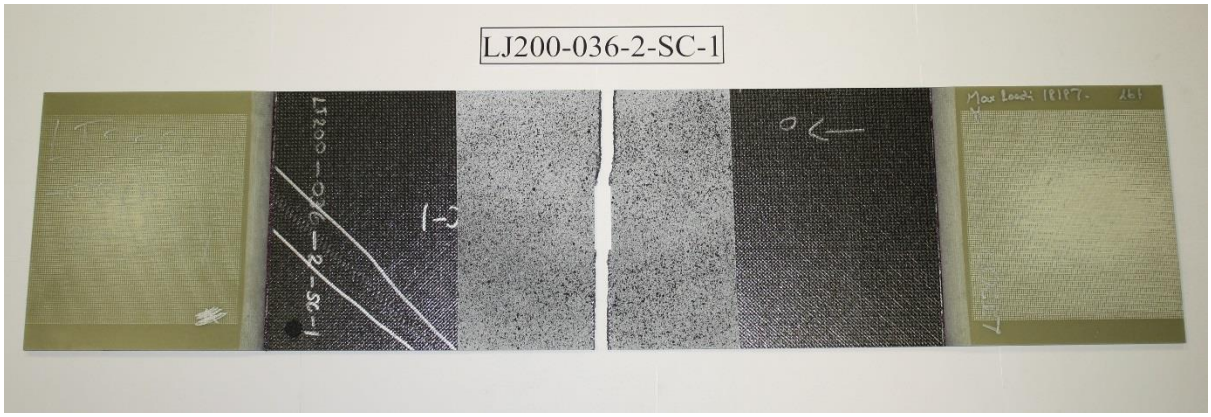

BACK SIDE

LJ200-036-2-SC-2

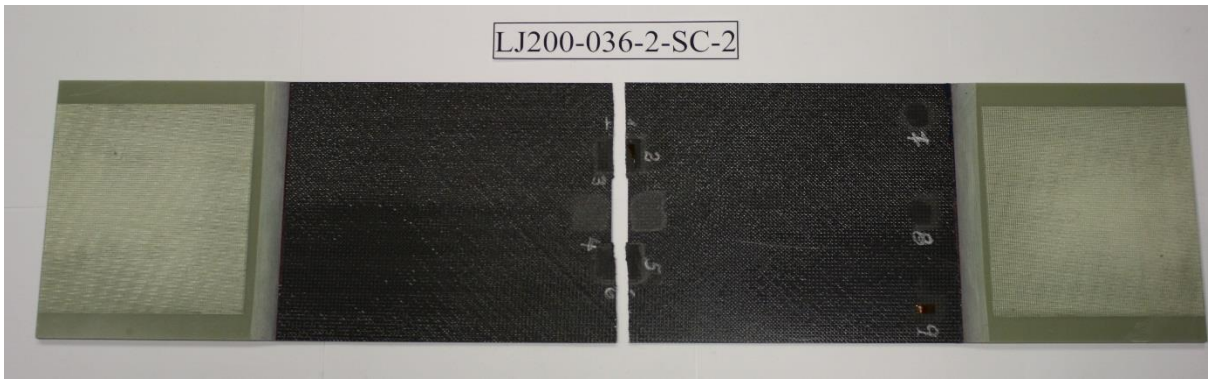

FRONT SIDE

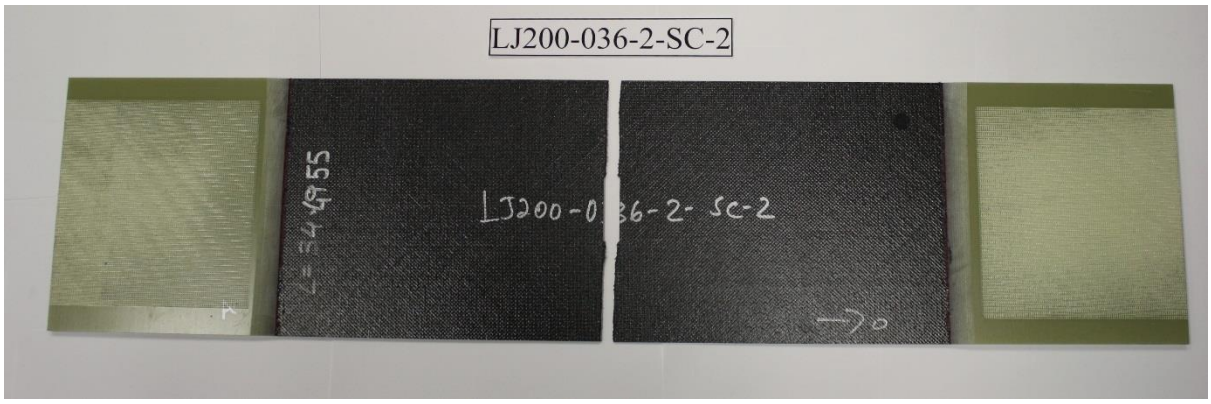

BACK SIDE

LJ200-036-2-SC-3

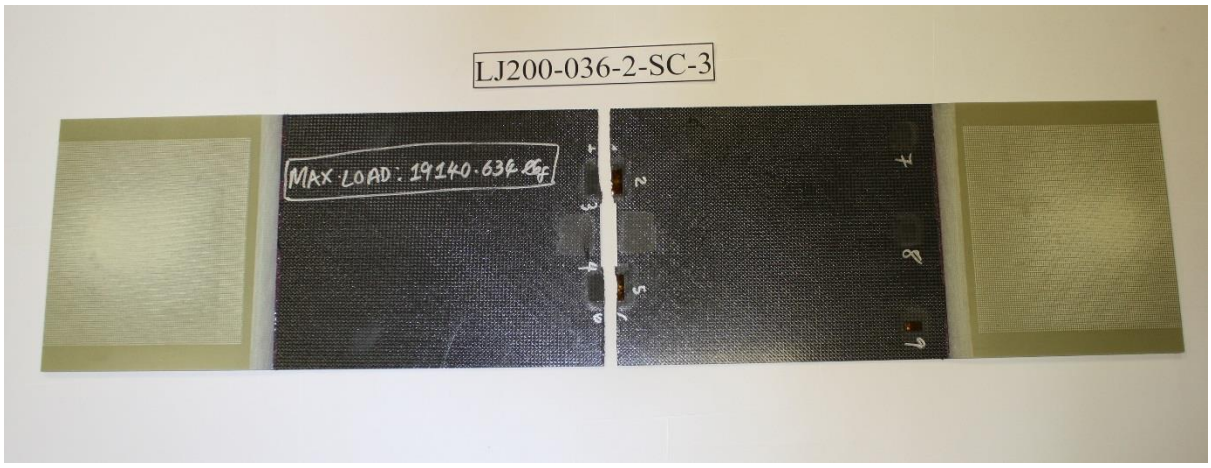

FRONT SIDE

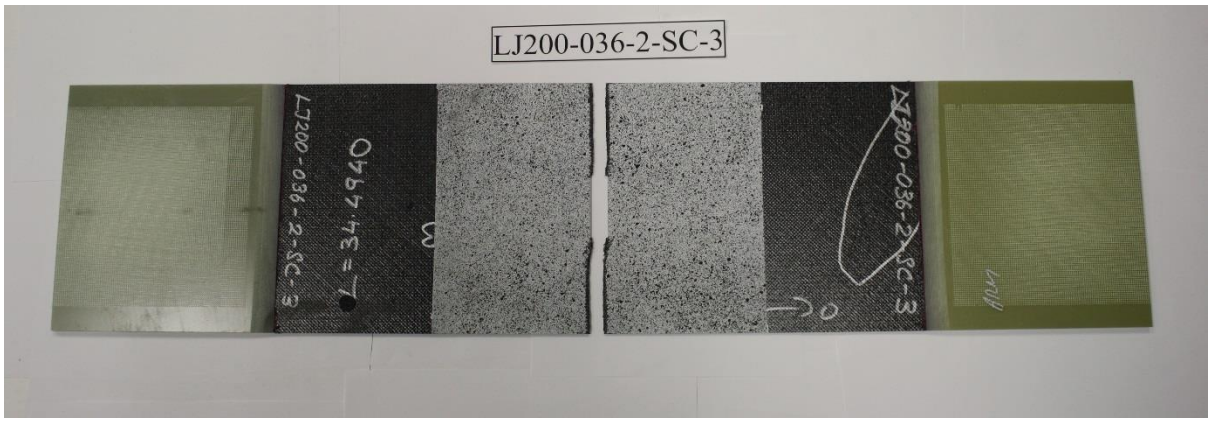

BACK SIDE

LJ200-036-3-SC-1

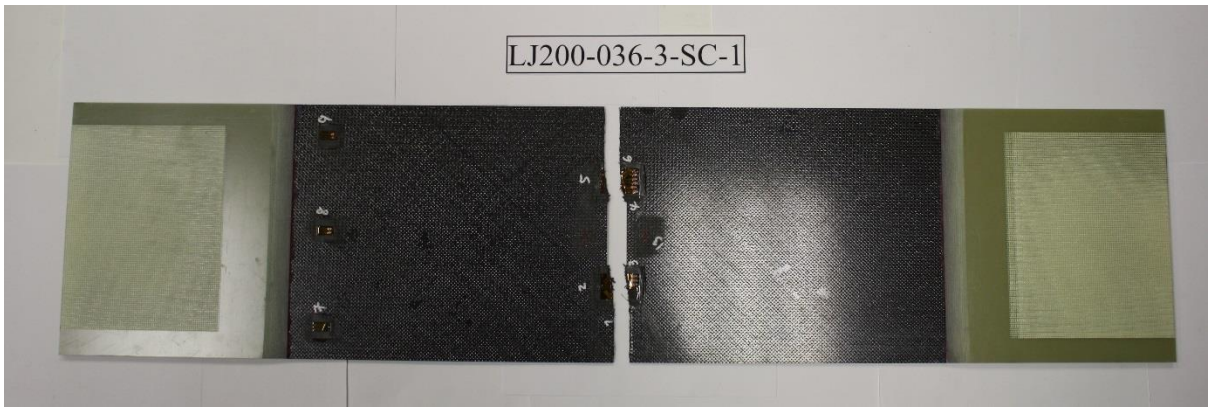

FRONT SIDE

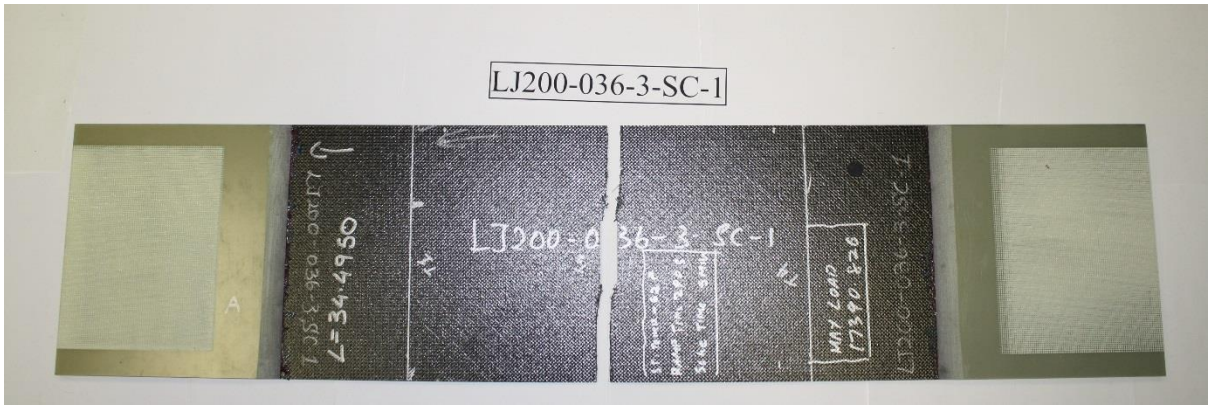

BACK SIDE

LJ200-036-3-SC-2

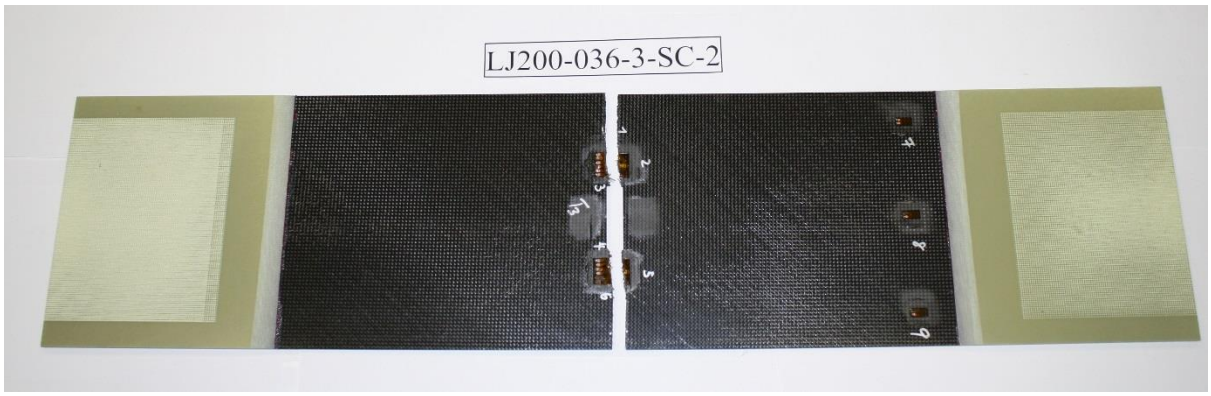

FRONT SIDE

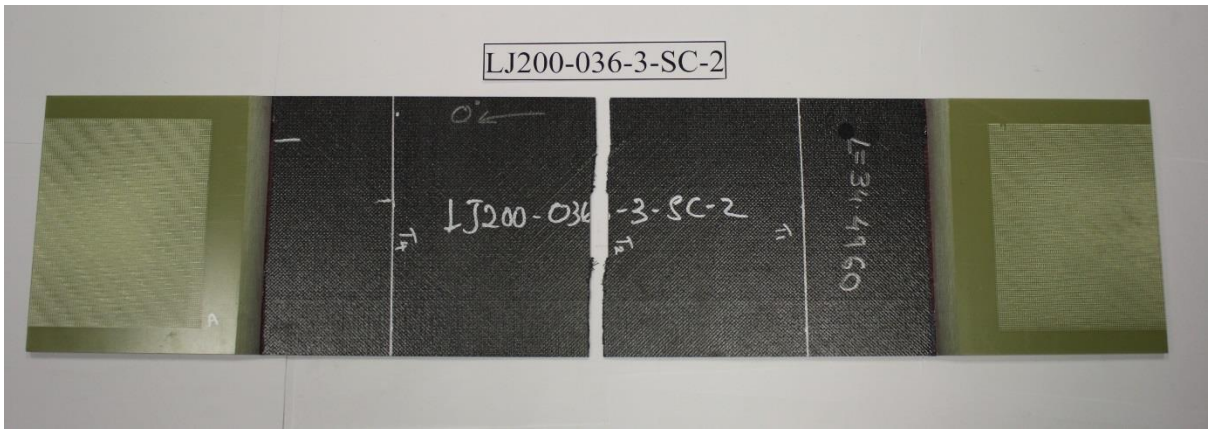

BACK SIDE

LJ200-036-3-SC-3

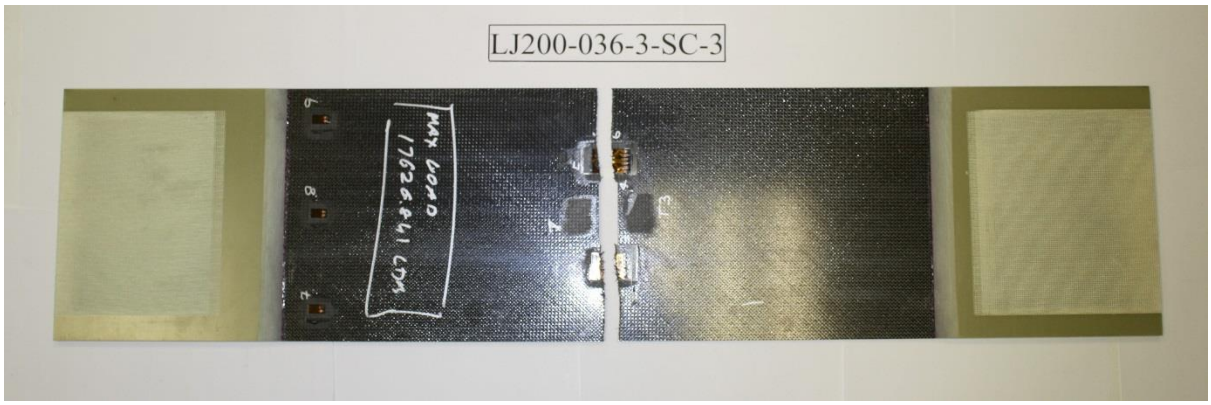

FRONT SIDE

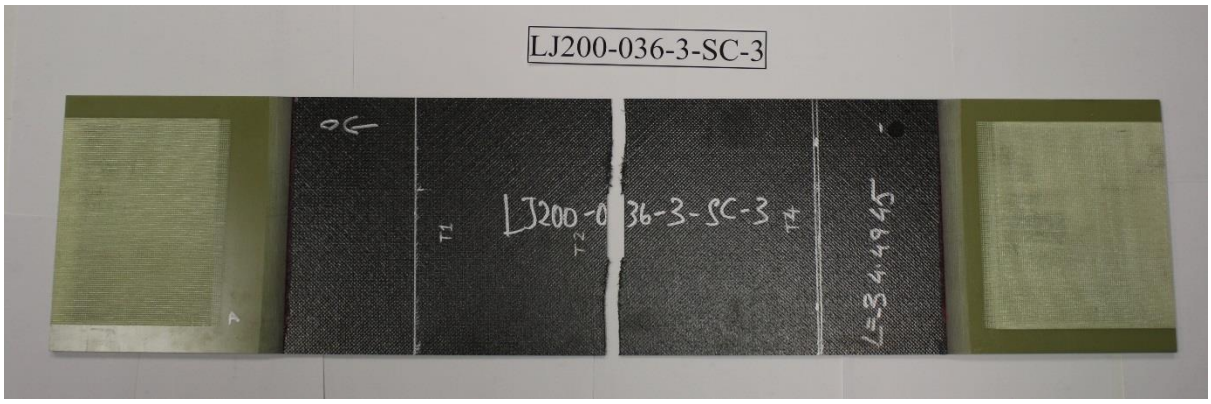

BACK SIDE

LJ200-036-5-SC-1

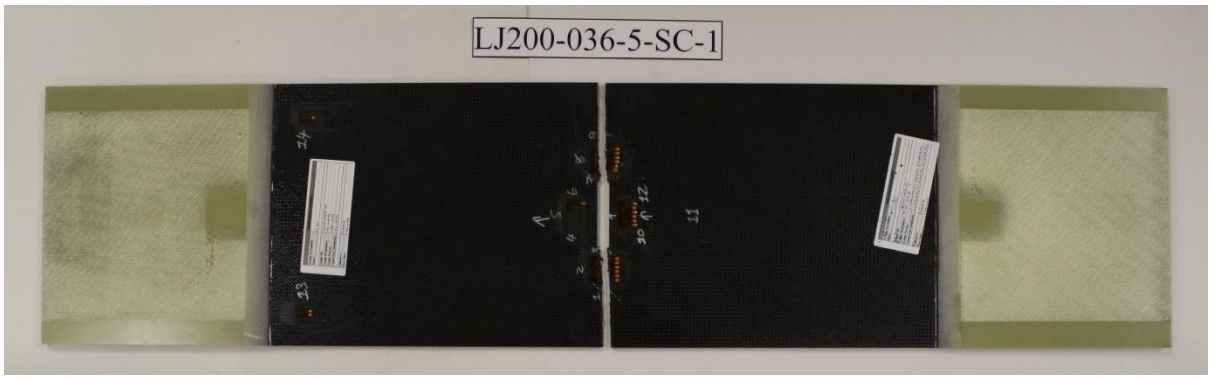

FRONT SIDE

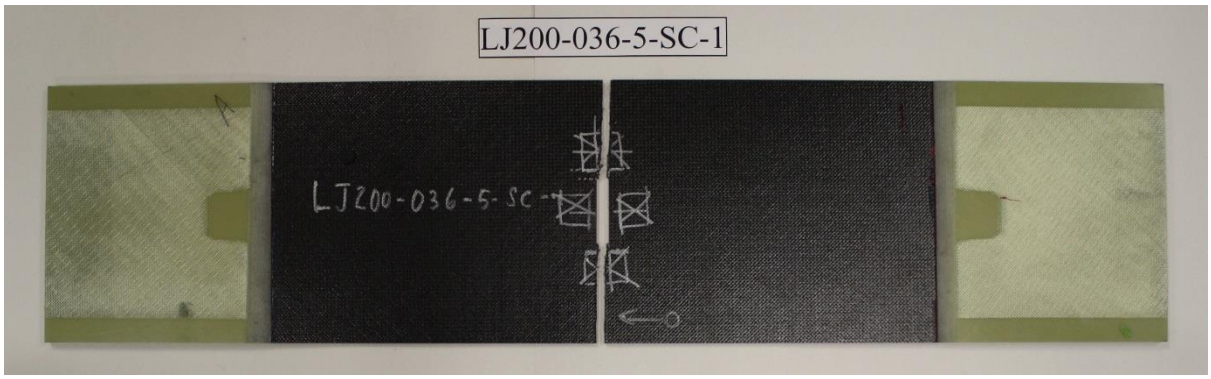

BACK SIDE

LJ200-036-5-SC-2

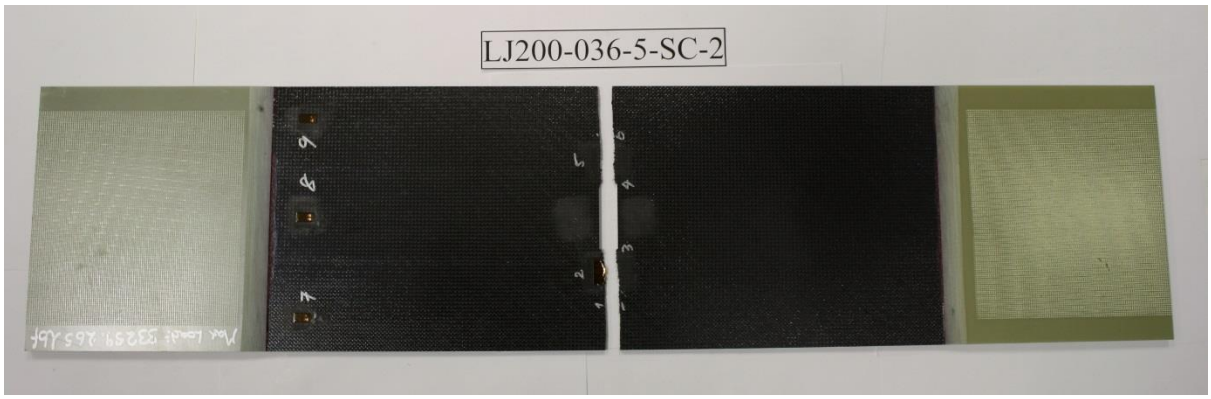

FRONT SIDE

BACK SIDE

LJ200-036-5-SC-3

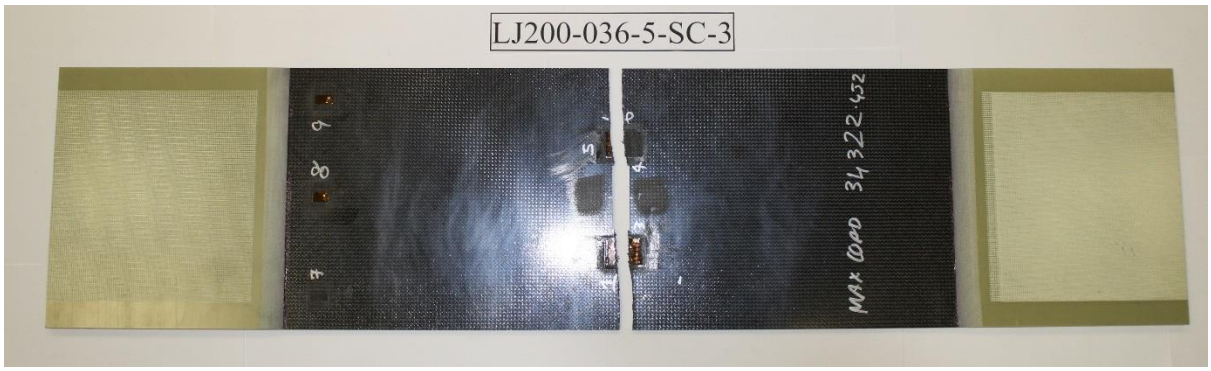

FRONT SIDE

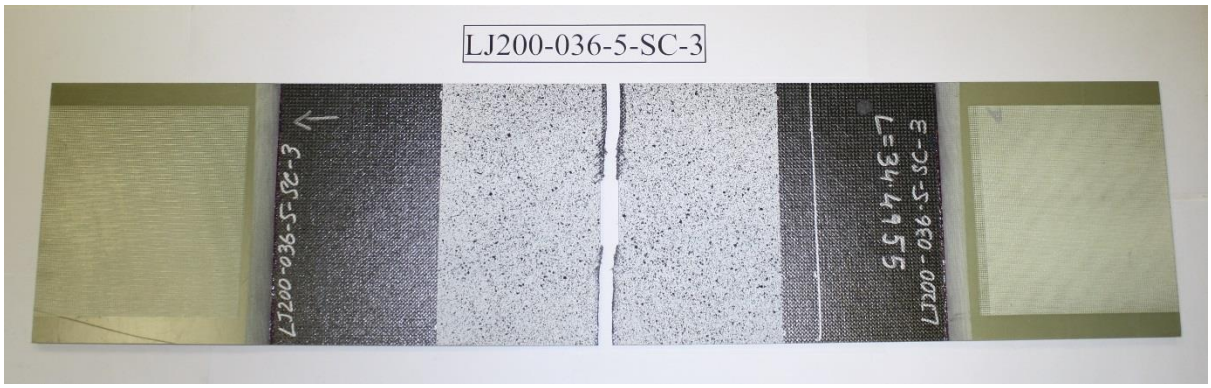

BACK SIDE

LJ200-036-6-SC-1

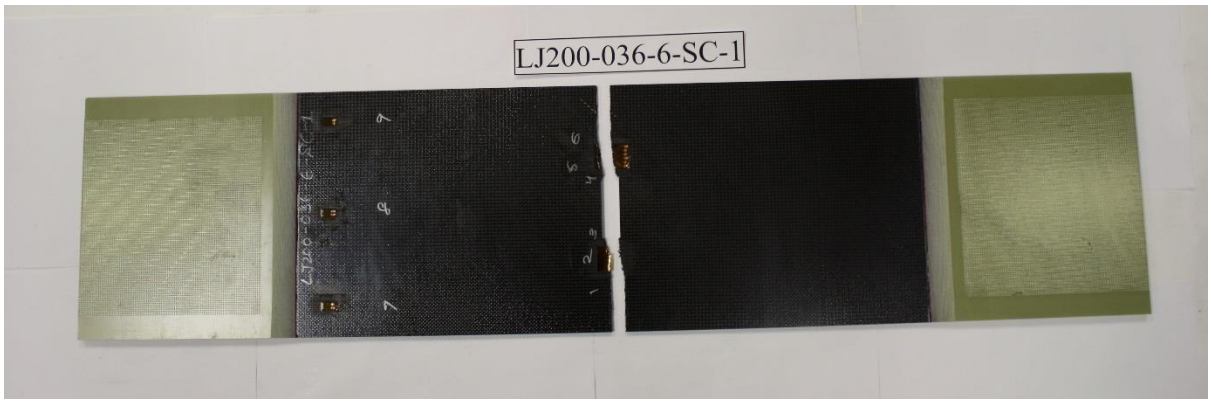

FRONT SIDE

BACK SIDE

LJ200-036-6-SC-2

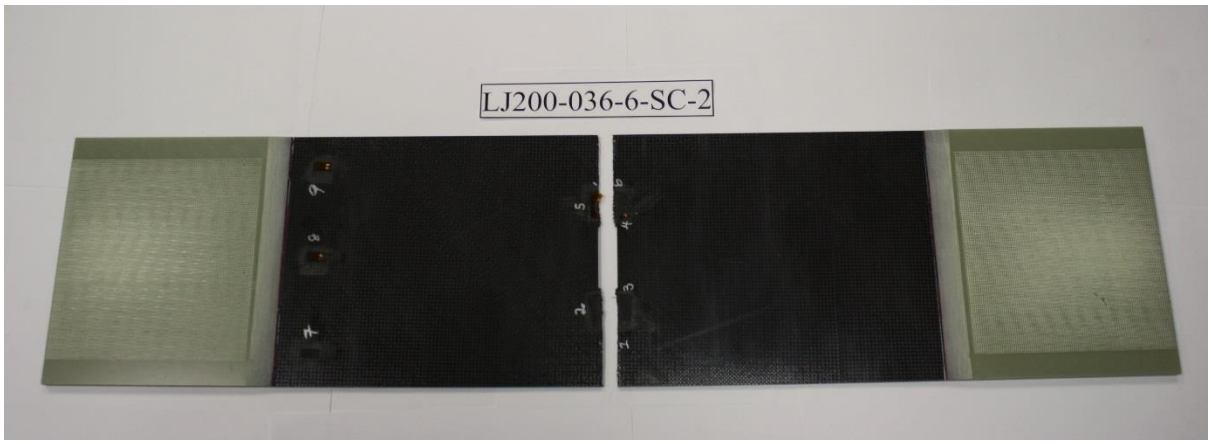

FRONT SIDE

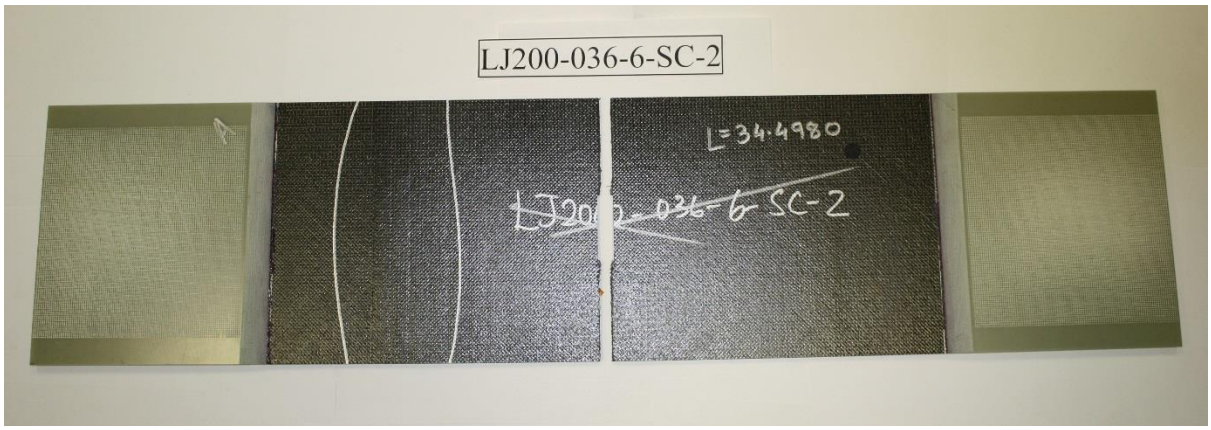

BACK SIDE

LJ200-036-6-SC-3

FRONT SIDE

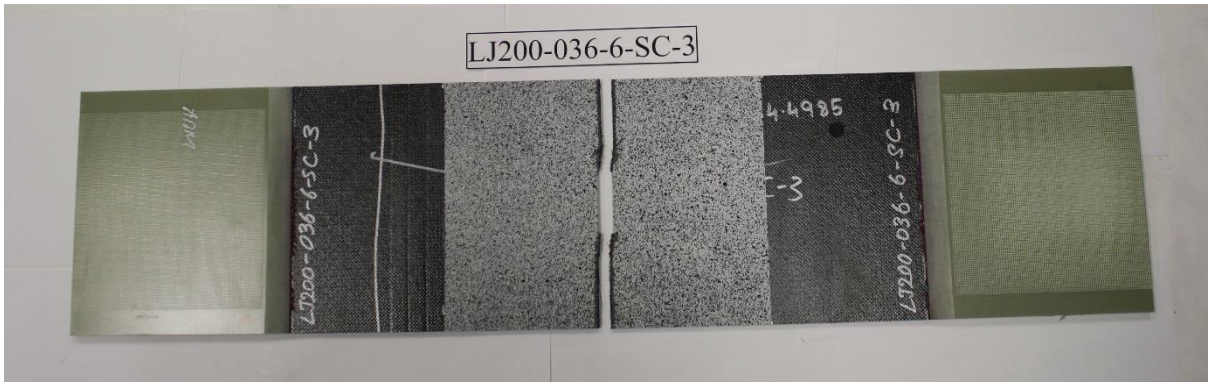

BACK SIDE

LJ200-036-7-SC-1

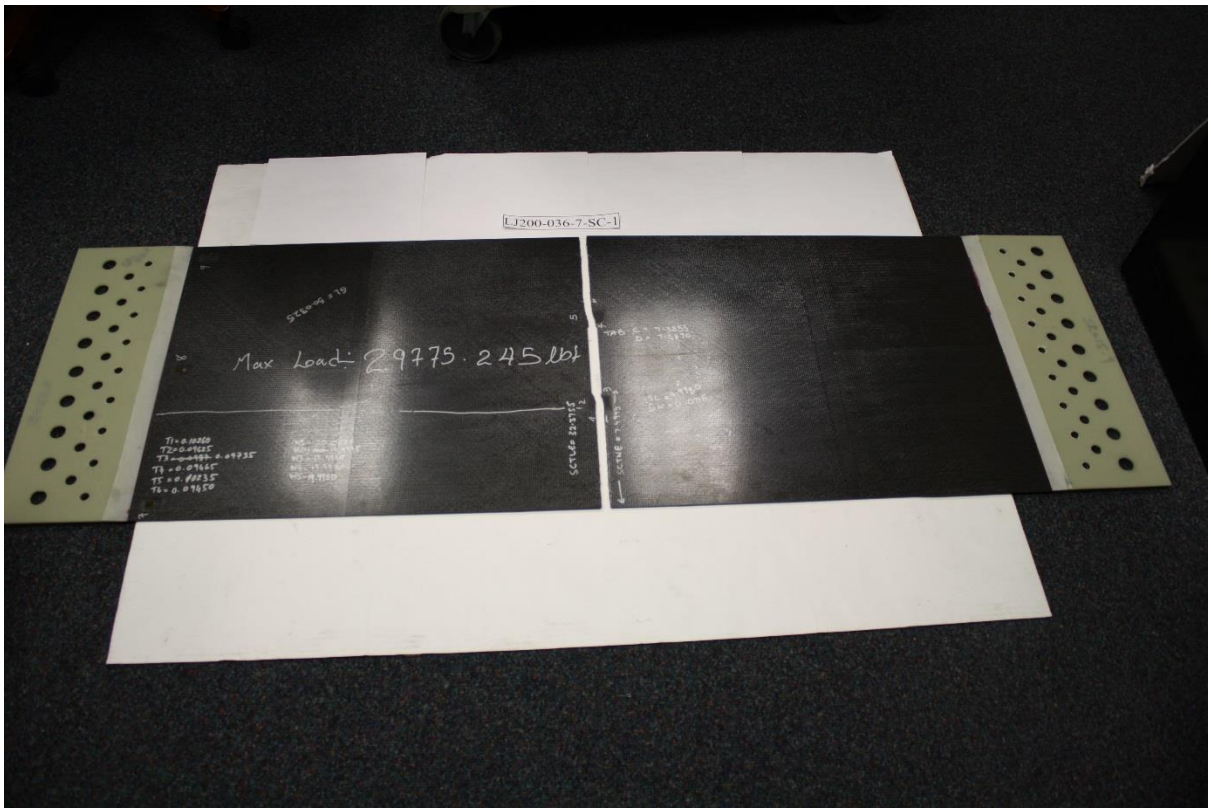

FORWARD SIDE

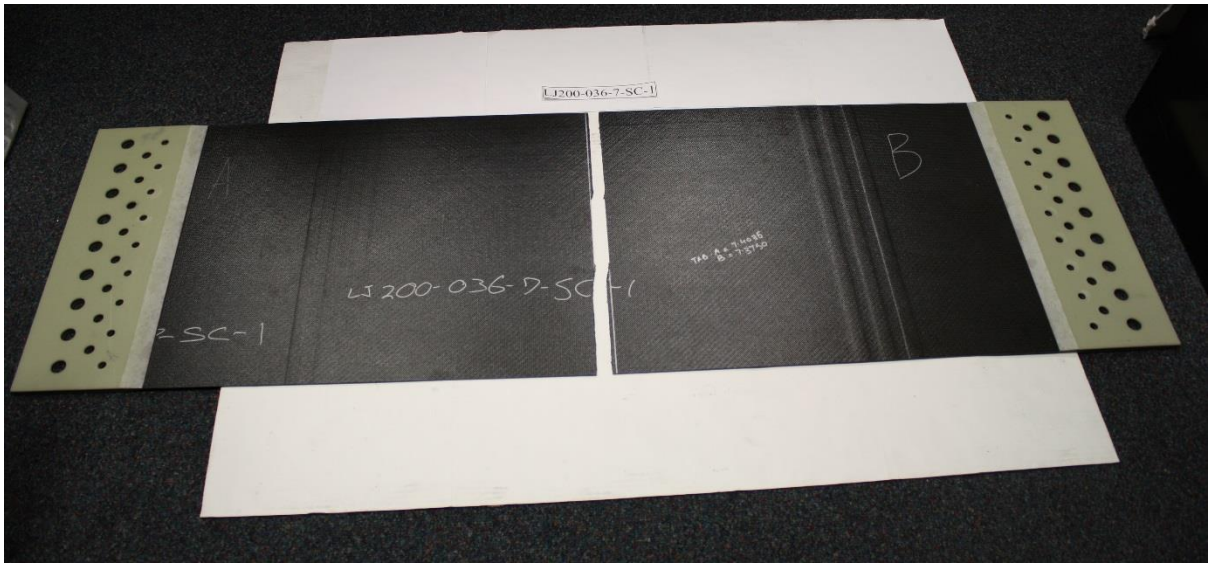

BACK SIDE

LJ200-036-8-SC-1

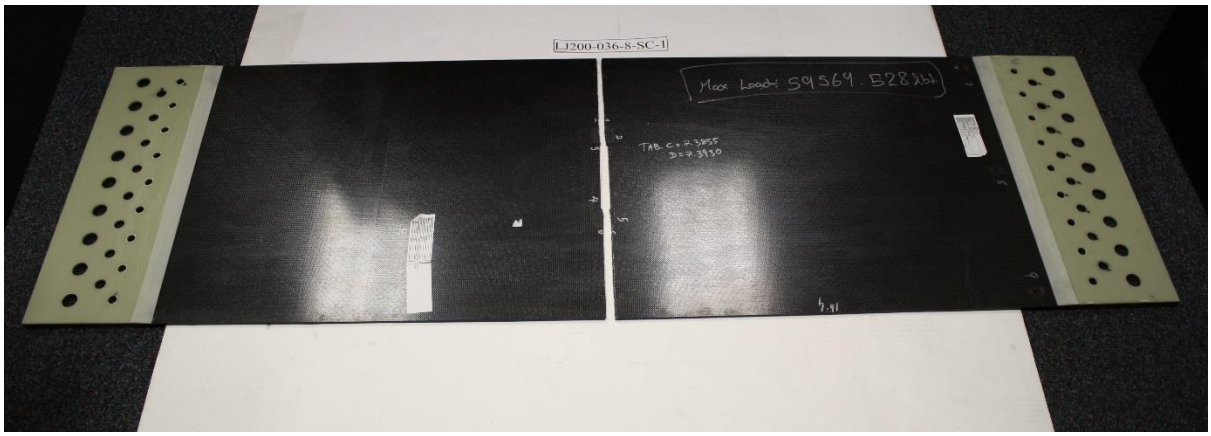

FRONT SIDE

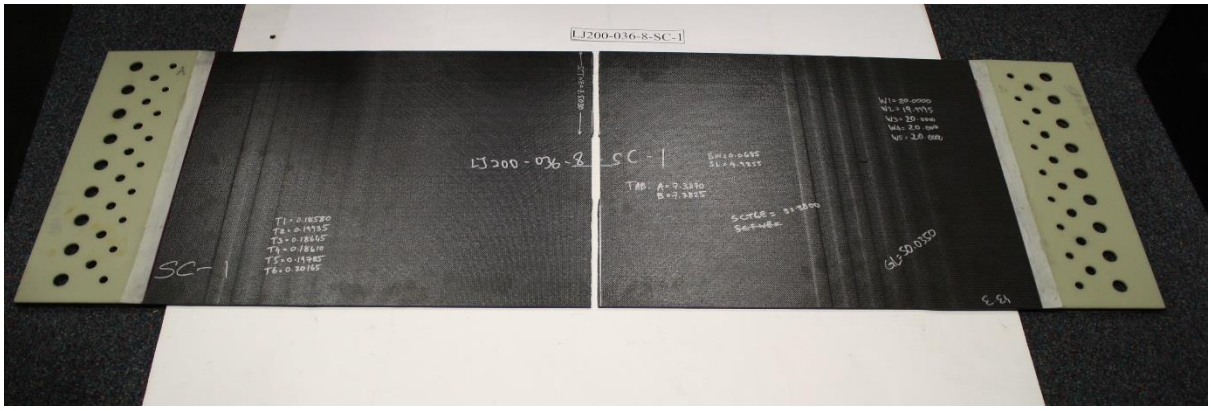

BACK SIDE

APPENDIX B

ARAMIS PHOTOGRAMMETRIC PHOTOS

LJ200-036-1-OH-2

Epsilon X:

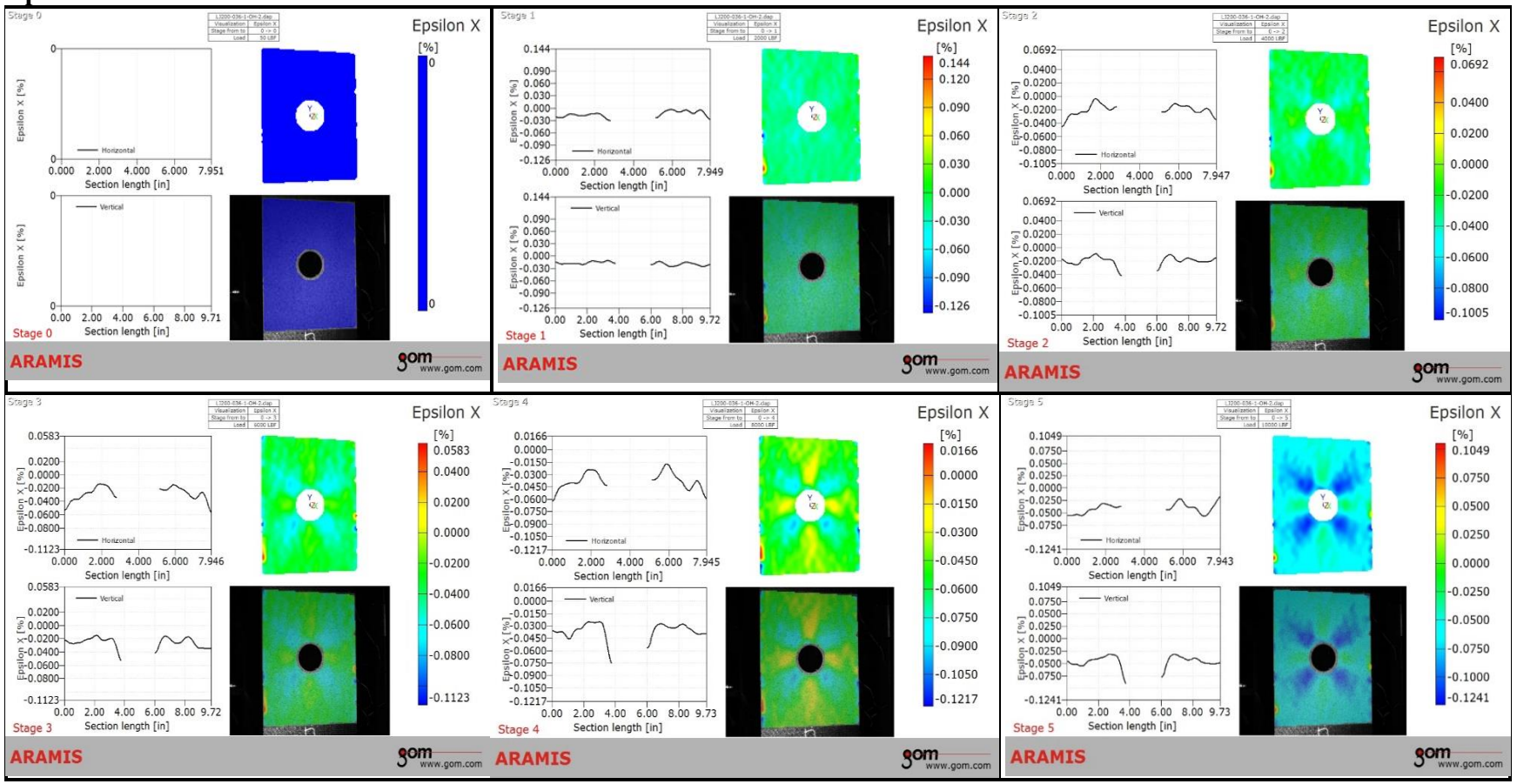

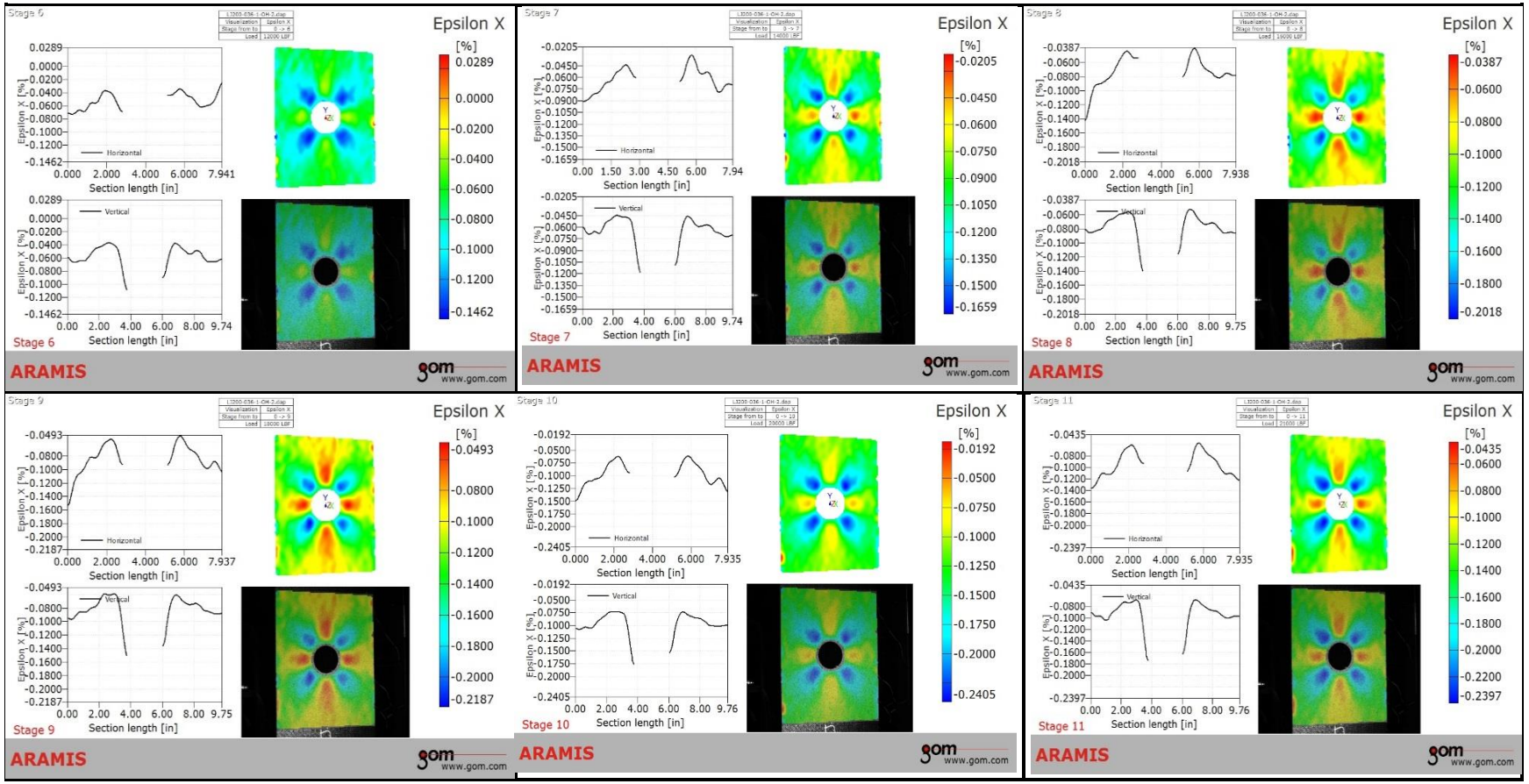
Stage 6
Epsilon X
[%]
0.0289
0.0000
-0.0200
-0.0400
-0.0600
-0.0800
-0.1000
-0.1200
-0.1462
Epsilon X [%]
Horizontal
Vertical
Section length [in]
0.000 2.000 4.000 6.000 7.941
0.000 2.000 4.000 6.000 8.000 9.74
Stage 6
ARAMIS
gom
www.gom.com
Stage 7
Epsilon X
[%]
-0.0205
-0.0450
-0.0600
-0.0750
-0.0900
-0.1050
-0.1200
-0.1350
-0.1500
-0.1659
Epsilon X [%]
Horizontal
Vertical
Section length [in]
0.00 1.50 3.00 4.50 6.00 7.94
0.00 2.00 4.00 6.00 8.00 9.74
Stage 7
ARAMIS
gom
www.gom.com
Stage 8
Epsilon X
[%]
-0.0387
-0.0600
-0.0800
-0.1000
-0.1200
-0.1400
-0.1600
-0.1800
-0.2018
Epsilon X [%]
Horizontal
Vertical
Section length [in]
0.000 2.000 4.000 6.000 7.938
0.000 2.000 4.000 6.000 8.000 9.75
Stage 8
ARAMIS
gom
www.gom.com
Stage 9
Epsilon X
[%]
-0.0493
-0.0800
-0.1000
-0.1200
-0.1400
-0.1600
-0.1800
-0.2000
-0.2187
Epsilon X [%]
Horizontal
Vertical
Section length [in]
0.000 2.000 4.000 6.000 7.937
0.000 2.000 4.000 6.000 8.000 9.75
Stage 9
ARAMIS
gom
www.gom.com
Stage 10
Epsilon X
[%]
-0.0192
-0.0500
-0.0750
-0.1000
-0.1250
-0.1500
-0.1750
-0.2000
-0.2405
Epsilon X [%]
Horizontal
Vertical
Section length [in]
0.000 2.000 4.000 6.000 7.935
0.000 2.000 4.000 6.000 8.000 9.76
Stage 10
ARAMIS
gom
www.gom.com
Stage 11
Epsilon X
[%]
-0.0435
-0.0600
-0.0800
-0.1000
-0.1200
-0.1400
-0.1600
-0.1800
-0.2000
-0.2200
-0.2397
Epsilon X [%]
Horizontal
Vertical
Section length [in]
0.000 2.000 4.000 6.000 7.935
0.000 2.000 4.000 6.000 8.000 9.76
Stage 11
ARAMIS
gom
www.gom.com

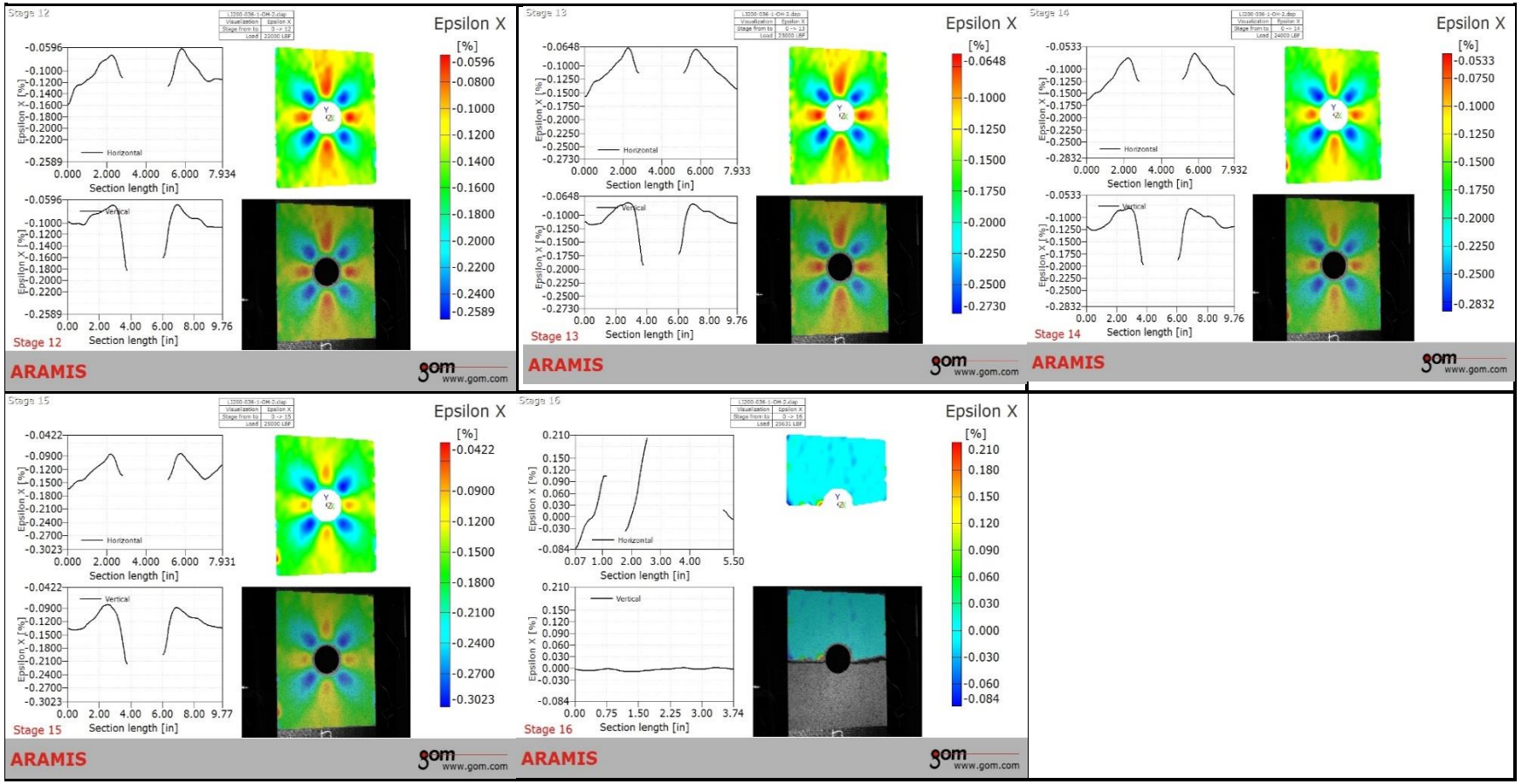
Stage 12
Epsilon X
[%]
-0.0596
-0.0800
-0.1000
-0.1200
-0.1400
-0.1600
-0.1800
-0.2000
-0.2200
-0.2400
-0.2589
Epsilon X [%]
Horizontal
Vertical
Section length [in]
0.000 2.000 4.000 6.000 7.934
0.00 2.00 4.00 6.00 8.00 9.76
Stage 12
ARAMIS
gom
www.gom.com
Stage 13
Epsilon X
[%]
-0.0648
-0.1000
-0.1250
-0.1500
-0.1750
-0.2000
-0.2250
-0.2500
-0.2730
Epsilon X [%]
Horizontal
Vertical
Section length [in]
0.000 2.000 4.000 6.000 7.933
0.00 2.00 4.00 6.00 8.00 9.76
Stage 13
ARAMIS
gom
www.gom.com
Stage 14
Epsilon X
[%]
-0.0533
-0.0750
-0.1000
-0.1250
-0.1500
-0.1750
-0.2000
-0.2250
-0.2500
-0.2832
Epsilon X [%]
Horizontal
Vertical
Section length [in]
0.000 2.000 4.000 6.000 7.932
0.00 2.00 4.00 6.00 8.00 9.76
Stage 14
ARAMIS
gom
www.gom.com
Stage 15
Epsilon X
[%]
-0.0422
-0.0900
-0.1200
-0.1500
-0.1800
-0.2100
-0.2400
-0.2700
-0.3023
Epsilon X [%]
Horizontal
Vertical
Section length [in]
0.000 2.000 4.000 6.000 7.931
0.00 2.00 4.00 6.00 8.00 9.77
Stage 15
ARAMIS
gom
www.gom.com
Stage 16
Epsilon X
[%]
0.210
0.180
0.150
0.120
0.090
0.060
0.030
0.000
-0.030
-0.060
-0.084
Epsilon X [%]
Horizontal
Vertical
Section length [in]
0.07 1.00 2.00 3.00 4.00 5.50
0.00 0.75 1.50 2.25 3.00 3.74
Stage 16
ARAMIS
gom
www.gom.com

Epsilon Y:

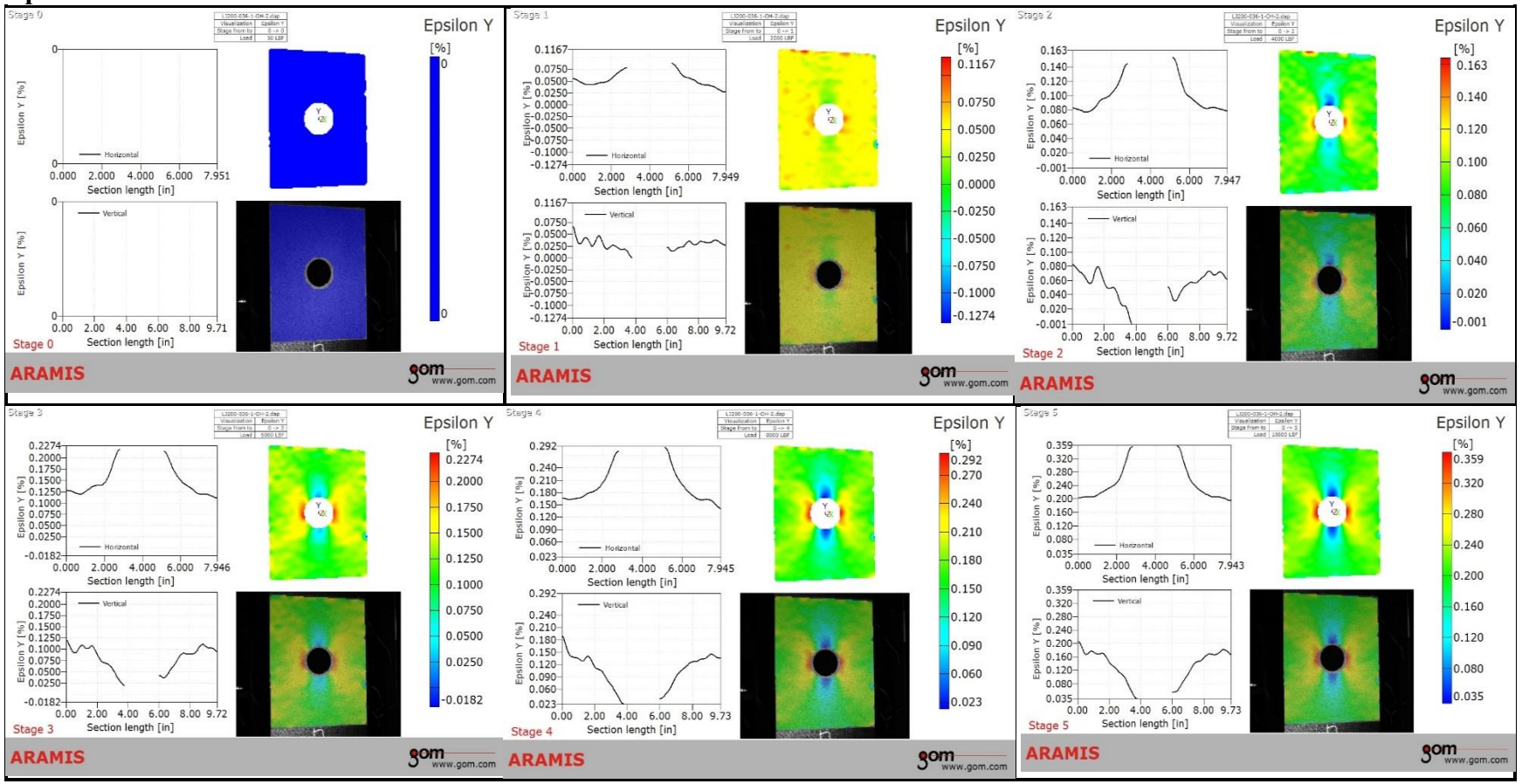
Stage 0
Epsilon Y
[%]
Horizontal
Vertical
Section length [in]
Stage 0
ARAMIS
Stage 1
Stage 1
ARAMIS
Stage 2
Stage 2
ARAMIS
Stage 3
Stage 3
ARAMIS
Stage 4
Stage 4
ARAMIS
Stage 5
Stage 5
ARAMIS
www.gom.com

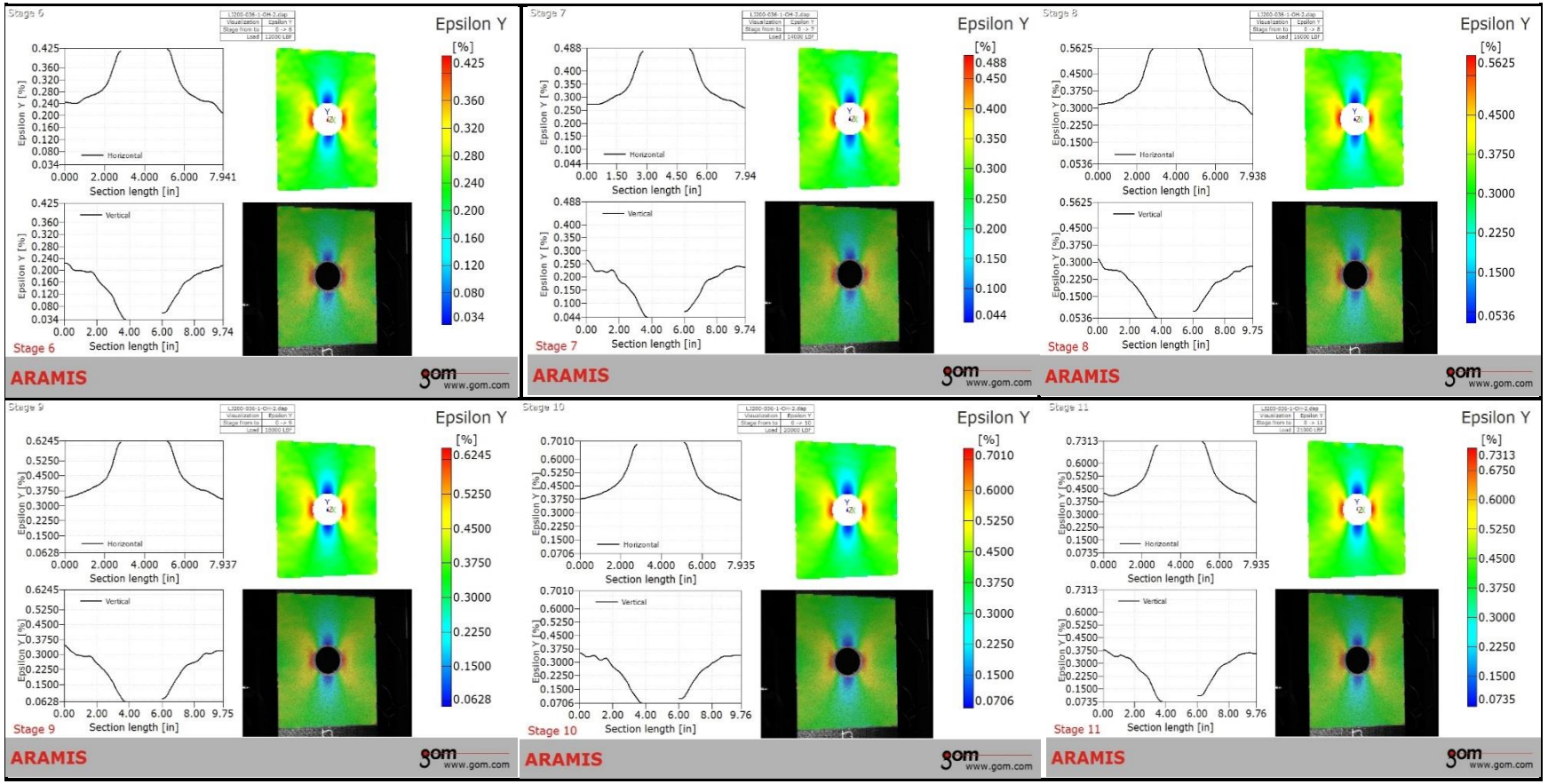
Stage 6
Epsilon Y
[%]
0.425
0.360
0.320
0.280
0.240
0.200
0.160
0.120
0.080
0.034
Epsilon Y [%]
Horizontal
Section length [in]
0.000 2.000 4.000 6.000 7.941
Vertical
0.00 2.00 4.00 6.00 8.00 9.74
Stage 6
ARAMIS
Stage 7
Epsilon Y
[%]
0.488
0.450
0.400
0.350
0.300
0.250
0.200
0.150
0.100
0.044
Horizontal
0.00 1.50 3.00 4.50 6.00 7.94
Vertical
0.00 2.00 4.00 6.00 8.00 9.74
Stage 7
ARAMIS
Stage 8
Epsilon Y
[%]
0.5625
0.4500
0.3750
0.3000
0.2250
0.1500
0.0536
Horizontal
0.000 2.000 4.000 6.000 7.938
Vertical
0.00 2.00 4.00 6.00 8.00 9.75
Stage 8
ARAMIS
Stage 9
Epsilon Y
[%]
0.6245
0.5250
0.4500
0.3750
0.3000
0.2250
0.1500
0.0628
Horizontal
0.000 2.000 4.000 6.000 7.937
Vertical
0.00 2.00 4.00 6.00 8.00 9.75
Stage 9
ARAMIS
Stage 10
Epsilon Y
[%]
0.7010
0.6000
0.5250
0.4500
0.3750
0.3000
0.2250
0.1500
0.0706
Horizontal
0.000 2.000 4.000 6.000 7.935
Vertical
0.00 2.00 4.00 6.00 8.00 9.76
Stage 10
ARAMIS
Stage 11
Epsilon Y
[%]
0.7313
0.6750
0.6000
0.5250
0.4500
0.3750
0.3000
0.2250
0.1500
0.0735
Horizontal
0.000 2.000 4.000 6.000 7.935
Vertical
0.00 2.00 4.00 6.00 8.00 9.76
Stage 11
ARAMIS
Section length [in]
www.gom.com

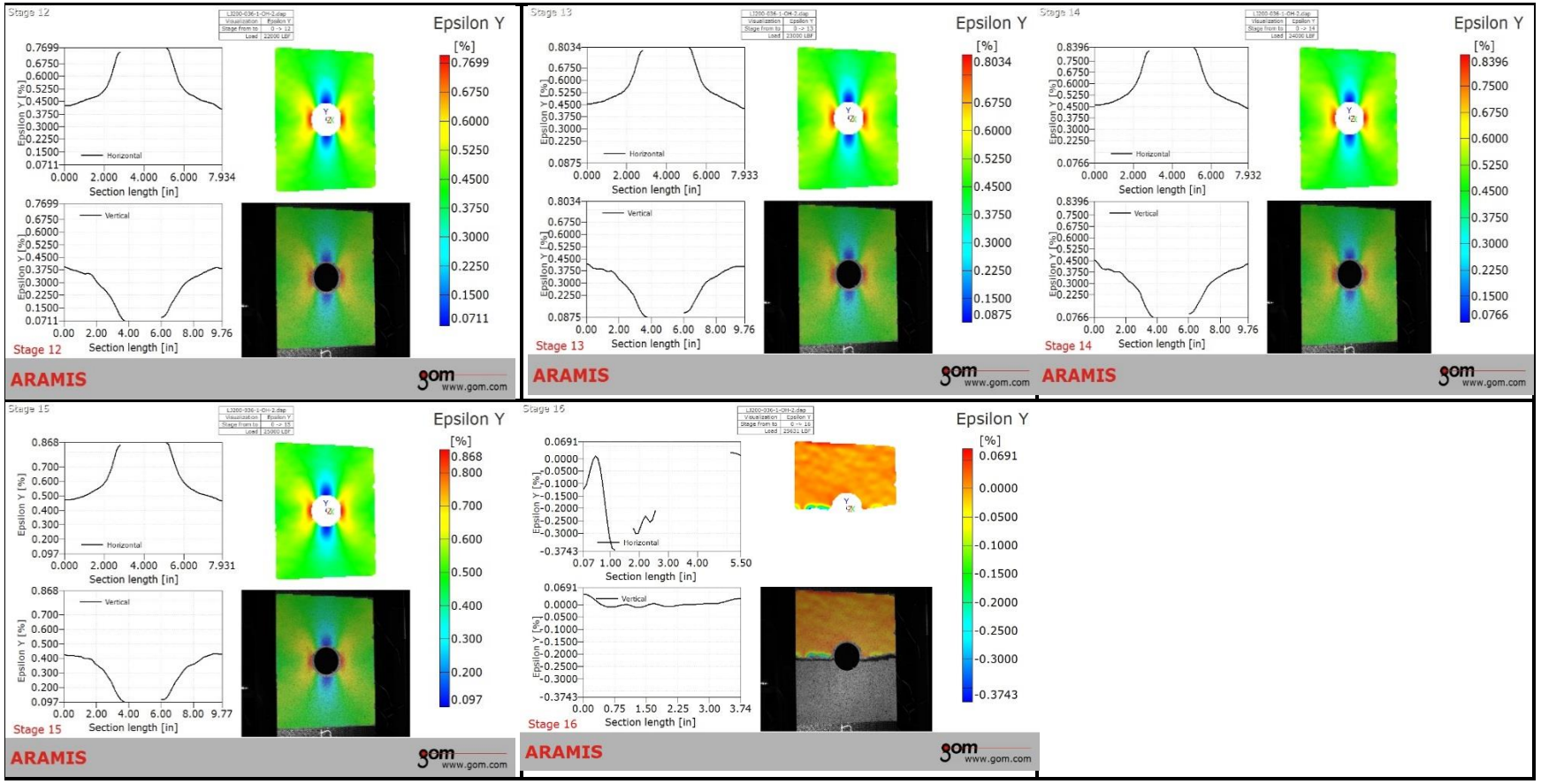
Stage 12
Epsilon Y
[%]
0.7699
0.6750
0.6000
0.5250
0.4500
0.3750
0.3000
0.2250
0.1500
0.0711
Epsilon Y [%]
Horizontal
Vertical
Section length [in]
0.000 2.000 4.000 6.000 7.934
0.00 2.00 4.00 6.00 8.00 9.76
Stage 12
ARAMIS
gom
www.gom.com
Stage 13
Epsilon Y
[%]
0.8034
0.6750
0.6000
0.5250
0.4500
0.3750
0.3000
0.2250
0.1500
0.0875
Epsilon Y [%]
Horizontal
Vertical
Section length [in]
0.000 2.000 4.000 6.000 7.933
0.00 2.00 4.00 6.00 8.00 9.76
Stage 13
ARAMIS
gom
www.gom.com
Stage 14
Epsilon Y
[%]
0.8396
0.7500
0.6750
0.6000
0.5250
0.4500
0.3750
0.3000
0.2250
0.1500
0.0766
Epsilon Y [%]
Horizontal
Vertical
Section length [in]
0.000 2.000 4.000 6.000 7.932
0.00 2.00 4.00 6.00 8.00 9.76
Stage 14
ARAMIS
gom
www.gom.com
Stage 15
Epsilon Y
[%]
0.868
0.800
0.700
0.600
0.500
0.400
0.300
0.200
0.097
Epsilon Y [%]
Horizontal
Vertical
Section length [in]
0.000 2.000 4.000 6.000 7.931
0.00 2.00 4.00 6.00 8.00 9.77
Stage 15
ARAMIS
gom
www.gom.com
Stage 16
Epsilon Y
[%]
0.0691
0.0000
-0.0500
-0.1000
-0.1500
-0.2000
-0.2500
-0.3000
-0.3743
Epsilon Y [%]
Horizontal
Vertical
Section length [in]
0.07 1.00 2.00 3.00 4.00 5.50
0.00 0.75 1.50 2.25 3.00 3.74
Stage 16
ARAMIS
gom
www.gom.com

LJ200-036-2-SC-1

Epsilon X:

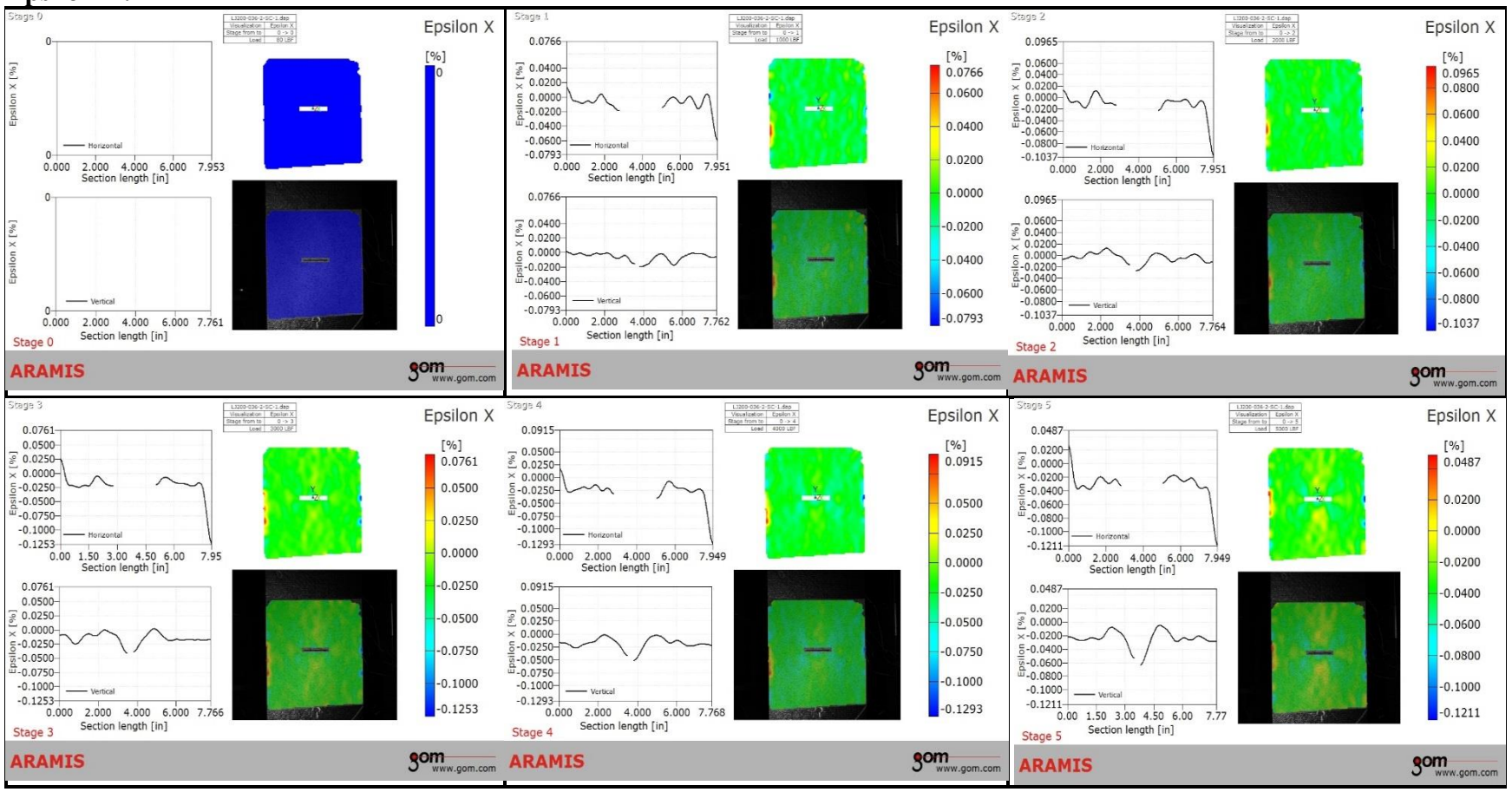

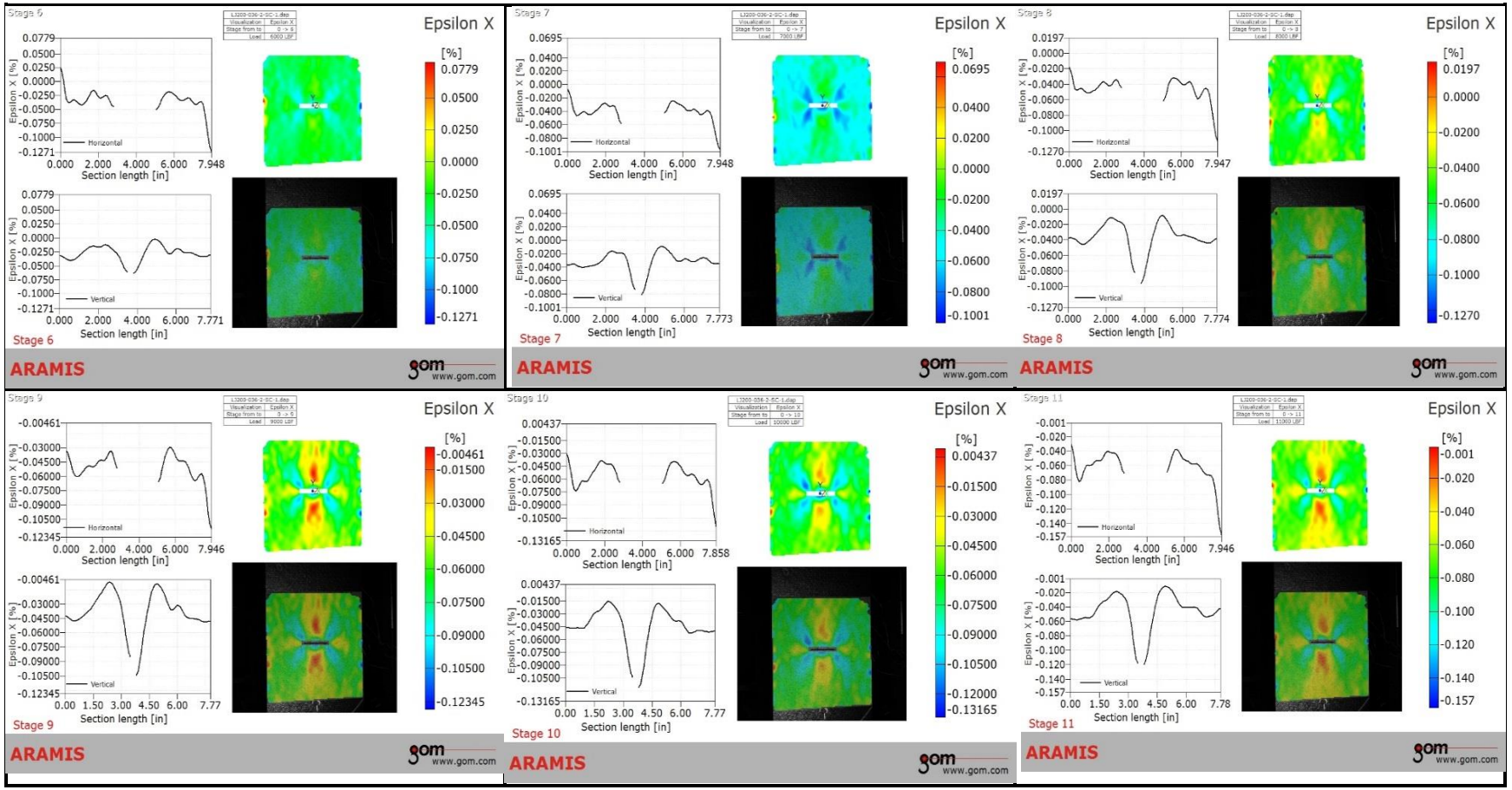
Stage 6
Epsilon X
[%]
0.0779
0.0500
0.0250
0.0000
-0.0250
-0.0500
-0.0750
-0.1000
-0.1271
Epsilon X [%]
Horizontal
Vertical
Section length [in]
0.000 2.000 4.000 6.000 7.948
0.000 2.000 4.000 6.000 7.771
Stage 6
ARAMIS
gom
www.gom.com
Stage 7
Epsilon X
[%]
0.0695
0.0400
0.0200
0.0000
-0.0200
-0.0400
-0.0600
-0.0800
-0.1001
Horizontal
Vertical
0.000 2.000 4.000 6.000 7.948
0.000 2.000 4.000 6.000 7.773
Stage 7
ARAMIS
gom
www.gom.com
Stage 8
Epsilon X
[%]
0.0197
0.0000
-0.0200
-0.0400
-0.0600
-0.0800
-0.1000
-0.1270
Horizontal
Vertical
0.000 2.000 4.000 6.000 7.947
0.000 2.000 4.000 6.000 7.774
Stage 8
ARAMIS
gom
www.gom.com
Stage 9
Epsilon X
[%]
-0.00461
-0.01500
-0.03000
-0.04500
-0.06000
-0.07500
-0.09000
-0.10500
-0.12345
Horizontal
Vertical
0.000 2.000 4.000 6.000 7.946
0.00 1.50 3.00 4.50 6.00 7.77
Stage 9
ARAMIS
gom
www.gom.com
Stage 10
Epsilon X
[%]
0.00437
-0.01500
-0.03000
-0.04500
-0.06000
-0.07500
-0.09000
-0.10500
-0.12000
-0.13165
Horizontal
Vertical
0.000 2.000 4.000 6.000 7.858
0.00 1.50 3.00 4.50 6.00 7.77
Stage 10
ARAMIS
gom
www.gom.com
Stage 11
Epsilon X
[%]
-0.001
-0.020
-0.040
-0.060
-0.080
-0.100
-0.120
-0.140
-0.157
Horizontal
Vertical
0.000 2.000 4.000 6.000 7.946
0.00 1.50 3.00 4.50 6.00 7.78
Stage 11
ARAMIS
gom
www.gom.com

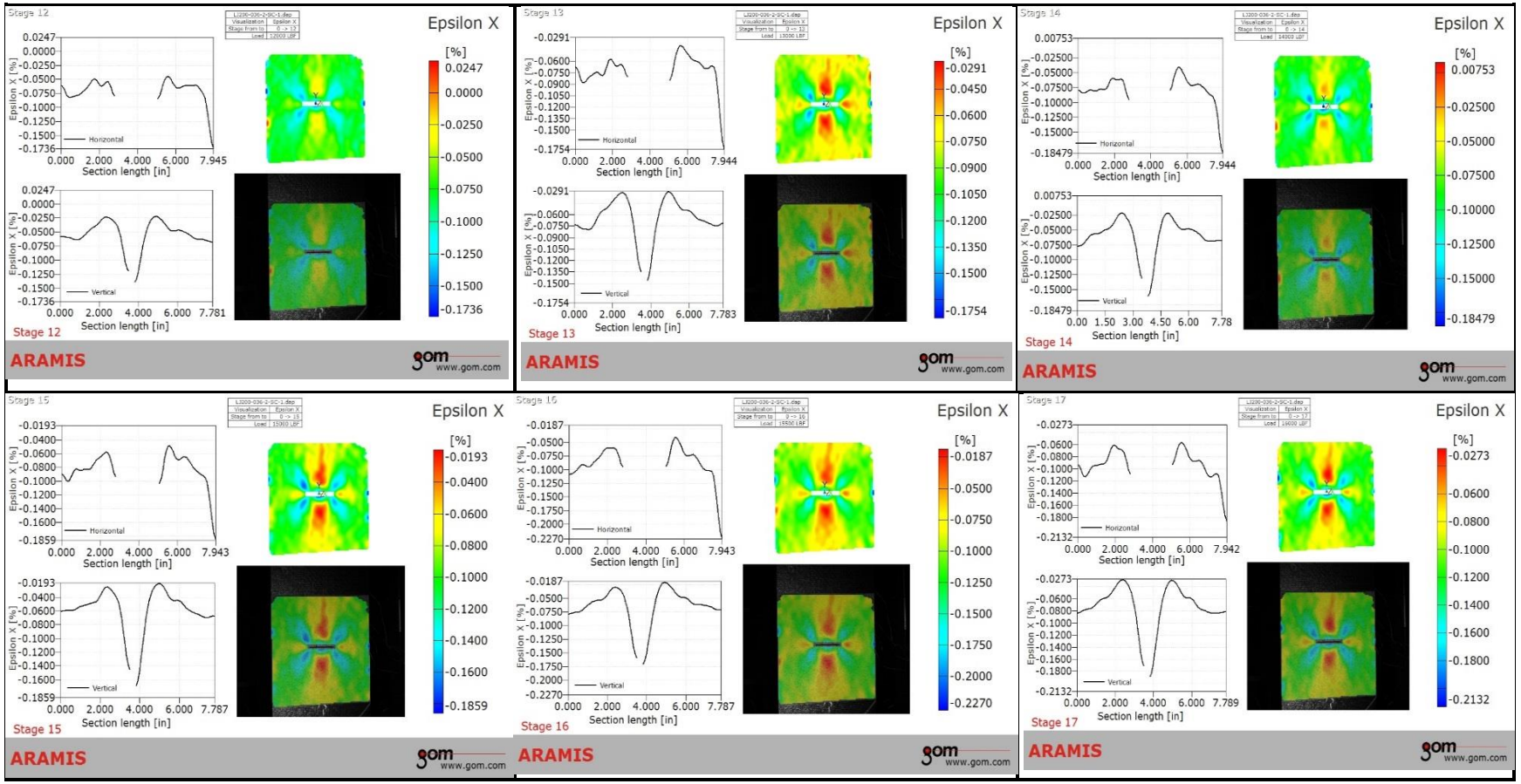
Stage 12
Epsilon X
[%]
0.0247
0.0000
-0.0250
-0.0500
-0.0750
-0.1000
-0.1250
-0.1500
-0.1736
Epsilon X [%]
Horizontal
Vertical
Section length [in]
0.000 2.000 4.000 6.000 7.945
0.000 2.000 4.000 6.000 7.781
Stage 12
ARAMIS
gom
www.gom.com
Stage 13
Epsilon X
[%]
-0.0291
-0.0450
-0.0600
-0.0750
-0.0900
-0.1050
-0.1200
-0.1350
-0.1500
-0.1754
Horizontal
Vertical
0.000 2.000 4.000 6.000 7.944
0.000 2.000 4.000 6.000 7.783
Stage 13
ARAMIS
gom
www.gom.com
Stage 14
Epsilon X
[%]
0.00753
-0.02500
-0.05000
-0.07500
-0.10000
-0.12500
-0.15000
-0.18479
Horizontal
Vertical
0.000 2.000 4.000 6.000 7.944
0.00 1.50 3.00 4.50 6.00 7.78
Stage 14
ARAMIS
gom
www.gom.com
Stage 15
Epsilon X
[%]
-0.0193
-0.0400
-0.0600
-0.0800
-0.1000
-0.1200
-0.1400
-0.1600
-0.1859
Horizontal
Vertical
0.000 2.000 4.000 6.000 7.943
0.000 2.000 4.000 6.000 7.787
Stage 15
ARAMIS
gom
www.gom.com
Stage 16
Epsilon X
[%]
-0.0187
-0.0500
-0.0750
-0.1000
-0.1250
-0.1500
-0.1750
-0.2000
-0.2270
Horizontal
Vertical
0.000 2.000 4.000 6.000 7.943
0.000 2.000 4.000 6.000 7.787
Stage 16
ARAMIS
gom
www.gom.com
Stage 17
Epsilon X
[%]
-0.0273
-0.0600
-0.0800
-0.1000
-0.1200
-0.1400
-0.1600
-0.1800
-0.2132
Horizontal
Vertical
0.000 2.000 4.000 6.000 7.942
0.000 2.000 4.000 6.000 7.789
Stage 17
ARAMIS
gom
www.gom.com

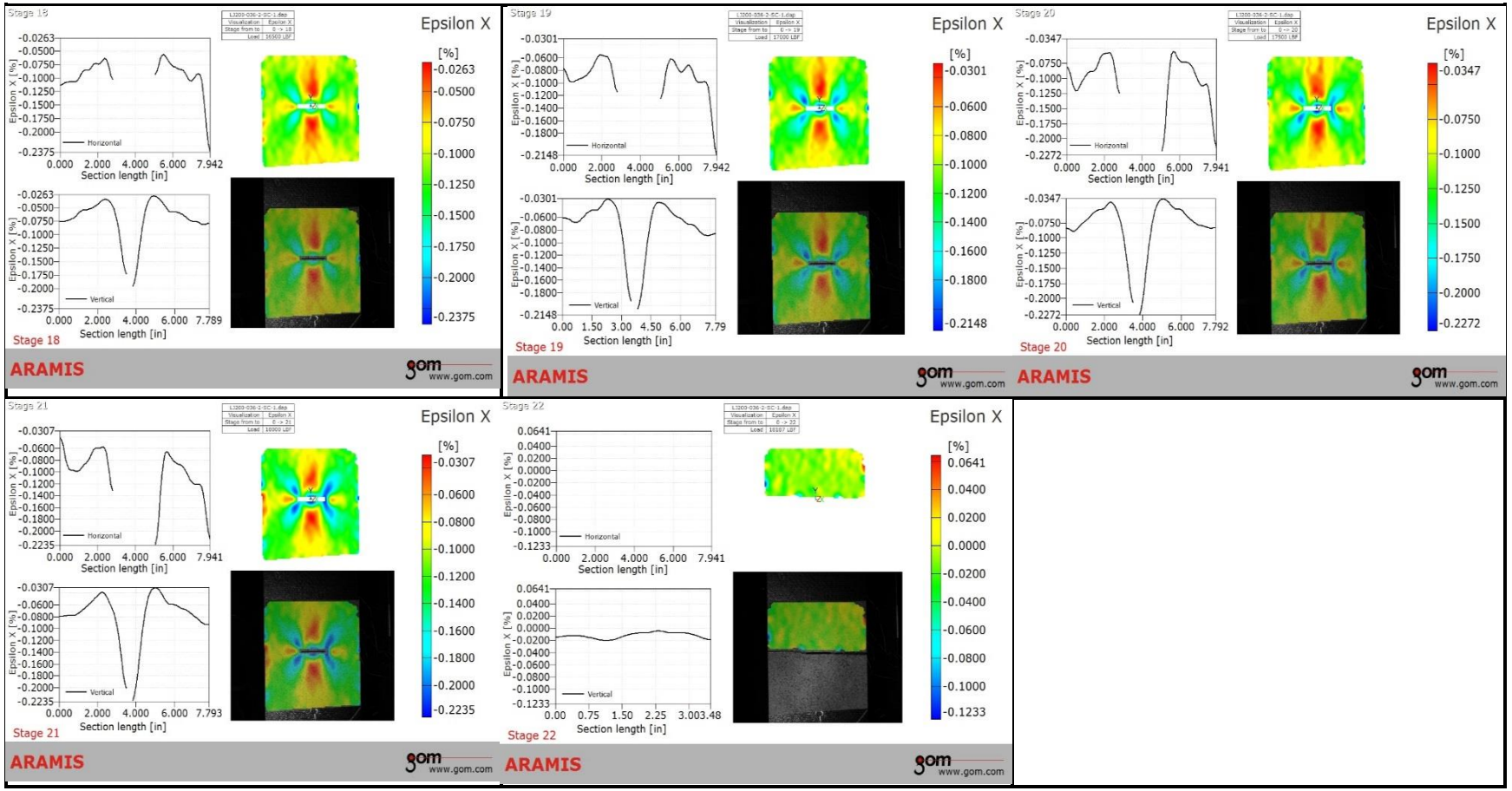
Stage 18
Epsilon X
[%]
Horizontal
Vertical
Section length [in]
ARAMIS
gom
www.gom.com
Stage 19
Epsilon X
[%]
Horizontal
Vertical
Section length [in]
ARAMIS
gom
www.gom.com
Stage 20
Epsilon X
[%]
Horizontal
Vertical
Section length [in]
ARAMIS
gom
www.gom.com
Stage 21
Epsilon X
[%]
Horizontal
Vertical
Section length [in]
ARAMIS
gom
www.gom.com
Stage 22
Epsilon X
[%]
Horizontal
Vertical
Section length [in]
ARAMIS
gom
www.gom.com

Epsilon Y:

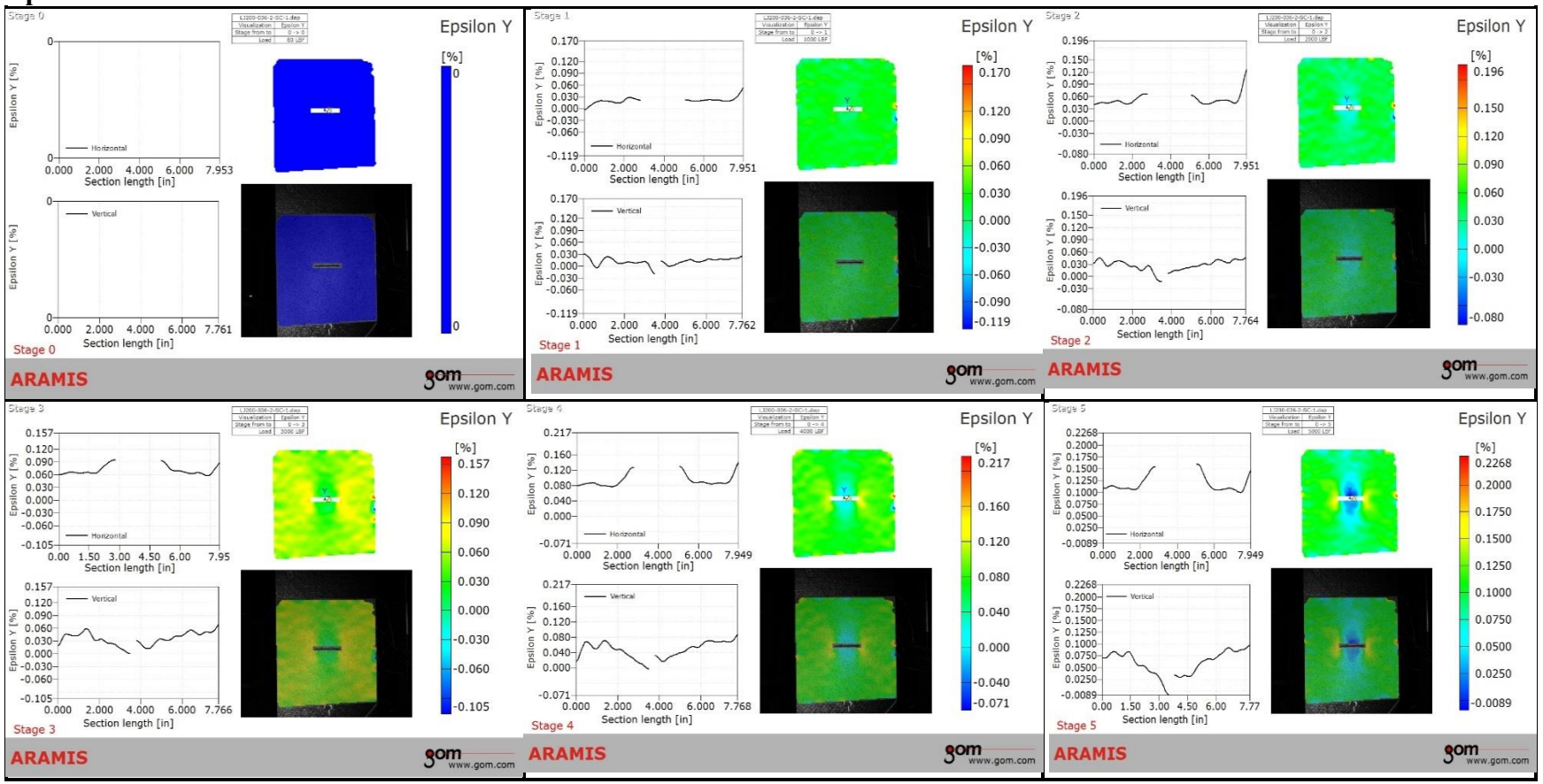
Stage 0
Epsilon Y
[%]
0
0
Epsilon Y [%]
Horizontal
Vertical
Section length [in]
0.000 2.000 4.000 6.000 7.953
0.000 2.000 4.000 6.000 7.761
Stage 0
ARAMIS
gom
www.gom.com
Stage 1
Epsilon Y
[%]
0.170
0.120
0.090
0.060
0.030
0.000
-0.030
-0.060
-0.090
-0.119
Epsilon Y [%]
Horizontal
Vertical
Section length [in]
0.000 2.000 4.000 6.000 7.951
0.000 2.000 4.000 6.000 7.762
Stage 1
ARAMIS
gom
www.gom.com
Stage 2
Epsilon Y
[%]
0.196
0.150
0.120
0.090
0.060
0.030
0.000
-0.030
-0.080
Epsilon Y [%]
Horizontal
Vertical
Section length [in]
0.000 2.000 4.000 6.000 7.951
0.000 2.000 4.000 6.000 7.764
Stage 2
ARAMIS
gom
www.gom.com
Stage 3
Epsilon Y
[%]
0.157
0.120
0.090
0.060
0.030
0.000
-0.030
-0.060
-0.105
Epsilon Y [%]
Horizontal
Vertical
Section length [in]
0.00 1.50 3.00 4.50 6.00 7.95
0.000 2.000 4.000 6.000 7.766
Stage 3
ARAMIS
gom
www.gom.com
Stage 4
Epsilon Y
[%]
0.217
0.160
0.120
0.080
0.040
0.000
-0.040
-0.071
Epsilon Y [%]
Horizontal
Vertical
Section length [in]
0.000 2.000 4.000 6.000 7.949
0.000 2.000 4.000 6.000 7.768
Stage 4
ARAMIS
gom
www.gom.com
Stage 5
Epsilon Y
[%]
0.2268
0.2000
0.1750
0.1500
0.1250
0.1000
0.0750
0.0500
0.0250
-0.0089
Epsilon Y [%]
Horizontal
Vertical
Section length [in]
0.000 2.000 4.000 6.000 7.949
0.00 1.50 3.00 4.50 6.00 7.77
Stage 5
ARAMIS
gom
www.gom.com

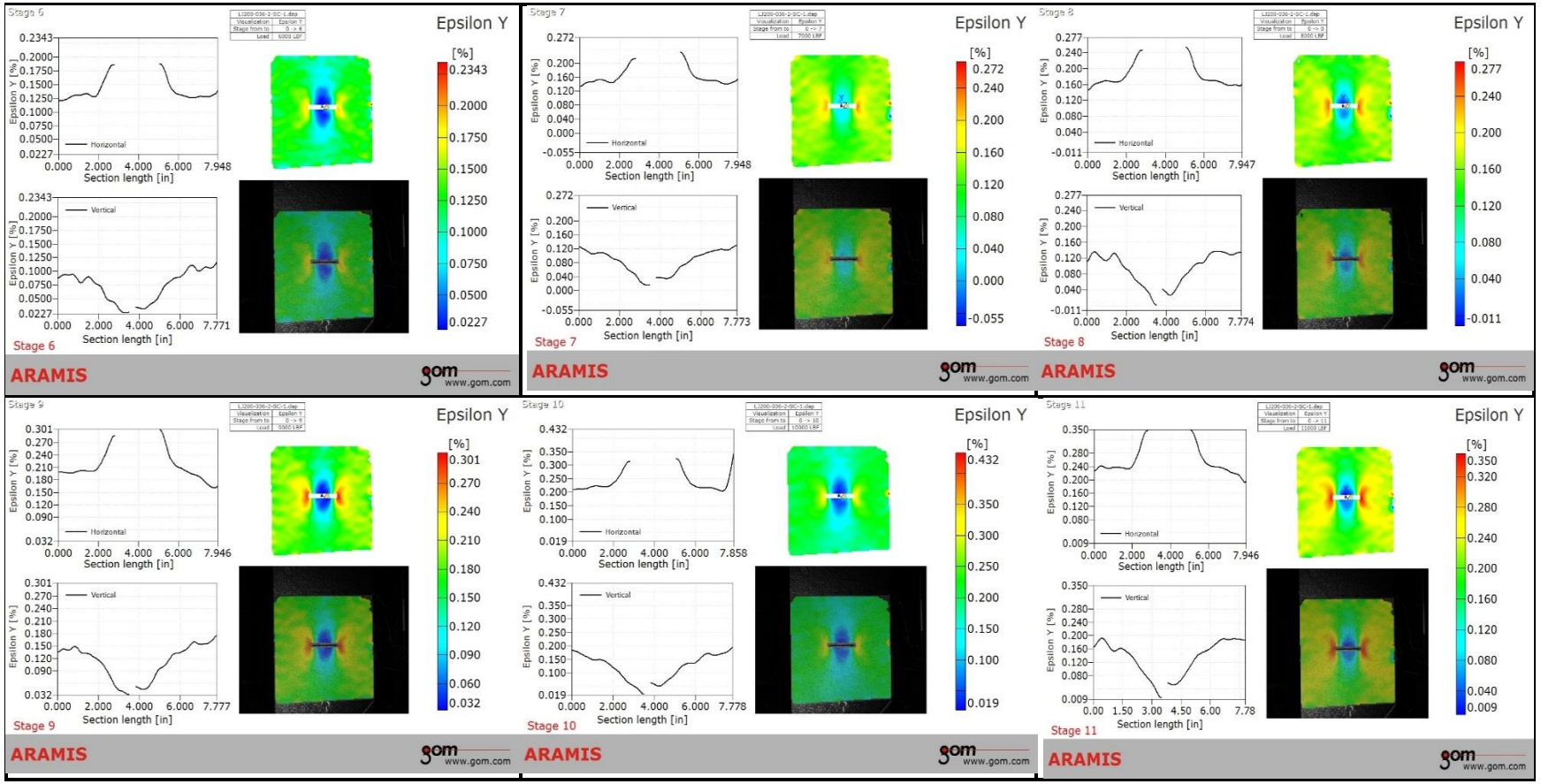
Stage 6
Epsilon Y
[%]
Horizontal
Vertical
Section length [in]
Stage 6
ARAMIS
Stage 7
Epsilon Y
[%]
Horizontal
Vertical
Section length [in]
Stage 7
ARAMIS
Stage 8
Epsilon Y
[%]
Horizontal
Vertical
Section length [in]
Stage 8
ARAMIS
Stage 9
Epsilon Y
[%]
Horizontal
Vertical
Section length [in]
Stage 9
ARAMIS
Stage 10
Epsilon Y
[%]
Horizontal
Vertical
Section length [in]
Stage 10
ARAMIS
Stage 11
Epsilon Y
[%]
Horizontal
Vertical
Section length [in]
Stage 11
ARAMIS

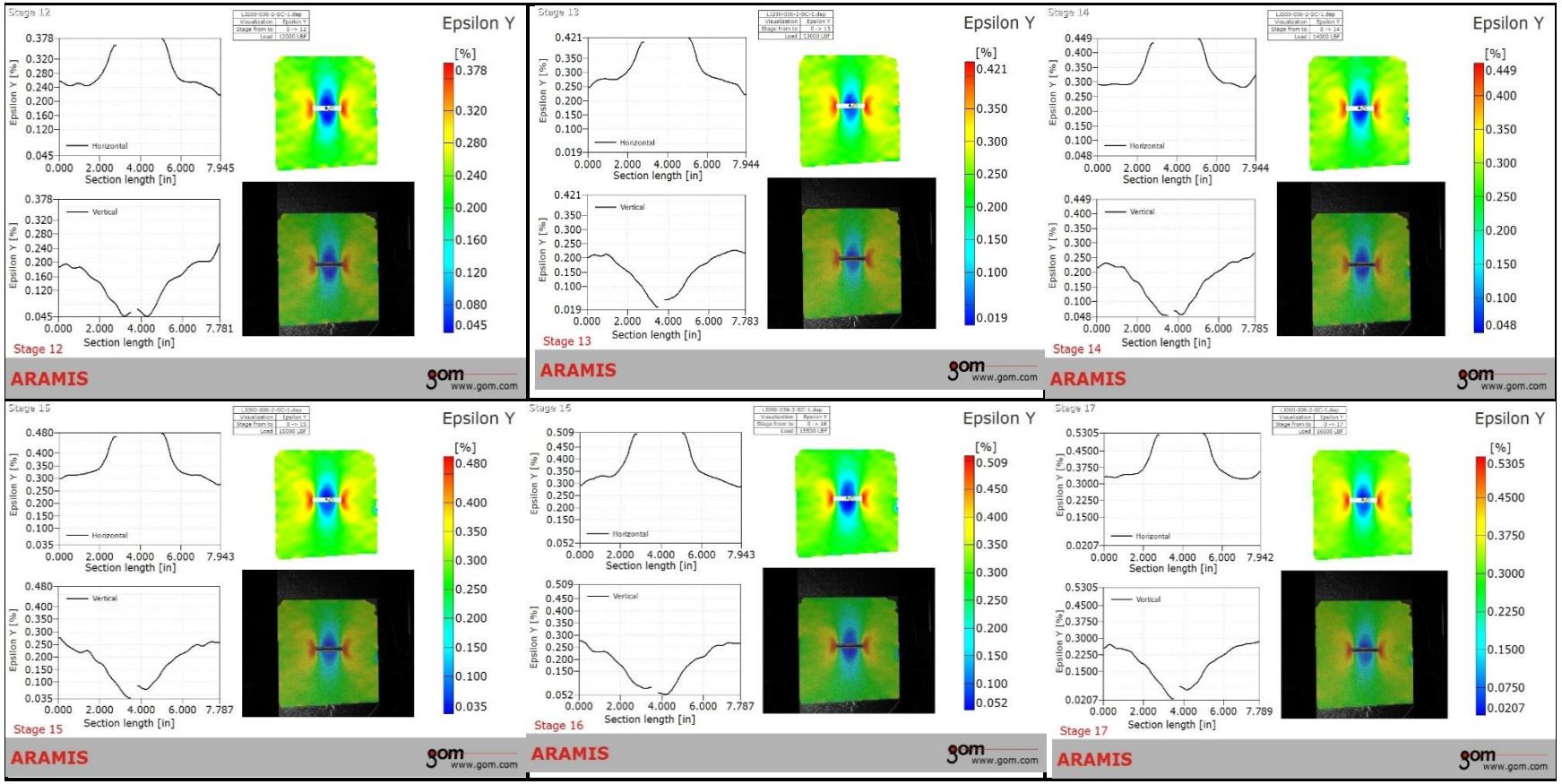
Stage 12
Epsilon Y
[%]
0.378
0.320
0.280
0.240
0.200
0.160
0.120
0.080
0.045
Epsilon Y [%]
Horizontal
Vertical
Section length [in]
0.000 2.000 4.000 6.000 7.945
0.000 2.000 4.000 6.000 7.781
Stage 12
ARAMIS
gom
www.gom.com
Stage 13
Epsilon Y
[%]
0.421
0.350
0.300
0.250
0.200
0.150
0.100
0.019
Horizontal
Vertical
0.000 2.000 4.000 6.000 7.944
0.000 2.000 4.000 6.000 7.783
Stage 13
ARAMIS
Stage 14
Epsilon Y
[%]
0.449
0.400
0.350
0.300
0.250
0.200
0.150
0.100
0.048
Horizontal
Vertical
0.000 2.000 4.000 6.000 7.944
0.000 2.000 4.000 6.000 7.785
Stage 14
ARAMIS
Stage 15
Epsilon Y
[%]
0.480
0.400
0.350
0.300
0.250
0.200
0.150
0.100
0.035
Horizontal
Vertical
0.000 2.000 4.000 6.000 7.943
0.000 2.000 4.000 6.000 7.787
Stage 15
ARAMIS
Stage 16
Epsilon Y
[%]
0.509
0.450
0.400
0.350
0.300
0.250
0.200
0.150
0.100
0.052
Horizontal
Vertical
0.000 2.000 4.000 6.000 7.943
0.000 2.000 4.000 6.000 7.787
Stage 16
ARAMIS
Stage 17
Epsilon Y
[%]
0.5305
0.4500
0.3750
0.3000
0.2250
0.1500
0.0750
0.0207
Horizontal
Vertical
0.000 2.000 4.000 6.000 7.942
0.000 2.000 4.000 6.000 7.789
Stage 17
ARAMIS

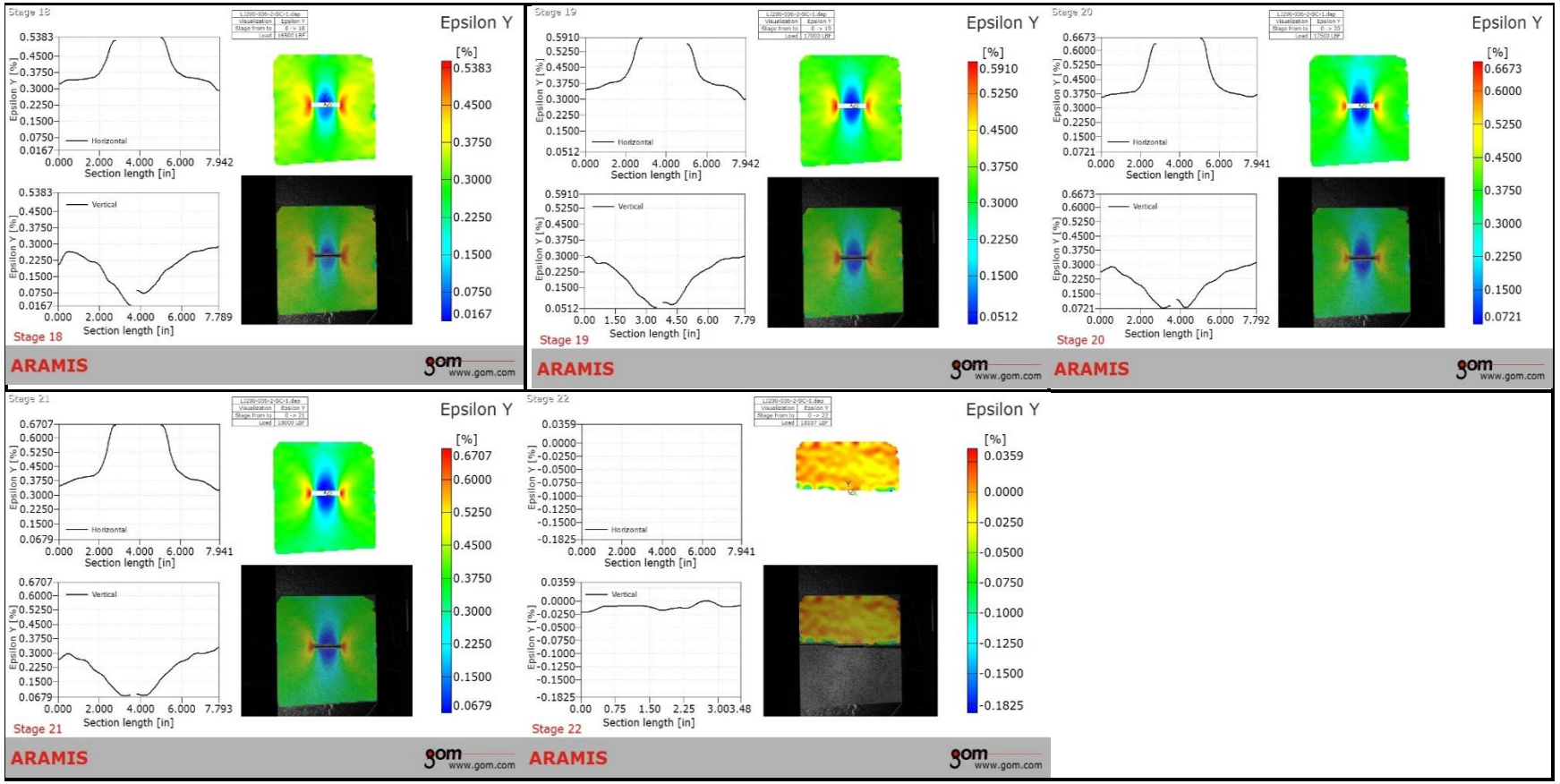
Stage 18
Epsilon Y
[%]
0.5383
0.4500
0.3750
0.3000
0.2250
0.1500
0.0750
0.0167
Epsilon Y [%]
Horizontal
Section length [in]
0.000 2.000 4.000 6.000 7.942
Vertical
0.000 2.000 4.000 6.000 7.789
Stage 18
ARAMIS
gom
www.gom.com
Stage 19
Epsilon Y
[%]
0.5910
0.5250
0.4500
0.3750
0.3000
0.2250
0.1500
0.0512
Horizontal
0.000 2.000 4.000 6.000 7.942
Vertical
0.00 1.50 3.00 4.50 6.00 7.79
Stage 19
ARAMIS
Stage 20
Epsilon Y
[%]
0.6673
0.6000
0.5250
0.4500
0.3750
0.3000
0.2250
0.1500
0.0721
Horizontal
0.000 2.000 4.000 6.000 7.941
Vertical
0.000 2.000 4.000 6.000 7.792
Stage 20
ARAMIS
Stage 21
Epsilon Y
[%]
0.6707
0.6000
0.5250
0.4500
0.3750
0.3000
0.2250
0.1500
0.0679
Horizontal
0.000 2.000 4.000 6.000 7.941
Vertical
0.000 2.000 4.000 6.000 7.793
Stage 21
ARAMIS
Stage 22
Epsilon Y
[%]
0.0359
0.0000
-0.0250
-0.0500
-0.0750
-0.1000
-0.1250
-0.1500
-0.1825
Horizontal
0.000 2.000 4.000 6.000 7.941
Vertical
0.00 0.75 1.50 2.25 3.003.48
Stage 22
ARAMIS

LJ200-036-5-SC-2

Epsilon X:

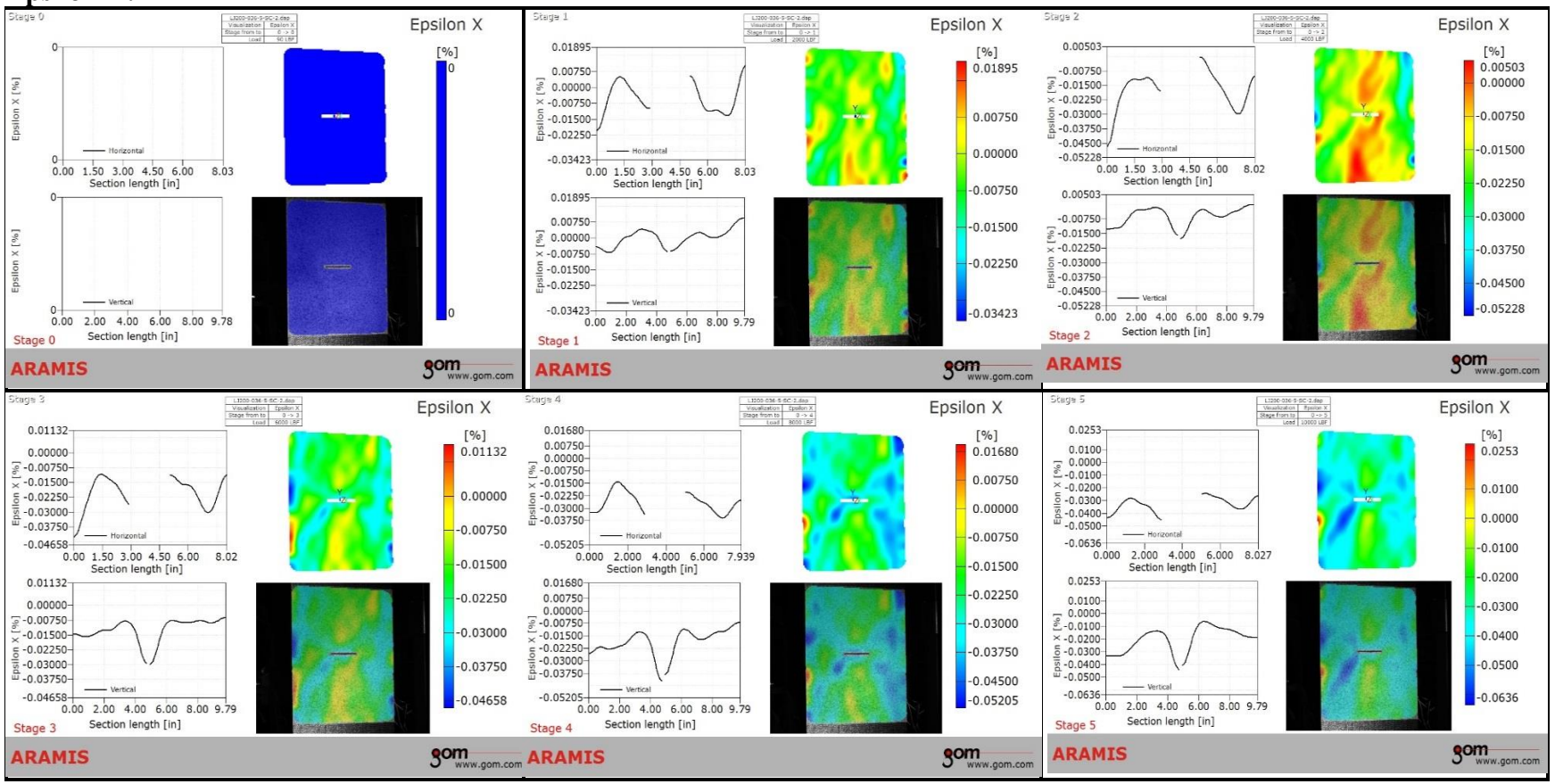

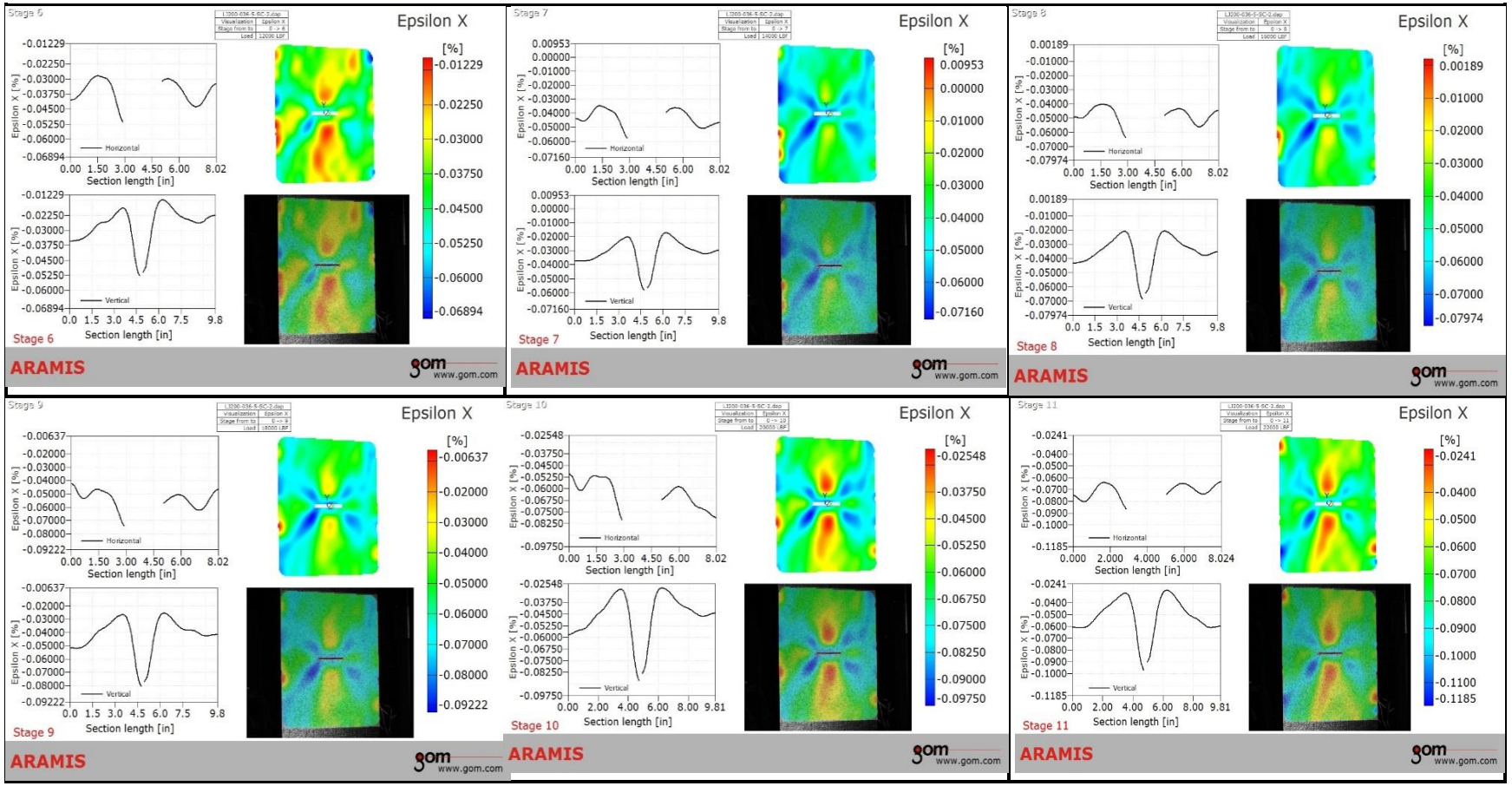
Stage 6
Epsilon X
[%]
-0.01229
-0.02250
-0.03000
-0.03750
-0.04500
-0.05250
-0.06000
-0.06894
Epsilon X [%]
Horizontal
Vertical
Section length [in]
0.00 1.50 3.00 4.50 6.00 8.02
0.0 1.5 3.0 4.5 6.0 7.5 9.8
Stage 6
ARAMIS
gom
www.gom.com
Stage 7
Epsilon X
[%]
0.00953
0.00000
-0.01000
-0.02000
-0.03000
-0.04000
-0.05000
-0.06000
-0.07160
Epsilon X [%]
Horizontal
Vertical
Section length [in]
0.00 1.50 3.00 4.50 6.00 8.02
0.0 1.5 3.0 4.5 6.0 7.5 9.8
Stage 7
ARAMIS
gom
www.gom.com
Stage 8
Epsilon X
[%]
0.00189
-0.01000
-0.02000
-0.03000
-0.04000
-0.05000
-0.06000
-0.07000
-0.07974
Epsilon X [%]
Horizontal
Vertical
Section length [in]
0.00 1.50 3.00 4.50 6.00 8.02
0.0 1.5 3.0 4.5 6.0 7.5 9.8
Stage 8
ARAMIS
gom
www.gom.com
Stage 9
Epsilon X
[%]
-0.00637
-0.02000
-0.03000
-0.04000
-0.05000
-0.06000
-0.07000
-0.08000
-0.09222
Epsilon X [%]
Horizontal
Vertical
Section length [in]
0.00 1.50 3.00 4.50 6.00 8.02
0.0 1.5 3.0 4.5 6.0 7.5 9.8
Stage 9
ARAMIS
gom
www.gom.com
Stage 10
Epsilon X
[%]
-0.02548
-0.03750
-0.04500
-0.05250
-0.06000
-0.06750
-0.07500
-0.08250
-0.09750
Epsilon X [%]
Horizontal
Vertical
Section length [in]
0.00 1.50 3.00 4.50 6.00 8.02
0.00 2.00 4.00 6.00 8.00 9.81
Stage 10
ARAMIS
gom
www.gom.com
Stage 11
Epsilon X
[%]
-0.0241
-0.0400
-0.0500
-0.0600
-0.0700
-0.0800
-0.0900
-0.1000
-0.1100
-0.1185
Epsilon X [%]
Horizontal
Vertical
Section length [in]
0.000 2.000 4.000 6.000 8.024
0.00 2.00 4.00 6.00 8.00 9.81
Stage 11
ARAMIS
gom
www.gom.com

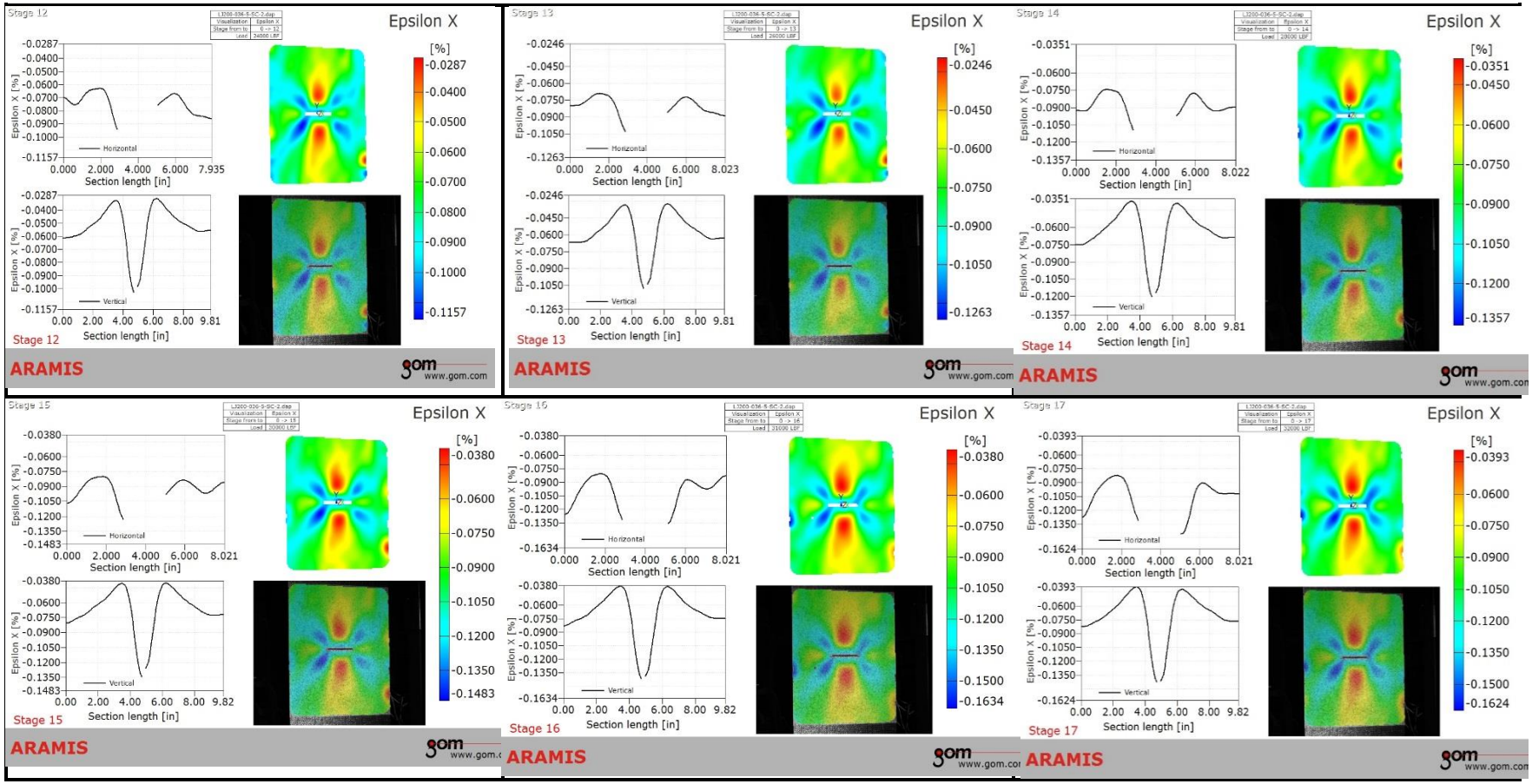
Stage 12
Epsilon X
[%]
-0.0287
-0.0400
-0.0500
-0.0600
-0.0700
-0.0800
-0.0900
-0.1000
-0.1157
Epsilon X [%]
Horizontal
Vertical
0.000 2.000 4.000 6.000 7.935
0.00 2.00 4.00 6.00 8.00 9.81
Section length [in]
Stage 12
ARAMIS
Stage 13
Epsilon X
[%]
-0.0246
-0.0450
-0.0600
-0.0750
-0.0900
-0.1050
-0.1263
0.000 2.000 4.000 6.000 8.023
0.00 2.00 4.00 6.00 8.00 9.81
Section length [in]
Stage 13
ARAMIS
Stage 14
Epsilon X
[%]
-0.0351
-0.0450
-0.0600
-0.0750
-0.0900
-0.1050
-0.1200
-0.1357
0.000 2.000 4.000 6.000 8.022
0.00 2.00 4.00 6.00 8.00 9.81
Section length [in]
Stage 14
ARAMIS
Stage 15
Epsilon X
[%]
-0.0380
-0.0600
-0.0750
-0.0900
-0.1050
-0.1200
-0.1350
-0.1483
0.000 2.000 4.000 6.000 8.021
0.00 2.00 4.00 6.00 8.00 9.82
Section length [in]
Stage 15
ARAMIS
Stage 16
Epsilon X
[%]
-0.0380
-0.0600
-0.0750
-0.0900
-0.1050
-0.1200
-0.1350
-0.1500
-0.1634
0.000 2.000 4.000 6.000 8.021
0.00 2.00 4.00 6.00 8.00 9.82
Section length [in]
Stage 16
ARAMIS
Stage 17
Epsilon X
[%]
-0.0393
-0.0600
-0.0750
-0.0900
-0.1050
-0.1200
-0.1350
-0.1500
-0.1624
0.000 2.000 4.000 6.000 8.021
0.00 2.00 4.00 6.00 8.00 9.82
Section length [in]
Stage 17
ARAMIS

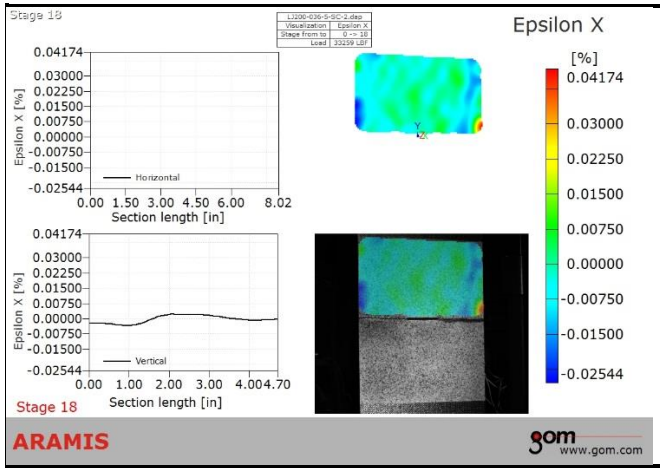
Stage 18
Epsilon X
[%]
0.04174
0.03000
0.02250
0.01500
0.00750
0.00000
-0.00750
-0.01500
-0.02544
Epsilon X [%]
Horizontal
Section length [in]
0.00 1.50 3.00 4.50 6.00 8.02
Vertical
0.00 1.00 2.00 3.00 4.00 4.70
Stage 18
ARAMIS
www.gom.com

Epsilon Y:

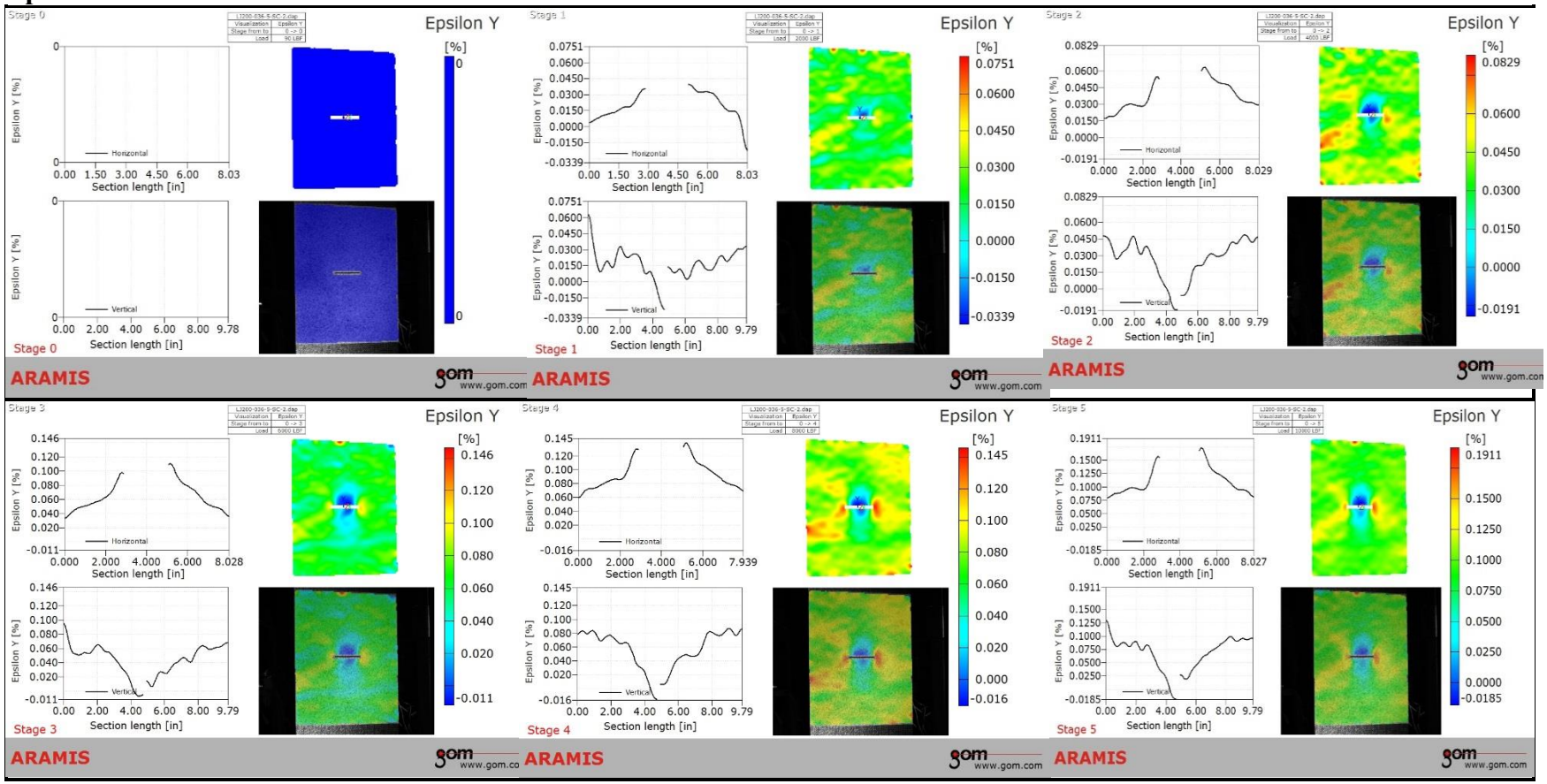
Stage 0
Epsilon Y
[%]
0
Epsilon Y [%]
Horizontal
Section length [in]
Vertical
Stage 0
ARAMIS
Stage 1
0.0751
0.0600
0.0450
0.0300
0.0150
0.0000
-0.0150
-0.0339
Stage 1
ARAMIS
Stage 2
0.0829
0.0600
0.0450
0.0300
0.0150
0.0000
-0.0191
Stage 2
ARAMIS
Stage 3
0.146
0.120
0.100
0.080
0.060
0.040
0.020
-0.011
Stage 3
ARAMIS
Stage 4
0.145
0.120
0.100
0.080
0.060
0.040
0.020
0.000
-0.016
Stage 4
ARAMIS
Stage 5
0.1911
0.1500
0.1250
0.1000
0.0750
0.0500
0.0250
0.0000
-0.0185
Stage 5
ARAMIS

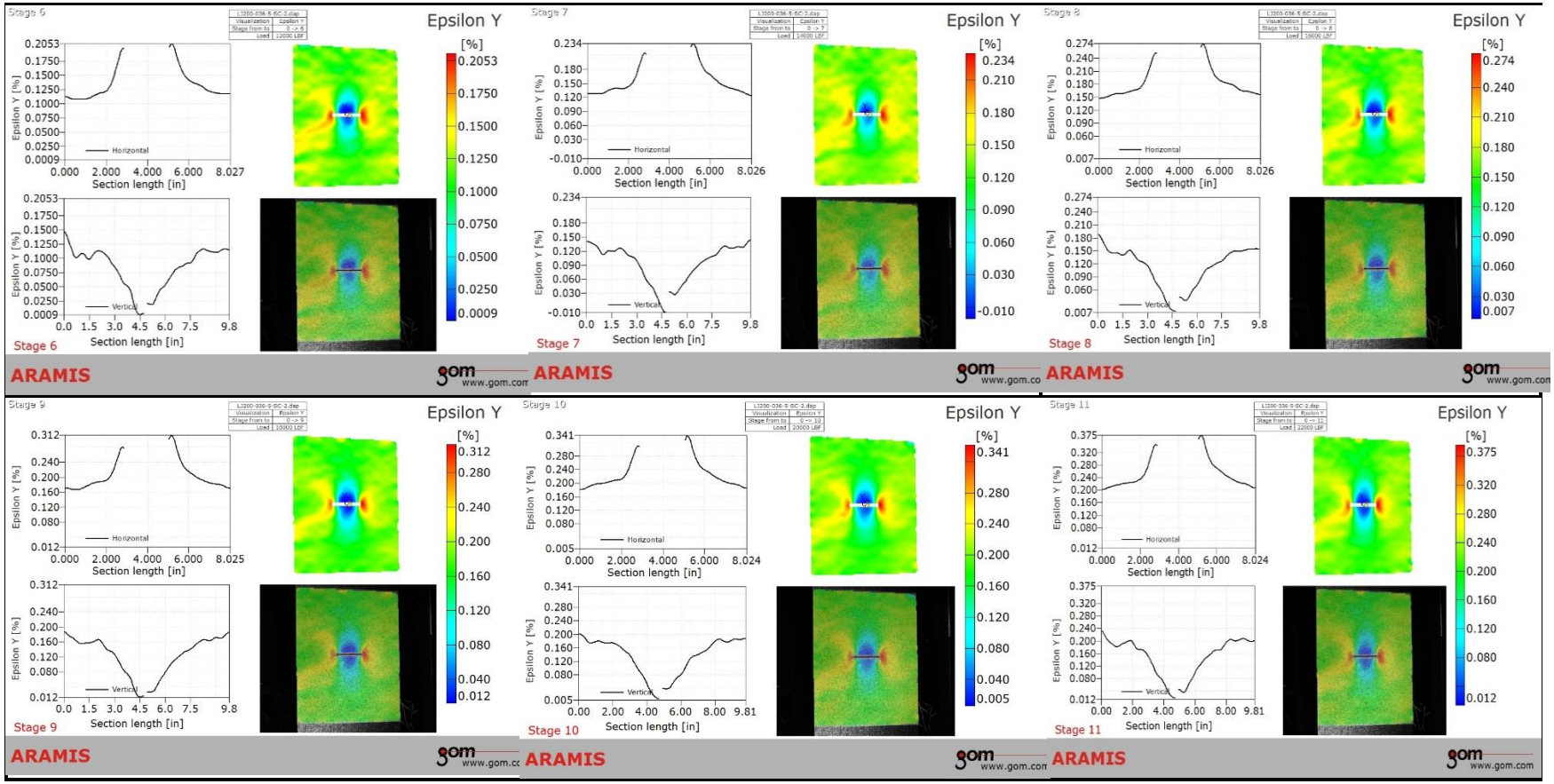
Stage 6
Epsilon Y
[%]
0.2053
0.1750
0.1500
0.1250
0.1000
0.0750
0.0500
0.0250
0.0009
Epsilon Y [%]
Horizontal
Section length [in]
0.000 2.000 4.000 6.000 8.027
Vertical
0.0 1.5 3.0 4.5 6.0 7.5 9.8
Stage 6
ARAMIS
Stage 7
Epsilon Y
[%]
0.234
0.210
0.180
0.150
0.120
0.090
0.060
0.030
-0.010
Horizontal
0.000 2.000 4.000 6.000 8.026
Vertical
0.0 1.5 3.0 4.5 6.0 7.5 9.8
Stage 7
ARAMIS
Stage 8
Epsilon Y
[%]
0.274
0.240
0.210
0.180
0.150
0.120
0.090
0.060
0.030
0.007
Horizontal
0.000 2.000 4.000 6.000 8.026
Vertical
0.0 1.5 3.0 4.5 6.0 7.5 9.8
Stage 8
ARAMIS
Stage 9
Epsilon Y
[%]
0.312
0.280
0.240
0.200
0.160
0.120
0.080
0.040
0.012
Horizontal
0.000 2.000 4.000 6.000 8.025
Vertical
0.0 1.5 3.0 4.5 6.0 7.5 9.8
Stage 9
ARAMIS
Stage 10
Epsilon Y
[%]
0.341
0.280
0.240
0.200
0.160
0.120
0.080
0.040
0.005
Horizontal
0.000 2.000 4.000 6.000 8.024
Vertical
0.00 2.00 4.00 6.00 8.00 9.81
Stage 10
ARAMIS
Stage 11
Epsilon Y
[%]
0.375
0.320
0.280
0.240
0.200
0.160
0.120
0.080
0.012
Horizontal
0.000 2.000 4.000 6.000 8.024
Vertical
0.00 2.00 4.00 6.00 8.00 9.81
Stage 11
ARAMIS

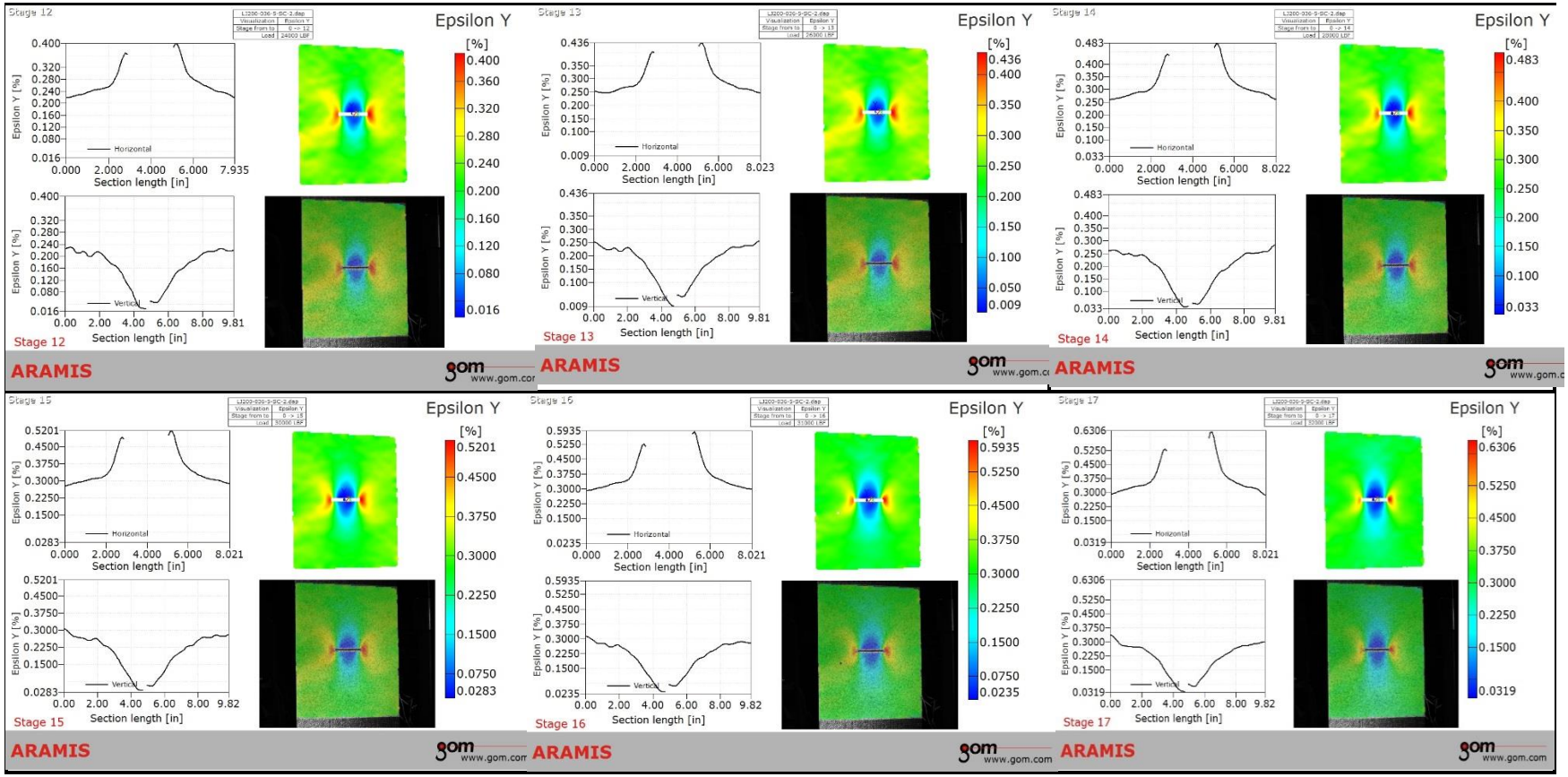
Stage 12
Epsilon Y
[%]
0.400
0.360
0.320
0.280
0.240
0.200
0.160
0.120
0.080
0.016
Epsilon Y [%]
Horizontal
Section length [in]
0.000 2.000 4.000 6.000 7.935
Vertical
0.00 2.00 4.00 6.00 8.00 9.81
Stage 12
ARAMIS
gom
www.gom.com
Stage 13
Epsilon Y
[%]
0.436
0.400
0.350
0.300
0.250
0.200
0.150
0.100
0.050
0.009
Horizontal
0.000 2.000 4.000 6.000 8.023
Vertical
0.00 2.00 4.00 6.00 8.00 9.81
Stage 13
ARAMIS
Stage 14
Epsilon Y
[%]
0.483
0.400
0.350
0.300
0.250
0.200
0.150
0.100
0.033
Horizontal
0.000 2.000 4.000 6.000 8.022
Vertical
0.00 2.00 4.00 6.00 8.00 9.81
Stage 14
ARAMIS
Stage 15
Epsilon Y
[%]
0.5201
0.4500
0.3750
0.3000
0.2250
0.1500
0.0750
0.0283
Horizontal
0.000 2.000 4.000 6.000 8.021
Vertical
0.00 2.00 4.00 6.00 8.00 9.82
Stage 15
ARAMIS
Stage 16
Epsilon Y
[%]
0.5935
0.5250
0.4500
0.3750
0.3000
0.2250
0.1500
0.0750
0.0235
Horizontal
0.000 2.000 4.000 6.000 8.021
Vertical
0.00 2.00 4.00 6.00 8.00 9.82
Stage 16
ARAMIS
Stage 17
Epsilon Y
[%]
0.6306
0.5250
0.4500
0.3750
0.3000
0.2250
0.1500
0.0319
Horizontal
0.000 2.000 4.000 6.000 8.021
Vertical
0.00 2.00 4.00 6.00 8.00 9.82
Stage 17
ARAMIS

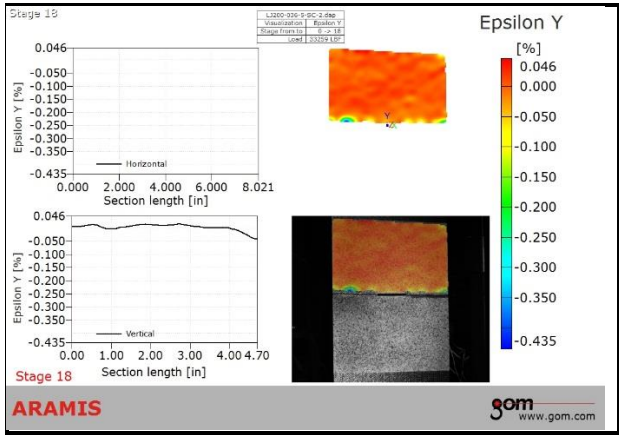
Stage 18
Epsilon Y
[%]
0.046
0.000
-0.050
-0.100
-0.150
-0.200
-0.250
-0.300
-0.350
-0.435
Epsilon Y [%]
Horizontal
Section length [in]
0.000 2.000 4.000 6.000 8.021
Vertical
0.00 1.00 2.00 3.00 4.00 4.70
Stage 18
ARAMIS
www.gom.com

LJ200-036-6-SC-1

Epsilon X:

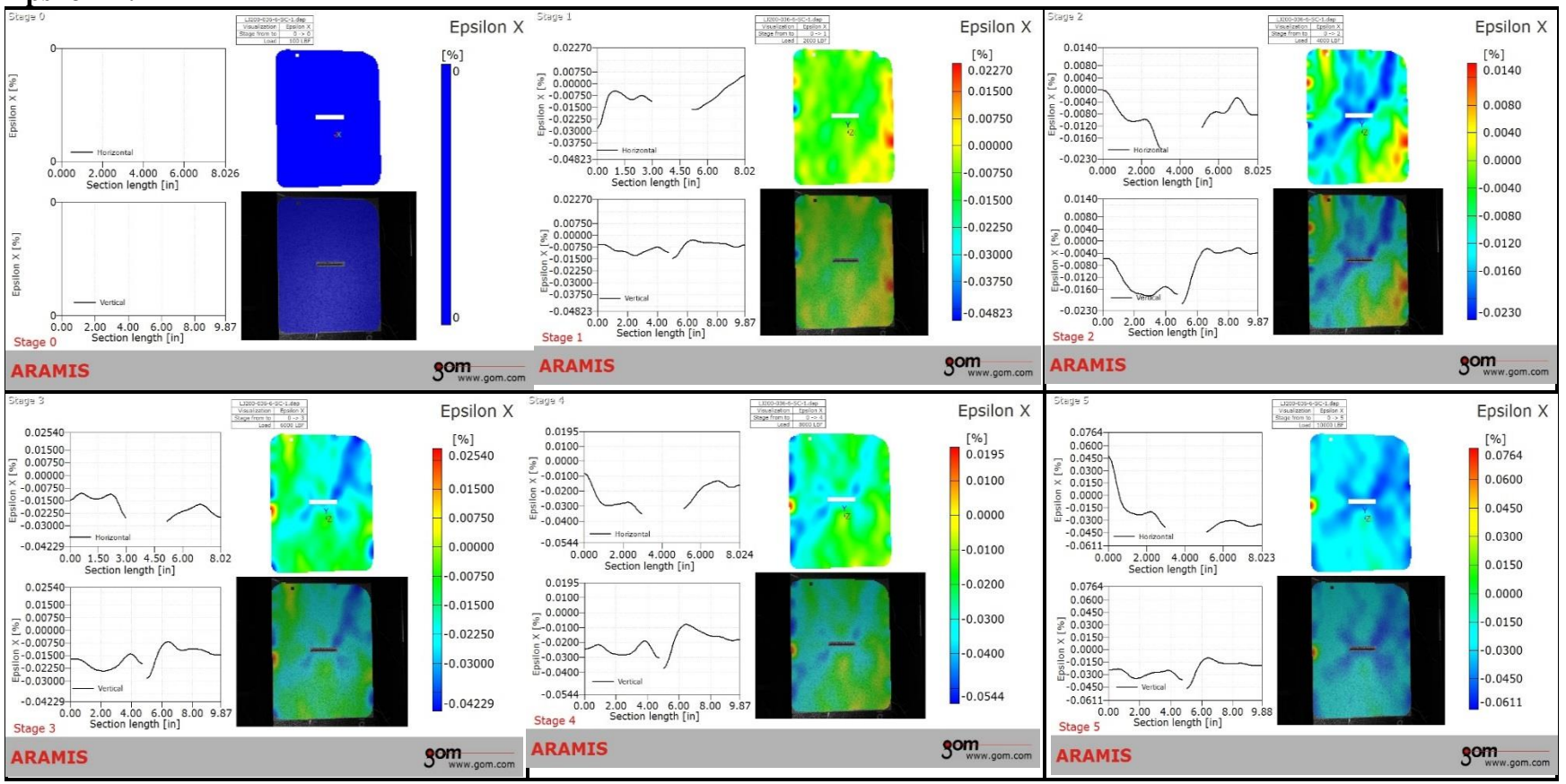

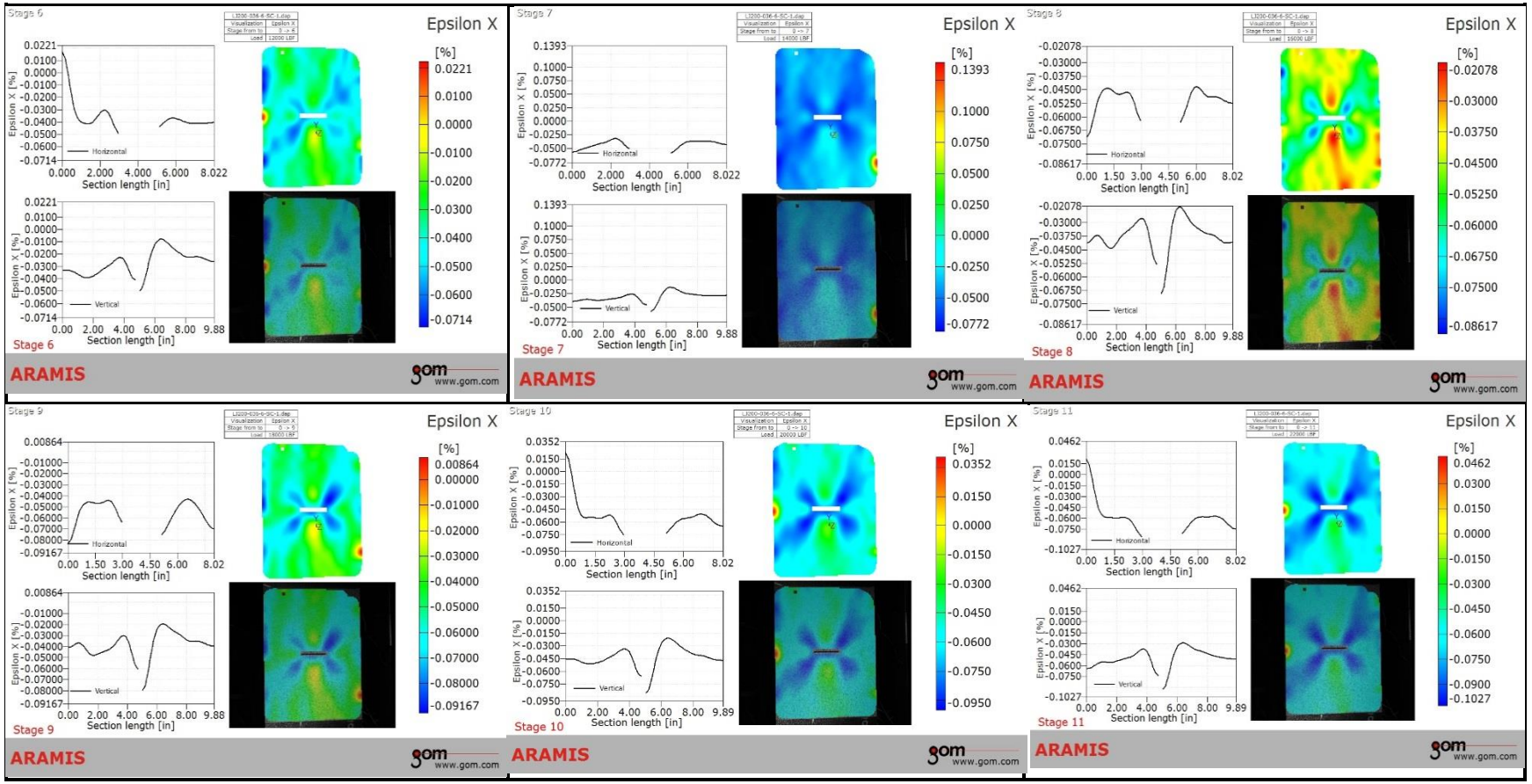
Stage 6
Epsilon X
[%]
0.0221
0.0100
0.0000
-0.0100
-0.0200
-0.0300
-0.0400
-0.0500
-0.0600
-0.0714
Epsilon X [%]
Horizontal
Vertical
Section length [in]
0.000 2.000 4.000 6.000 8.022
0.00 2.00 4.00 6.00 8.00 9.88
Stage 6
ARAMIS
gom
www.gom.com
Stage 7
Epsilon X
[%]
0.1393
0.1000
0.0750
0.0500
0.0250
0.0000
-0.0250
-0.0500
-0.0772
Epsilon X [%]
Horizontal
Vertical
Section length [in]
0.000 2.000 4.000 6.000 8.022
0.00 2.00 4.00 6.00 8.00 9.88
Stage 7
ARAMIS
gom
www.gom.com
Stage 8
Epsilon X
[%]
-0.02078
-0.03000
-0.03750
-0.04500
-0.05250
-0.06000
-0.06750
-0.07500
-0.08617
Epsilon X [%]
Horizontal
Vertical
Section length [in]
0.00 1.50 3.00 4.50 6.00 8.02
0.00 2.00 4.00 6.00 8.00 9.88
Stage 8
ARAMIS
gom
www.gom.com
Stage 9
Epsilon X
[%]
0.00864
0.00000
-0.01000
-0.02000
-0.03000
-0.04000
-0.05000
-0.06000
-0.07000
-0.08000
-0.09167
Epsilon X [%]
Horizontal
Vertical
Section length [in]
0.00 1.50 3.00 4.50 6.00 8.02
0.00 2.00 4.00 6.00 8.00 9.88
Stage 9
ARAMIS
gom
www.gom.com
Stage 10
Epsilon X
[%]
0.0352
0.0150
0.0000
-0.0150
-0.0300
-0.0450
-0.0600
-0.0750
-0.0950
Epsilon X [%]
Horizontal
Vertical
Section length [in]
0.00 1.50 3.00 4.50 6.00 8.02
0.00 2.00 4.00 6.00 8.00 9.89
Stage 10
ARAMIS
gom
www.gom.com
Stage 11
Epsilon X
[%]
0.0462
0.0300
0.0150
0.0000
-0.0150
-0.0300
-0.0450
-0.0600
-0.0750
-0.0900
-0.1027
Epsilon X [%]
Horizontal
Vertical
Section length [in]
0.00 1.50 3.00 4.50 6.00 8.02
0.00 2.00 4.00 6.00 8.00 9.89
Stage 11
ARAMIS
gom
www.gom.com

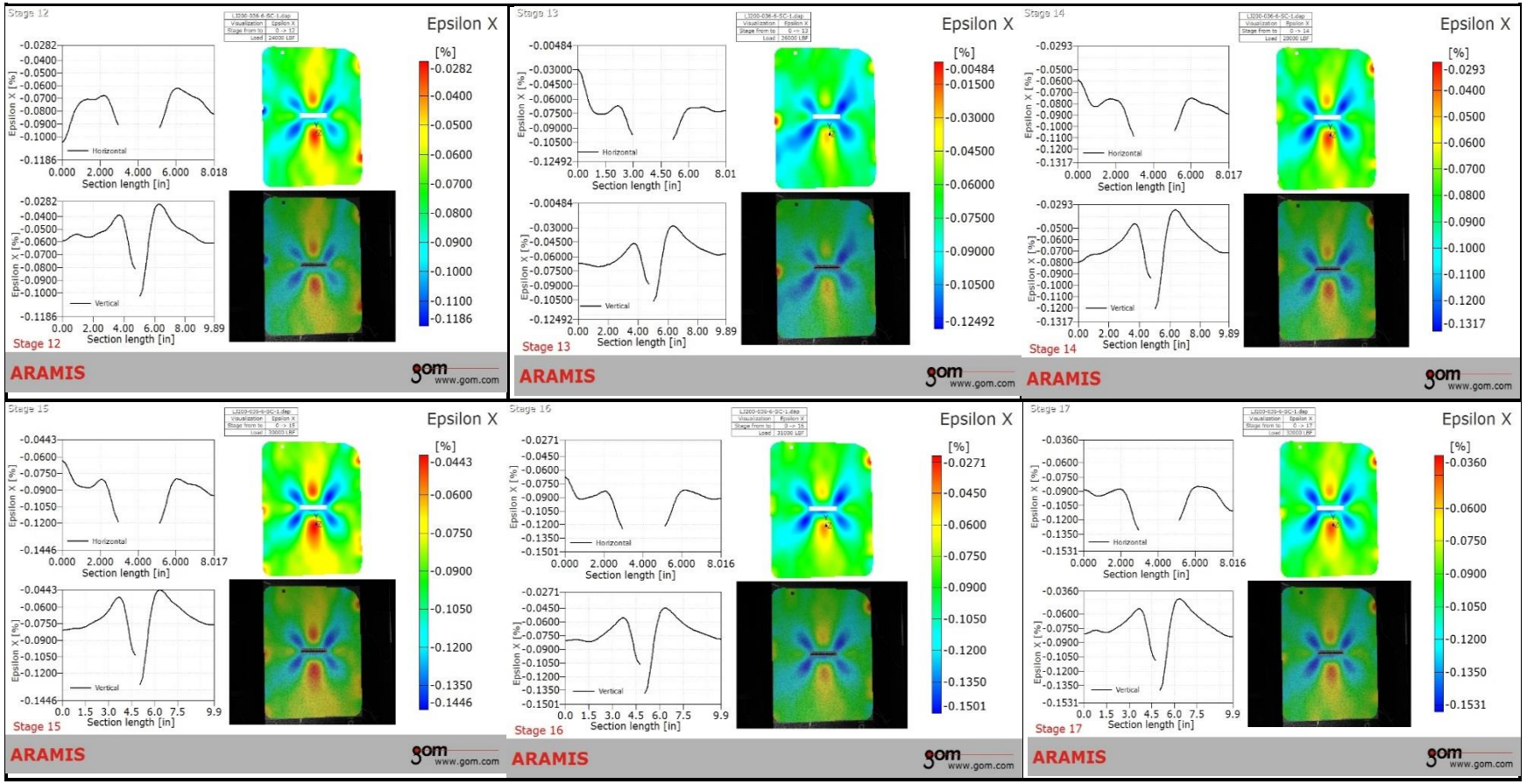
Stage 12
Epsilon X
[%]
-0.0282
-0.0400
-0.0500
-0.0600
-0.0700
-0.0800
-0.0900
-0.1000
-0.1100
-0.1186
Epsilon X [%]
Horizontal
Vertical
Section length [in]
0.000 2.000 4.000 6.000 8.018
0.00 2.00 4.00 6.00 8.00 9.89
Stage 12
ARAMIS
gom
www.gom.com
Stage 13
-0.00484
-0.01500
-0.03000
-0.04500
-0.06000
-0.07500
-0.09000
-0.10500
-0.12492
0.00 1.50 3.00 4.50 6.00 8.01
Stage 13
Stage 14
-0.0293
-0.0400
-0.0500
-0.0600
-0.0700
-0.0800
-0.0900
-0.1000
-0.1100
-0.1200
-0.1317
0.000 2.000 4.000 6.000 8.017
Stage 14
Stage 15
-0.0443
-0.0600
-0.0750
-0.0900
-0.1050
-0.1200
-0.1350
-0.1446
0.000 2.000 4.000 6.000 8.017
0.0 1.5 3.0 4.5 6.0 7.5 9.9
Stage 15
Stage 16
-0.0271
-0.0450
-0.0600
-0.0750
-0.0900
-0.1050
-0.1200
-0.1350
-0.1501
0.000 2.000 4.000 6.000 8.016
Stage 16
Stage 17
-0.0360
-0.0600
-0.0750
-0.0900
-0.1050
-0.1200
-0.1350
-0.1531
0.000 2.000 4.000 6.000 8.016
Stage 17

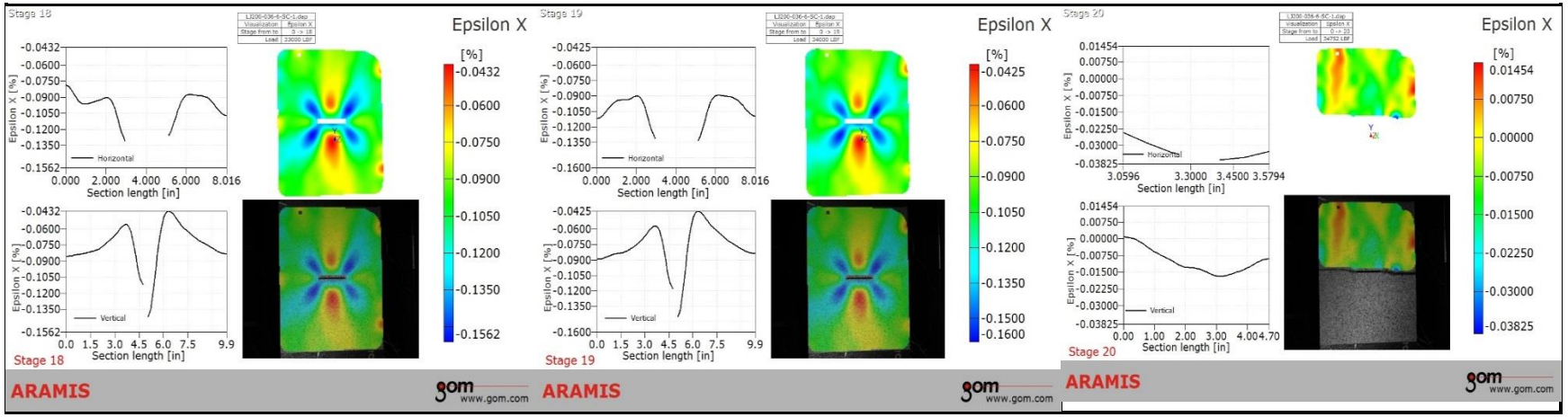
Stage 18
Epsilon X
[%]
-0.0432
-0.0600
-0.0750
-0.0900
-0.1050
-0.1200
-0.1350
-0.1562
Epsilon X [%]
Horizontal
Section length [in]
0.000 2.000 4.000 6.000 8.016
Vertical
0.0 1.5 3.0 4.5 6.0 7.5 9.9
Stage 18
ARAMIS
gom www.gom.com
Stage 19
Epsilon X
[%]
-0.0425
-0.0600
-0.0750
-0.0900
-0.1050
-0.1200
-0.1350
-0.1500
-0.1600
Horizontal
Section length [in]
0.000 2.000 4.000 6.000 8.016
Vertical
0.0 1.5 3.0 4.5 6.0 7.5 9.9
Stage 19
ARAMIS
gom www.gom.com
Stage 20
Epsilon X
[%]
0.01454
0.00750
0.00000
-0.00750
-0.01500
-0.02250
-0.03000
-0.03825
Epsilon X [%]
Horizontal
Section length [in]
3.0596 3.3000 3.4500 3.5794
Vertical
0.00 1.00 2.00 3.00 4.004.70
Stage 20
ARAMIS
gom www.gom.com

Epsilon Y:

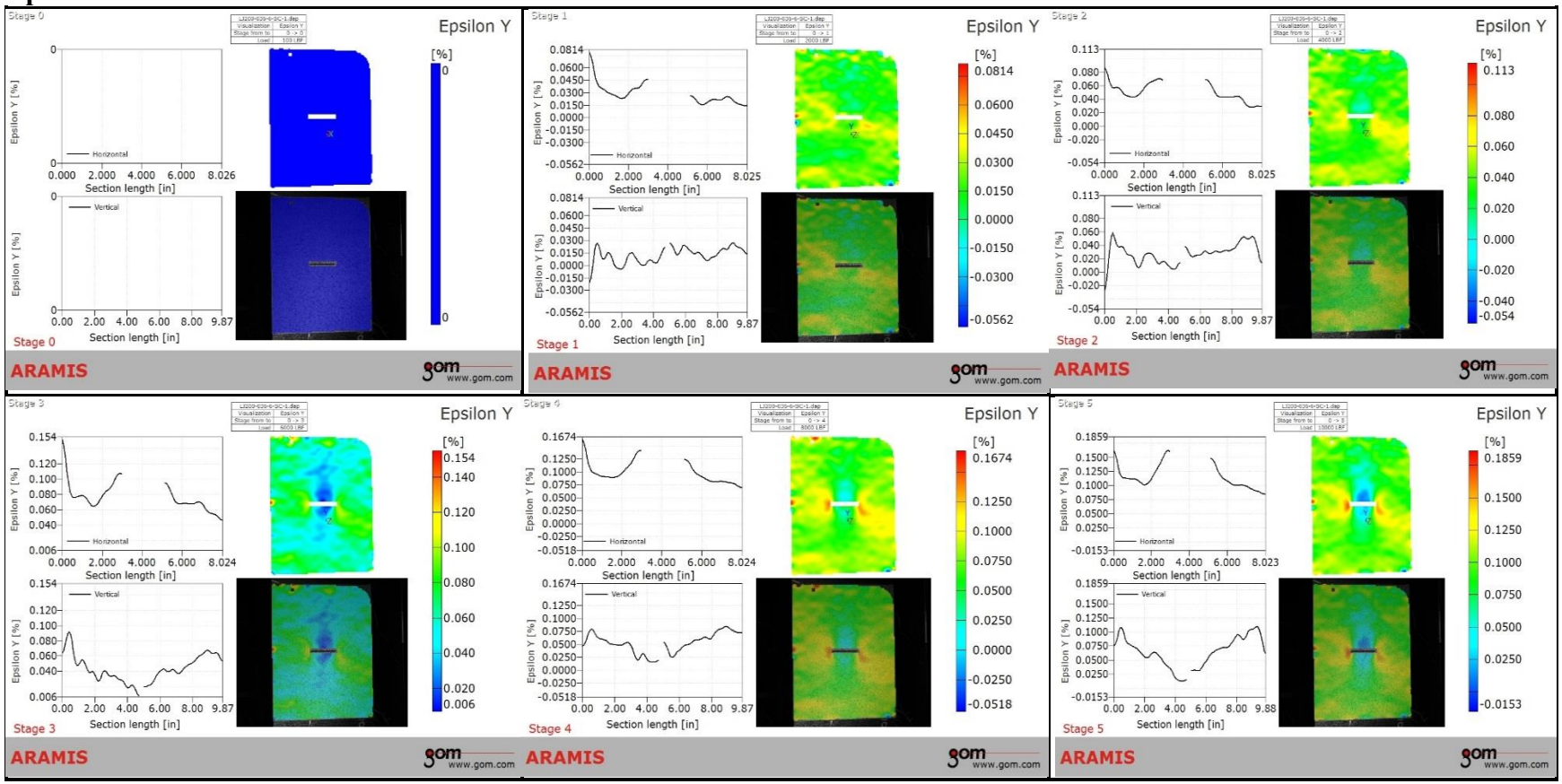
Stage 0
Epsilon Y
[%]
0
0
Horizontal
Vertical
Epsilon Y [%]
Section length [in]
0.000 2.000 4.000 6.000 8.026
0.00 2.00 4.00 6.00 8.00 9.87
Stage 0
ARAMIS
gom
www.gom.com
Stage 1
Epsilon Y
[%]
0.0814
0.0600
0.0450
0.0300
0.0150
0.0000
-0.0150
-0.0300
-0.0562
0.000 2.000 4.000 6.000 8.025
0.00 2.00 4.00 6.00 8.00 9.87
Stage 1
ARAMIS
Stage 2
Epsilon Y
[%]
0.113
0.080
0.060
0.040
0.020
0.000
-0.020
-0.040
-0.054
0.000 2.000 4.000 6.000 8.025
0.00 2.00 4.00 6.00 8.00 9.87
Stage 2
ARAMIS
Stage 3
Epsilon Y
[%]
0.154
0.140
0.120
0.100
0.080
0.060
0.040
0.020
0.006
0.000 2.000 4.000 6.000 8.024
0.00 2.00 4.00 6.00 8.00 9.87
Stage 3
ARAMIS
Stage 4
Epsilon Y
[%]
0.1674
0.1250
0.1000
0.0750
0.0500
0.0250
0.0000
-0.0250
-0.0518
0.000 2.000 4.000 6.000 8.024
0.00 2.00 4.00 6.00 8.00 9.87
Stage 4
ARAMIS
Stage 5
Epsilon Y
[%]
0.1859
0.1500
0.1250
0.1000
0.0750
0.0500
0.0250
-0.0153
0.000 2.000 4.000 6.000 8.023
0.00 2.00 4.00 6.00 8.00 9.88
Stage 5
ARAMIS

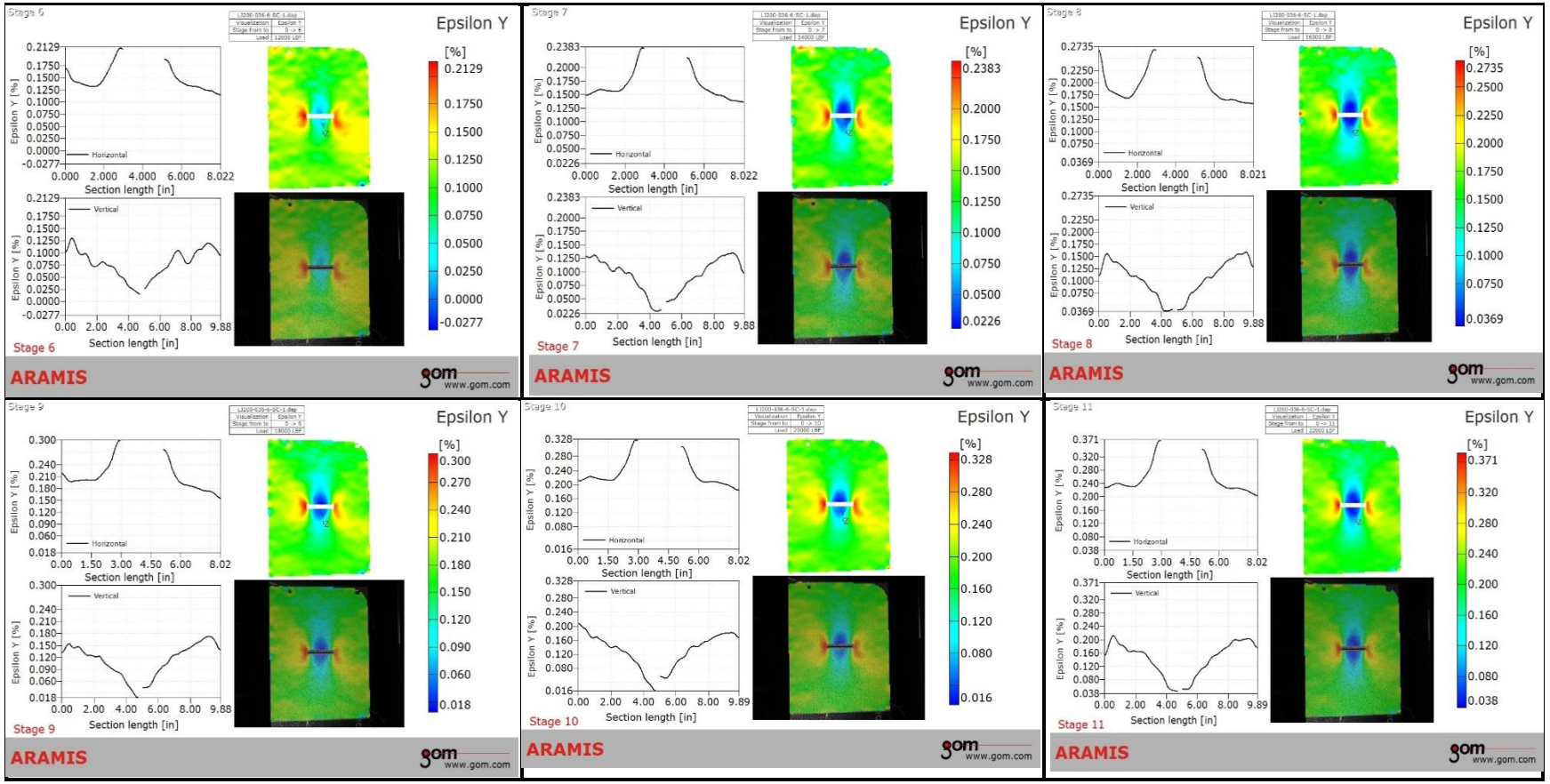
Stage 6
Epsilon Y
[%]
0.2129
0.1750
0.1500
0.1250
0.1000
0.0750
0.0500
0.0250
0.0000
-0.0277
Epsilon Y [%]
Horizontal
Vertical
Section length [in]
0.000 2.000 4.000 6.000 8.022
0.00 2.00 4.00 6.00 8.00 9.88
Stage 6
ARAMIS
gom
www.gom.com
Stage 7
Epsilon Y
[%]
0.2383
0.2000
0.1750
0.1500
0.1250
0.1000
0.0750
0.0500
0.0226
Epsilon Y [%]
Horizontal
Vertical
Section length [in]
0.000 2.000 4.000 6.000 8.022
0.00 2.00 4.00 6.00 8.00 9.88
Stage 7
ARAMIS
gom
www.gom.com
Stage 8
Epsilon Y
[%]
0.2735
0.2500
0.2250
0.2000
0.1750
0.1500
0.1250
0.1000
0.0750
0.0369
Epsilon Y [%]
Horizontal
Vertical
Section length [in]
0.000 2.000 4.000 6.000 8.021
0.00 2.00 4.00 6.00 8.00 9.88
Stage 8
ARAMIS
gom
www.gom.com
Stage 9
Epsilon Y
[%]
0.300
0.270
0.240
0.210
0.180
0.150
0.120
0.090
0.060
0.018
Epsilon Y [%]
Horizontal
Vertical
Section length [in]
0.00 1.50 3.00 4.50 6.00 8.02
0.00 2.00 4.00 6.00 8.00 9.88
Stage 9
ARAMIS
gom
www.gom.com
Stage 10
Epsilon Y
[%]
0.328
0.280
0.240
0.200
0.160
0.120
0.080
0.016
Epsilon Y [%]
Horizontal
Vertical
Section length [in]
0.00 1.50 3.00 4.50 6.00 8.02
0.00 2.00 4.00 6.00 8.00 9.89
Stage 10
ARAMIS
gom
www.gom.com
Stage 11
Epsilon Y
[%]
0.371
0.320
0.280
0.240
0.200
0.160
0.120
0.080
0.038
Epsilon Y [%]
Horizontal
Vertical
Section length [in]
0.00 1.50 3.00 4.50 6.00 8.02
0.00 2.00 4.00 6.00 8.00 9.89
Stage 11
ARAMIS
gom
www.gom.com

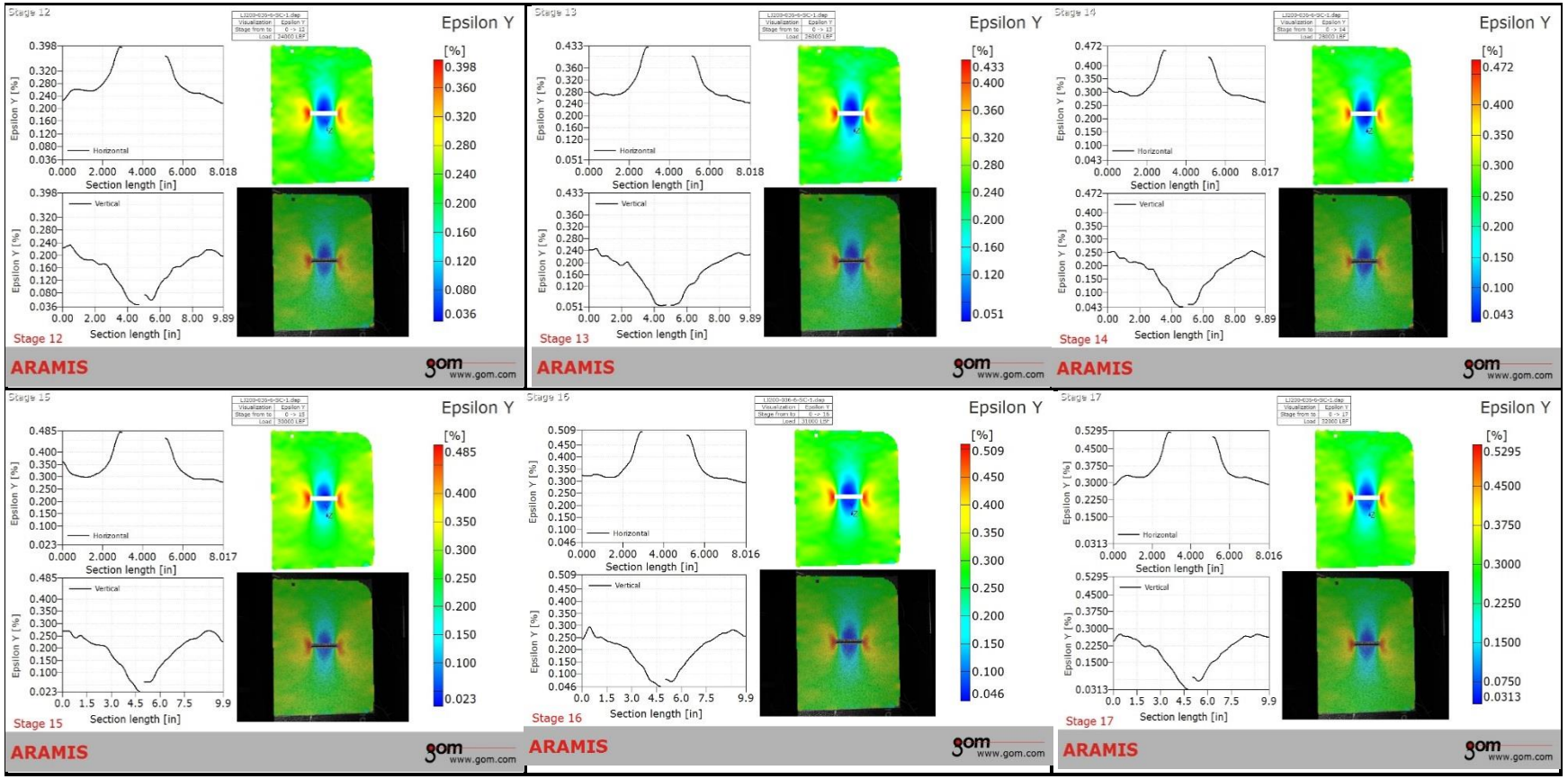
Stage 12
Epsilon Y
[%]
0.398
0.360
0.320
0.280
0.240
0.200
0.160
0.120
0.080
0.036
Epsilon Y [%]
Horizontal
Vertical
Section length [in]
0.000 2.000 4.000 6.000 8.018
0.00 2.00 4.00 6.00 8.00 9.89
Stage 12
ARAMIS
gom
www.gom.com
Stage 13
Epsilon Y
[%]
0.433
0.400
0.360
0.320
0.280
0.240
0.200
0.160
0.120
0.051
Horizontal
Vertical
Section length [in]
0.000 2.000 4.000 6.000 8.018
0.00 2.00 4.00 6.00 8.00 9.89
Stage 13
ARAMIS
gom
www.gom.com
Stage 14
Epsilon Y
[%]
0.472
0.400
0.350
0.300
0.250
0.200
0.150
0.100
0.043
Horizontal
Vertical
Section length [in]
0.000 2.000 4.000 6.000 8.017
0.00 2.00 4.00 6.00 8.00 9.89
Stage 14
ARAMIS
gom
www.gom.com
Stage 15
Epsilon Y
[%]
0.485
0.400
0.350
0.300
0.250
0.200
0.150
0.100
0.023
Horizontal
Vertical
Section length [in]
0.000 2.000 4.000 6.000 8.017
0.0 1.5 3.0 4.5 6.0 7.5 9.9
Stage 15
ARAMIS
gom
www.gom.com
Stage 16
Epsilon Y
[%]
0.509
0.450
0.400
0.350
0.300
0.250
0.200
0.150
0.100
0.046
Horizontal
Vertical
Section length [in]
0.000 2.000 4.000 6.000 8.016
0.0 1.5 3.0 4.5 6.0 7.5 9.9
Stage 16
ARAMIS
gom
www.gom.com
Stage 17
Epsilon Y
[%]
0.5295
0.4500
0.3750
0.3000
0.2250
0.1500
0.0750
0.0313
Horizontal
Vertical
Section length [in]
0.000 2.000 4.000 6.000 8.016
0.0 1.5 3.0 4.5 6.0 7.5 9.9
Stage 17
ARAMIS
gom
www.gom.com

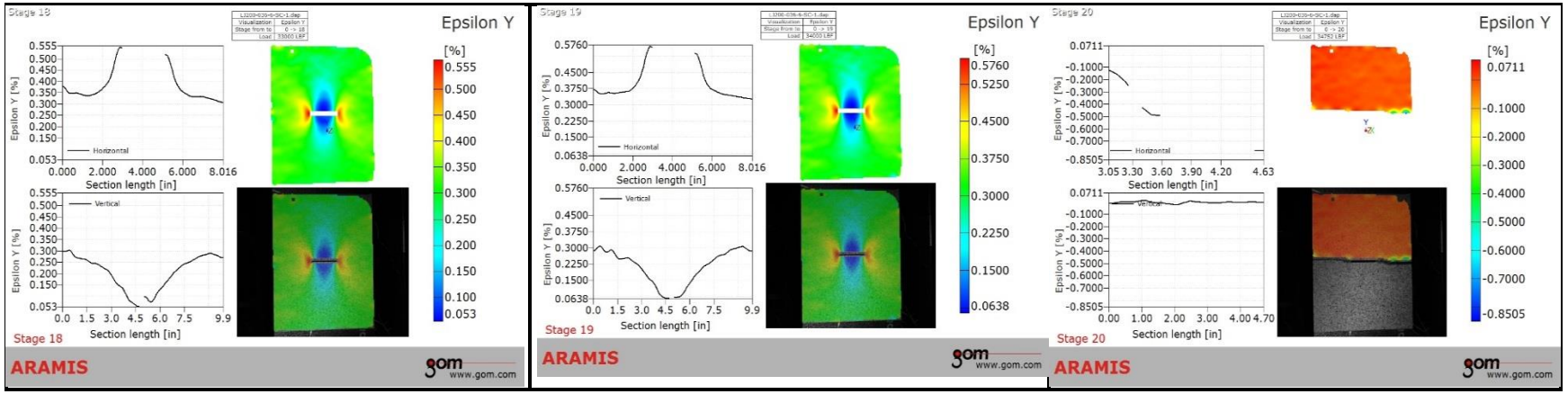
Stage 18
Epsilon Y
[%]
0.555
0.500
0.450
0.400
0.350
0.300
0.250
0.200
0.150
0.100
0.053
Epsilon Y [%]
Horizontal
Section length [in]
Vertical
Stage 18
ARAMIS
gom
www.gom.com
Stage 19
Epsilon Y
[%]
0.5760
0.5250
0.4500
0.3750
0.3000
0.2250
0.1500
0.0638
Horizontal
Section length [in]
Vertical
Stage 19
ARAMIS
gom
www.gom.com
Stage 20
Epsilon Y
[%]
0.0711
-0.1000
-0.2000
-0.3000
-0.4000
-0.5000
-0.6000
-0.7000
-0.8505
Horizontal
Section length [in]
Vertical
Stage 20
ARAMIS
gom
www.gom.com

APPENDIX C

OVERALL DETAILED TEST MATRIX

Test Type	Test ID	Flaw Type	Flaw Length, 2c (in)	Laminate	Lay-up	No. of Plies	Average Thickness (in)	Gage Section Height (in)	Gage Section Width (in)	Test Condition (1)	No. of Specimens
Tension Fracture Strength Test	1	Circular Hole	2.0	SL-12	$[45/0_2/45/0/45]_s$	12	0.094	20	8	RTA	3
	2	Saw Cut	2.0	SL-12	$[45/0_2/45/0/45]_s$	12	0.094	20	8	RTA	3
	3	Saw Cut	2.0	SL-12	$[45/0_2/45/0/45]_s$	12	0.094	20	8	CTD	3
	4(2)	Saw Cut	2.0	SL-12	$[45/0_2/45/0/45]_s$	12	0.094	20	8	ETW	3
	5	Saw Cut	2.0	SL-24	$[45/0_2/45_2/0_2/45_2/0_2/45]_s$	24	0.186	20	8	RTA	3
	6	Saw Cut	2.0	SL-24 Co-cured Splice	$[45/0_2/45_2/0_2/45_2/0_2/45]_s$	24	0.186	20	8	RTA	3
	7	Saw Cut	5.0	SL-12	$[45/0_2/45/0/45]_s$	12	0.094	50	20	RTA	3
	8	Saw Cut	5.0	SL-24	$[45/0_2/45_2/0_2/45_2/0_2/45]_s$	24	0.186	50	20	RTA	3
Compression Fracture Strength Test	9(2)	Circular Hole	2.0	SL-12	$[45/0_2/45/0/45]_s$	12	0.094	20	8	RTA	3
	10(2)	Saw Cut	2.0	SL-12	$[45/0_2/45/0/45]_s$	12	0.094	20	8	RTA	3
	11(2)	Saw Cut	2.0	SL-12	$[45/0_2/45/0/45]_s$	12	0.094	20	8	CTD	3
	12(2)	Saw Cut	2.0	SL-12	$[45/0_2/45/0/45]_s$	12	0.094	20	8	ETW	3
	13(2)	Saw Cut	2.0	SL-24	$[45/0_2/45_2/0_2/45_2/0_2/45]_s$	24	0.186	20	8	RTA	3
	14(2)	Saw Cut	2.0	SL-24 Co-cured Splice	$[45/0_2/45_2/0_2/45_2/0_2/45]_s$	24	0.186	20	8	RTA	3
	15(2)	Saw Cut	5.0	SL-12	$[45/0_2/45/0/45]_s$	12	0.094	36*(3)	20	RTA	3
	16(2)	Saw Cut	5.0	SL-24	$[45/0_2/45_2/0_2/45_2/0_2/45]_s$	24	0.186	36*(3)	20	RTA	3
										Sub-Total	48

Notes:

1) Test conditions: RTA = Room Temperature Ambient, test temperature at 70°F ± 10°F and specimen in as-is moisture content state.
CTD = Cold Temperature Dry, test temperature at -94°F ± 5°F, dry moisture content.
ETW = Elevated Temperature Wet, test temperature at 180°F ± 5°F at which specimens shall be pre-conditioned wet to saturation prior to the start of testing.

2) The highlighted portion of test matrix is in work. ETW test condition requires test articles to be pre-conditioned in long hot wet conditioning period. Furthermore, several challenges are experienced from test fixturing for compression testing.
3) Gage height is reduced because of test fixture height limitation.